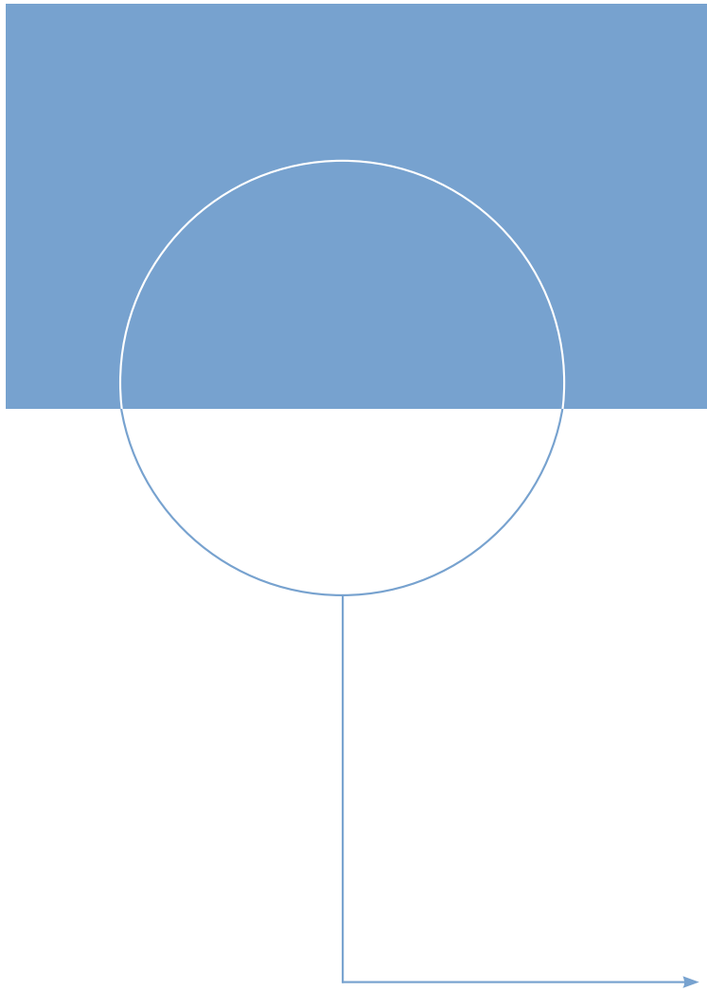

Master's thesis

2019

Eivind Jülke Røer

NTNU
Norwegian University of
Science and Technology
Faculty of Information Technology and Electrical
Engineering
Department of Electronic Systems

Eivind Jülke Røer

Optimization and Fabrication of Photonic Crystal Drop Filters for Optical Biosensing

June 2019

NTNU
Norwegian University of
Science and Technology

NTNU
Norwegian University of
Science and Technology

NTNU

Norwegian University of
Science and Technology

Optimization and Fabrication of Photonic Crystal Drop Filters for Optical Biosensing

Eivind Jülke Røer

Nanotechnology
Submission date: June 2019
Supervisor: Astrid Aksnes
Co-supervisor: Mukesh Yadav

Norwegian University of Science and Technology
Department of Electronic Systems

Problem Description

Photonic crystals are materials with a periodic dielectric function. Such materials can have a photonic band gap which allows for light confinement in compact photonic devices.

In this master's project, a refractive index sensor based on a photonic crystal filter will be investigated. The photonic sensor will be a drop filter made in a silicon-on-insulator (SOI) system since this material system is compatible with existing fabrication processes developed for the CMOS industry.

The sensor will be designed using COMSOL and the open source software packages MIT Photonic Bands and MIT Electromagnetic Equation Propagation. Time-consuming 3D simulations will be performed using Fram, the newest high performance computing resource in Norway. The goals of the simulations are to understand and improve key properties of the sensor, such as the quality factor and the signal-to-noise ratio of the filter.

Fabrication and characterization of the photonic sensor will be done at NTNU Nanolab. Plasma-enhanced chemical vapor deposition (PECVD), electron beam lithography (EBL), inductively coupled reactive-ion etching (ICP-RIE), and photolithography will be used to fabricate the device. Scanning electron microscopy (SEM) and optical measurements using a tunable laser will be used for characterizing the fabricated devices. The goal of the experimental part of the project is to fabricate devices with performance similar to simulated devices.

Abstract

Photonic crystals can be used to make compact photonic devices. The use of photonic crystal drop filters as label-free optical biosensors by refractive index sensing was investigated in this study.

The drop filter consists of two photonic crystal waveguides placed above and below a photonic crystal resonator. The components of the drop filter were designed and simulated in 2D and 3D using COMSOL and the open-source software packages MIT Photonic Bands and MIT Electromagnetic Equation Propagation. After optimization, a drop filter with a quality factor of 9,800 and 45% transmission at resonance was simulated in 3D. Additionally, the quality factor of the unloaded resonator was improved to 414,000, more than an order of magnitude higher than achieved in earlier work by the author. A multiplexer device consisting of four drop filters placed in series was simulated in 2D, and precise control of four resonance peaks was demonstrated.

Photonic crystal drop filters based on the simulations were fabricated using electron beam lithography (EBL) to pattern silicon-on-insulator samples made using plasma-enhanced chemical vapor deposition (PECVD). Patterned samples were later etched using inductively coupled plasma reactive-ion etching (ICP-RIE). High quality photonic crystal devices were fabricated, with transmission spectra for photonic crystal waveguides and filters similar to simulated spectra. A quality factor of 2,100 was found for the drop filter. Additionally, a resonance shift of 21.1 nm was found after depositing a drop of water on top of the sensor, similar to the 18.6 nm resonance shift found in 3D simulations.

Sammendrag

Fotoniske krystaller kan bli brukt til å lage kompakte fotoniske komponenter. Frekvensfiltre basert på fotoniske krystaller blir i denne studien undersøkt for bruk som brytningsindeksbaserte biosensorer.

Filteret undersøkt her består av to bølgeledere plassert over og under en resonanskavitet i en fotonisk krystall. De forskjellige komponentene til filteret ble designet og simulert i to og tre dimensjoner med COMSOL og de fritt tilgjengelige programvarepakkene MIT Photonic Bands og MIT Electromagnetic Equation Propagation. Et frekvensfilter med kvalitetsfaktor 9,800 og 45% transmisjon ved resonans ble simulert i 3D etter optimering av de forskjellige komponentene. Videre ble kvalitetsfaktoren til resonatoren brukt i filtrene forbedret til 414,000, mer enn en størrelsesorden sammenlignet med tidligere arbeid. En multiplexer bestående av fire separate filtre ble simulert i 2D, og nøyaktig kontroll av fire separate resonanstopper ble demonstrert.

Fotonisk krystall-filtre basert på simuleringene ble fabrikert ved bruk av elektronstålelitografi (EBL) til mønstring av silicon-on-insulator-prøver lagd med plasma-forbedret kjemisk dampfase-deponering (PECVD). Mønstrede prøver ble deretter etset med reaktiv ioneetsing med induktivt koblet plasma (ICP-RIE). Bølgeledere og filtre i fotoniske krystaller av høy kvalitet ble fabrikert, og transmisjonsspektrene funnet med tunebar laser stemte godt overens med simuleringer. En kvalitetsfaktor på 2,100 ble funnet for et av filtrene. Sensitiviteten til sensoren ble testet ved å legge en dråpe vann over filteret. Et resonansskift på 21.1 nm ble funnet, noe som er nære resonansskiftet på 18.6 nm funnet i simuleringer.

Preface

This thesis is written based on work done during Spring 2019 and concludes my five years of studies at the Norwegian University of Science and Technology (NTNU). The thesis is the final work for a degree of Master of Science in Nanotechnology at the Department of Electronic Systems (IES). This work is a continuation of a 15 ECTS specialization project carried out during Fall 2018, where a photonic crystal drop filter was designed and simulated. The theory chapter from the project report is partly reproduced here. Additionally, a few results are presented again to compare with new results. The experimental procedure used for fabricating devices is based on work done by previous master's students [1–3].

Acknowledgements

I would like to thank my supervisor Astrid Aksnes for guidance and valuable feedback during the project. I would also like to thank my co-supervisor Mukesh Yadav and Jens Høvik for giving me training on equipment used for fabrication and characterization, and for sharing their cleanroom experience. Finally, I thank my family and Amanda for their continuous support during these five years of study.

The simulations were performed on resources provided by UNINETT Sigma2 - the National Infrastructure for High Performance Computing and Data Storage in Norway.

The Research Council of Norway is acknowledged for the support to the Norwegian Micro- and Nano-Fabrication Facility, NorFab.

List of Abbreviations

a-Si Amorphous Silicon

BZ Brillouin Zone

c-Si Crystalline Silicon

CVD Chemical Vapor Deposition

EBL Electron-beam Lithography

ELISA Enzyme-linked Immunosorbent Assay

FDTD Finite-difference Time-domain

FEM Finite-element Method

HMDS Hexamethyldisilazane

ICP-RIE Inductively-coupled Plasma Reactive-ion Etching

IPA Isopropanol

LOC Lab-on-a-chip

Meep MIT Electromagnetic Equation Propagation

MPB MIT Photonic Bands

MPI Message Passing Interface

PBG Photonic Band Gap

PECVD Plasma-enhanced Chemical Vapor Deposition

PhC Photonic Crystal

PML Perfectly Matched Layer

RF Radio Frequency

RIE Reactive-ion Etching

SEM Scanning Electron Microscope

SOI Silicon-on-insulator

TE Transverse-electric

TIR Total Internal Reflection

TM Transverse-magnetic

Contents

Chapter 1

Introduction

Motivation

Early detection of diseases can in many cases be crucial for effective treatment. For instance, the decline in cancer mortality in the U.S is partially attributed to advances in early detection [4]. Diseases are detected at an early stage by identification and quantification of specific antigens in body fluids such as blood, saliva, or urine. Typically, enzyme-linked immunosorbent assay (ELISA) is used for detecting and measuring the concentration of antigens. However, this method for identification of diseases is laborious, requires significant sample volumes, and is time-consuming [5, 6]. To be cost-effective centralized labs are needed, which in turn increases the total testing time up to several days. The long testing time can be critical for certain diseases, especially if several tests are needed. A different method for detecting antigens is to use label-free detection where the antigens are detected in their natural form. Time-consuming pre- and post-processing are no longer needed, resulting in fast and cost-effective testing. A Lab-on-a-chip (LOC) is a device where all necessary laboratory functions are integrated on a single chip [5]. Using a LOC, analysis of biosamples can be done without a centralized lab, and diagnostics can therefore be provided to a larger population.

Photonic sensors are a promising class of sensors for use in LOC devices. Label-free detection using photonic sensors can be done by measuring the change in the refractive index when specific antigens bind to antibodies placed on the surface of the sensor. Various sensing platforms utilizing refractive index sensing have been demonstrated, including surface plasmon resonance [7], interferometers [8], ring resonators [9] and photonic crystal-based resonators [10]. In this thesis, the latter platform will be investigated. Photonic crystals have been studied extensively since the discovery by Yablonovitch [11] and John [12] in 1987. The frequency range of no propagating electromagnetic modes called photonic band gap found for certain photonic crystals can be utilized to create lossless waveguides around sharp bends and ultracompact resonance cavities [13], paving the way for compact integrated photonic circuits and optical biosensors [14]. Two-dimensional photonic crystals made in silicon-on-insulator is an especially interesting platform for photonic biosensors due to the compatibility with existing fabrication technology used in the CMOS industry. Mass production of sensors can then be cheap and efficient, driving the cost per device down.

Objectives

The main objectives for this project were to design and optimize photonic crystal drop filters using computer simulations and to fabricate and characterize a drop filter made in silicon-on-insulator. Simulation software based on frequency- and time-domain methods were used with the intention of improving key parameters for biosensing performance such as filter quality factor and signal-to-noise ratio. The goal of the fabrication part of the project was to make filters with performance similar to what was found in simulations.

Thesis Overview

Chapter 2 presents the electromagnetic theory needed to understand how photonic crystal drop filter work, and how to use it as an optical biosensor. The theory and working principle behind the simulation software and fabrication methods used to design and make photonic crystal drop filters are presented in chapter 3. In chapter 4, the specific choices of simulation and fabrication parameters are presented and motivated. The results from the simulations, fabrication, and characterization are presented and discussed in chapter 5. The last chapter concludes the results obtained in this thesis and suggests topics for further research.

Chapter 2

Theory

In this chapter, the theory necessary for understanding the working principle of photonic crystal filters and refractive index biosensors is presented. Maxwell's equations are used as a starting point for discussing the properties of light in dielectric media. Photonic crystals are then discussed with emphasis on properties and applications. Lastly, label-free optical biosensing using a photonic crystal filter is explained.

The theory on electromagnetism and photonic crystals is based on the first chapters of Joannopoulos [15].

2.1 Electromagnetism in Dielectric Media

Propagation of light in dielectric media is governed by the Maxwell's equations

$$\boldsymbol{\nabla} \cdot \mathbf{D} = \rho, \tag{2.1}$$

$$\boldsymbol{\nabla} \cdot \mathbf{B} = 0, \tag{2.2}$$

$$\boldsymbol{\nabla} \times \mathbf{E} = -\frac{\partial \mathbf{B}}{\partial t}, \tag{2.3}$$

$$\boldsymbol{\nabla} \times \mathbf{H} = \mathbf{J} + \frac{\partial \mathbf{D}}{\partial t}, \tag{2.4}$$

where $\mathbf{D}$ is the displacement field, $\mathbf{B}$ is the magnetic induction field, $\mathbf{E}$ is the electric field, $\mathbf{H}$ is the magnetic field, ρ is the free charge density and $\mathbf{J}$ is the current density in the material. The derivation of these equations can be found in any introductory text on electromagnetism such as [16] or [17]. Dielectric media without electric current and free charges will be considered in this thesis, simplifying Equation 2.1 and 2.4. Furthermore, the considered materials are assumed to be linear, isotropic and non-dispersive, resulting in the following simplified version of the Maxwell's equations

$$\boldsymbol{\nabla} \cdot [\varepsilon(\mathbf{r})\mathbf{E}(\mathbf{r}, \mathbf{t})] = 0, \tag{2.5}$$

$$\boldsymbol{\nabla} \cdot \mathbf{H}(\mathbf{r}, t) = 0, \tag{2.6}$$

$$\boldsymbol{\nabla} \times \mathbf{E}(\mathbf{r}, t) = -\mu \frac{\partial \mathbf{H}(\mathbf{r}, t)}{\partial t}, \tag{2.7}$$

$$\boldsymbol{\nabla} \times \mathbf{H}(\mathbf{r}, t) = \varepsilon_0 \varepsilon(\mathbf{r}) \frac{\partial \mathbf{E}(\mathbf{r}, t)}{\partial t}. \tag{2.8}$$

ε_0 is the vacuum permittivity, $\varepsilon(\mathbf{r})$ is the dielectric function of the considered material and $\mu = \mu_0$ is the permeability, here taken to be the vacuum permeability. Equations 2.5-2.8 are separable in time and space [18], and the solutions can be written in the form

$$\mathbf{H}(\mathbf{r}, t) = \mathbf{H}(\mathbf{r})\, e^{-i\omega t}, \tag{2.9}$$

$$\mathbf{E}(\mathbf{r}, t) = \mathbf{E}(\mathbf{r})\, e^{-i\omega t}, \tag{2.10}$$

i.e, a vector field varying in space times a harmonic oscillation with frequency ω. By inserting these solutions into the simplified Maxwell's equations (Eq. 2.5-2.8), the equation for a magnetic mode profile $\mathbf{H}(\mathbf{r})$ with frequency ω is obtained:

$$\boldsymbol{\nabla} \times \frac{1}{\varepsilon(\mathbf{r})} \boldsymbol{\nabla} \times \mathbf{H}(\mathbf{r}) = \left(\frac{\omega}{c}\right)^2 \mathbf{H}(\mathbf{r}). \tag{2.11}$$

After $\mathbf{H}(\mathbf{r})$ is found, the electric field can be calculated using Equation 2.8 and 2.10:

$$\mathbf{E}(\mathbf{r}) = \frac{i}{\omega \varepsilon_0 \varepsilon(\mathbf{r})} \boldsymbol{\nabla} \times \mathbf{H}(\mathbf{r}). \tag{2.12}$$

Alternatively, the simplified Maxwell's equations can be combined to find an equation for the electric field mode instead of the magnetic field

$$\boldsymbol{\nabla} \times \boldsymbol{\nabla} \times \mathbf{E}(\mathbf{r}) = \left(\frac{\omega}{c}\right)^2 \varepsilon(\mathbf{r}) \mathbf{E}(\mathbf{r}), \tag{2.13}$$

where the magnetic field can be found by an expression similar to Equation 2.12.

2.1.1 Electromagnetism as an Eigenvalue Problem

Equation 2.11 is an eigenvalue equation where the operator

$$\hat{\Theta} \triangleq \boldsymbol{\nabla} \times \frac{1}{\varepsilon(\mathbf{r})} \boldsymbol{\nabla} \times, \tag{2.14}$$

operates on an eigenmode $\mathbf{H}(\mathbf{r})$ resulting in an eigenvalue, $(\omega/c)^2$, times the eigenmode. Since the curl operator is a linear operator, Equation 2.11 is a linear eigenvalue problem. Furthermore, the operator is Hermitian [15], meaning that the order of operation in an inner product can be swapped without changing the result [19]:

$$(\mathbf{F}, \hat{\Theta}\mathbf{G}) = (\hat{\Theta}\mathbf{F}, \mathbf{G}), \tag{2.15}$$

where $\mathbf{F}$ and $\mathbf{G}$ are arbitrary vector fields. This can be proved for the operator above by performing integration by parts [15]. Formulating Equation 2.11 as an Hermitian eigenvalue equation provides useful insight of the behavior and properties of the modes in the considered system. Eigenvalues of Hermitian operators are real and the eigenmodes corresponding to different eigenvalues are orthogonal [19]. Furthermore, it can be shown that $\hat{\Theta}$ is positive semi-definite [15], making $(\omega/c)^2$ nonnegative and ω real. The modes corresponding to degenerate eigenvalues will on the other hand not be orthogonal. By multiplying each side of Equation 2.11 with $\mathbf{H}(\mathbf{r})$, taking the inner products and solving for $(\omega/c)^2$ one ends up with the Rayleigh-Ritz variational method [19]

$$U_f \triangleq \frac{(\mathbf{H}, \hat{\Theta}\mathbf{H})}{(\mathbf{H}, \mathbf{H})} = \left(\frac{\omega}{c}\right)^2. \tag{2.16}$$

Minimizing the Rayleigh quotient, U_f, yields the smallest eigenvalue $(\omega_0/c)^2$ and the corresponding eigenmode $\mathbf{H}_0(\mathbf{r})$. The Rayleigh-Ritz variational principle can be used to describe the modes in a mixed dielectric medium qualitatively. This is most easily done by rewriting the Rayleigh quotient in terms of the electric field [15]:

$$U_f = \frac{(\boldsymbol{\nabla} \times \mathbf{E}, \boldsymbol{\nabla} \times \mathbf{E})}{(\mathbf{E}, \varepsilon(\mathbf{r})\mathbf{E})} = \frac{\int \mathrm{d}^3\mathbf{r} \, |\boldsymbol{\nabla} \times \mathbf{E}|^2}{\int \mathrm{d}^3\mathbf{r} \, \varepsilon(\mathbf{r}) |\mathbf{E}|^2}. \tag{2.17}$$

U_f is minimized either by minimizing the spatial oscillations of the electric field or by concentrating the electric field in the regions of high dielectric constant, while remaining orthogonal

to the lower-frequency modes. The change in eigenfrequency in response to a small change in dielectric function can be analyzed using perturbation theory [19, 20]. The first order correction to the frequency, $\Delta\omega$, due to a small change in the dielectric function from ε to $\varepsilon + \Delta\varepsilon$ can be shown to be

$$\Delta\omega = -\frac{\omega}{2}\frac{\int \mathrm{d}^3\mathbf{r}\,\Delta\varepsilon(\mathbf{r})|\mathbf{E}|^2}{\int \mathrm{d}^3\mathbf{r}\,\varepsilon(\mathbf{r})|\mathbf{E}|^2}, \tag{2.18}$$

where ω is the eigenfrequency of the eigenmode $\mathbf{E}$ in the unperturbed system. This expression is useful later on when discussing refractive index sensing and sensitivity.

2.1.2 Scaling Invariance of Maxwell's Equations

A useful property of the Maxwell's Equations is that there is no fundamental length scale as long as the system is considered macroscopic, i.e., the equations are invariant under scaling [15]. Consider a material with dielectric function $\varepsilon(\mathbf{r})$ where the mode $\mathbf{H}(\mathbf{r})$ is an eigenmode of Equation 2.11 with eigenfrequency ω. If the dielectric function is scaled by a factor s, $\varepsilon(\mathbf{r}') = \varepsilon(\mathbf{r}/s)$, the eigenmode will be scaled by the same factor and the eigenfrequency will be $\omega' = \omega/s'$. This is useful when designing photonic crystal devices, since the operating frequency range of the device can be chosen by adjusting the lattice constant of the crystal.

It is convenient to define a fundamental length scale for the system considered and scale all other physical quantities accordingly. The suitable length scale in a photonic crystal will typically be the lattice constant a. The dimensionless frequency and wave number in terms of a are $\omega a/2\pi c$ and $ka/2\pi$, respectively. The photonic crystal band gap size is also useful to express as the gap-midgap ratio, $\Delta\omega/\omega_m$, where ω_m is the frequency in the middle of the band gap and $\Delta\omega$ is the frequency width of the band gap. Both will be scaled by the same factor when scaling the dielectric function, making the band gap size independent of the lattice constant of the crystal.

2.2 Photonic Crystals

Structures with periodic dielectric function are called photonic crystals (PhCs) in analogy with crystalline materials where the Coulomb potential is periodic [21]. Some periodic dielectric functions give rise to a photonic band gap (PBG) where no propagating modes exist, similar to the electronic band gap in semiconductors and insulators. In this section, the origin of the photonic band gap will be discussed together with properties and applications of two-dimensional photonic crystals.

2.2.1 Discrete Translation Symmetry

Photonic crystals are materials where the dielectric function has a discrete translation symmetry meaning that $\varepsilon(\mathbf{r}) = \varepsilon(\mathbf{r}+\mathbf{R})$ where $\mathbf{R}$ is any integral multiple of the periodicity of the system. The lattice considered in this thesis is the two-dimensional triangular Bravais lattice (also known as the hexagonal lattice), where every lattice point makes an equilateral triangle with the neighbouring lattice points. The triangular lattice with its translation vectors $\mathbf{a}_1$ and $\mathbf{a}_2$, and the unit cell spanned by the translation vectors are shown in Figure 2.1a. Unit cells containing a single lattice point are called primitive unit cells. The corresponding lattice vectors are therefore called primitive lattice vectors. The primitive lattice vectors of the triangular lattice are $\mathbf{a}_1 = a/2\hat{\mathbf{x}} + \sqrt{3}a/2\hat{\mathbf{y}}$ and $\mathbf{a}_2 = a/2\hat{\mathbf{x}} - \sqrt{3}a/2\hat{\mathbf{y}}$, where a is the distance between neighbouring lattice points. Dielectric functions with triangular periodicity will therefore be invariant under translation along the translation vector

$$\mathbf{R} = m_1\mathbf{a_1} + m_2\mathbf{a_2}, \quad \text{where } m_1, m_2 \in \mathbb{Z}. \tag{2.19}$$

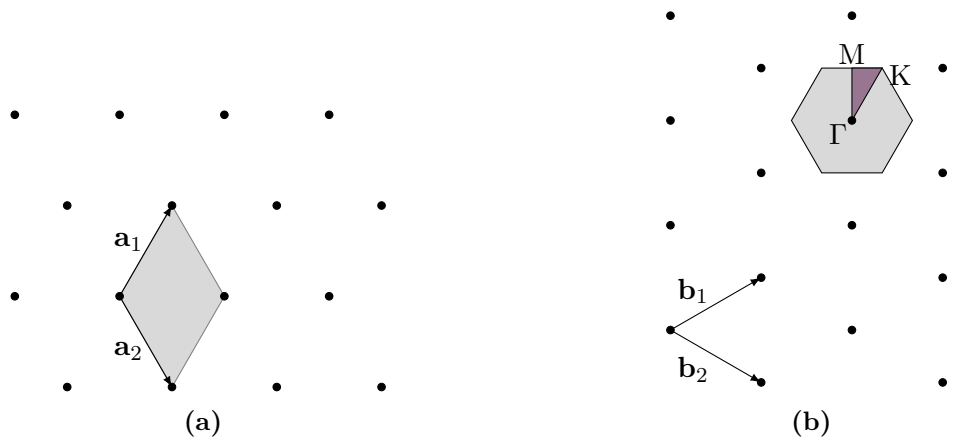

Figure 2.1: (a) The two-dimensional triangular Bravais lattice. The primitive lattice vectors $\mathbf{a}_1$, $\mathbf{a}_2$ and the primitive cell spanned by the vectors are shown. (b) The reciprocal lattice of the lattice in (a). The reciprocal lattice vectors $\mathbf{b}_1$ and $\mathbf{b}_2$ are shown together with the 1st Brillouin zone (grey), the irreducible BZ (colored) and the high symmetry directions Γ, M and K.

It is convenient to define the reciprocal lattice with primitive vectors $\mathbf{b}$ defined such that $\mathbf{a}_i \cdot \mathbf{b}_j = 2\pi\delta_{ij}$, where δ_{ij} is the Kronecker delta. Each point in the reciprocal lattice is then defined by the vector $\mathbf{G} = l_1\mathbf{b}_1 + l_2\mathbf{b}_2$, where $l_1, l_2 \in \mathbb{Z}$. The reciprocal lattice of the triangular lattice is shown in Figure 2.1b together with the reciprocal lattice vectors and the unit cell spanned by the vectors. Additionally, one defines the 1st Brillouin zone (BZ) in reciprocal space as the primitive unit cell where all points in the cell is closer to the lattice point in the cell than to any other lattice point. Furthermore, the irreducible BZ is the 1st BZ reduced by the symmetries of lattice. Both the 1st BZ and the irreducible BZ are shown in Figure 2.1b and the high symmetry points Γ, M and K are highlighted.

The solutions to Equation 2.11 for a periodic dielectric function are found by using the Bloch theorem [15, 21, 22]. The eigenmodes of the system, Bloch modes, are then given as

$$\mathbf{H}_\mathbf{k}(\mathbf{r}) = e^{i\mathbf{k}\cdot\mathbf{r}}\mathbf{u}_\mathbf{k}(\mathbf{r}), \tag{2.20}$$

i.e., plane waves modulated by a periodic function in the lattice $\mathbf{u}_\mathbf{k}(\mathbf{r}) = \mathbf{u}_\mathbf{k}(\mathbf{r} + \mathbf{R})$. For wave vectors $\mathbf{k}$ outside of the 1st BZ one can always find a reciprocal lattice vector $\mathbf{G}$ such that $\mathbf{k}' = \mathbf{k} + \mathbf{G}$ is inside without changing the eigenfrequency of the mode [15, 21]. It is therefore sufficient to consider the 1st irreducible BZ when finding solutions to Equation 2.11 in a periodic medium.

2.2.2 Photonic Crystal Band Gaps

The physical origin of the PBG can be illustrated considering a structure consisting of alternating layers of medium with low and high relative permittivity, ε_l and ε_h, shown in Figure 2.2a. The dispersion relation for this structure is shown in Figure 2.2c, and a frequency band gap clearly appears at $ka/2\pi = 0.5$. The mode at the bottom of the band gap will have its electric field concentrated in the regions of high dielectric constant according to the variational principle (Eq. 2.17) as shown in Figure 2.2a. The mode at the top of the band gap has to be orthogonal to the lower-frequency mode and will therefore be phase shifted $\pi/2$ compared to the other mode in this one-dimensional system. This mode will have a higher concentration of the electric field in the regions of low dielectric constant, as seen in Figure 2.2b. The frequency will therefore be higher than for the other mode according to the variational principle.

The photonic band gap allows for control of light propagation at length scales comparable to the wavelength of the light and can be used to create compact optical devices such as filters

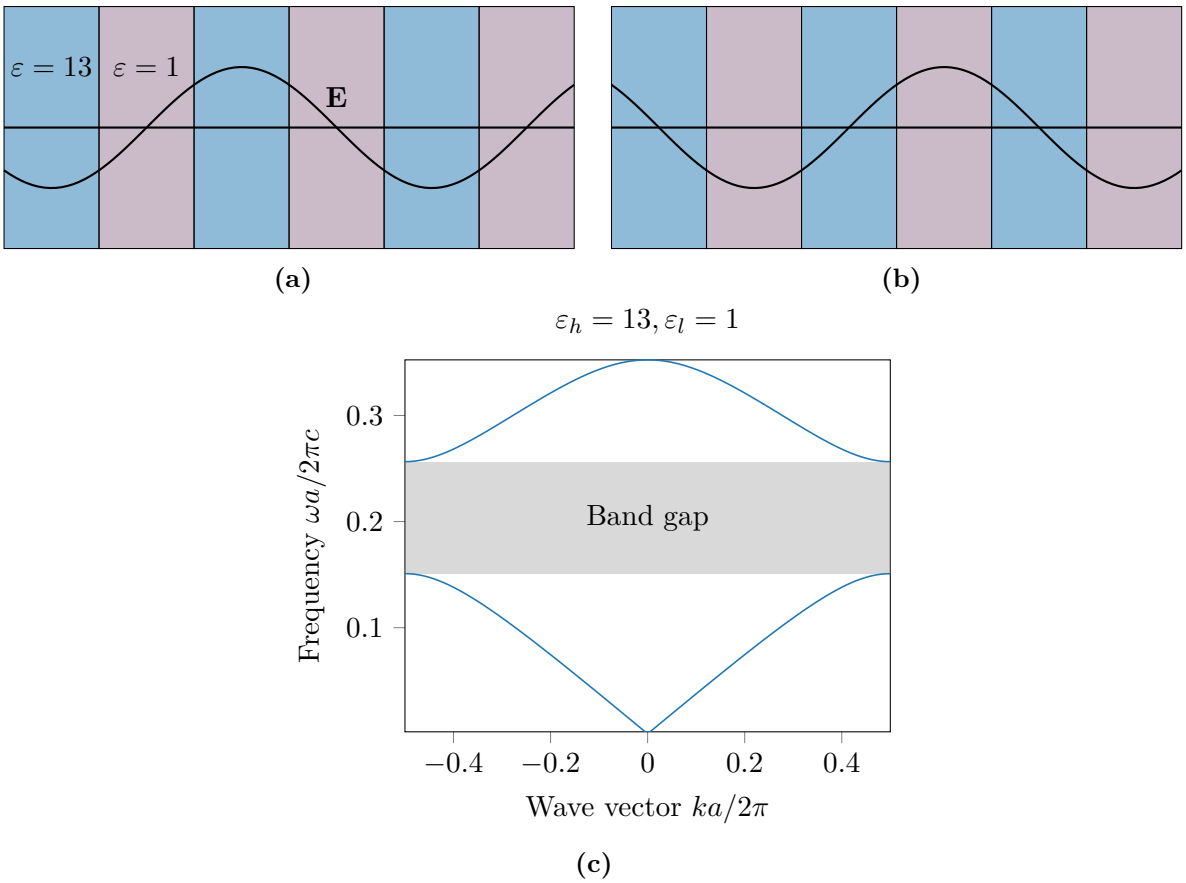

Figure 2.2: The electric field for light with wave vector $ka/2\pi = 0.5$ is shown in (a) and (b) for a layered material where each layer have a thickness a. The diagram in (c) shows the dispersion relation for the layered material, with a band gap appearing at $ka/2\pi = 0.5$. The mode at the bottom of the band gap is shown in (a), where the electric field is most concentrated in the material with high permittivity. The mode at the top of the band gap is shown in (b), and the electric for this mode is more concentrated in the material with low permittivity.

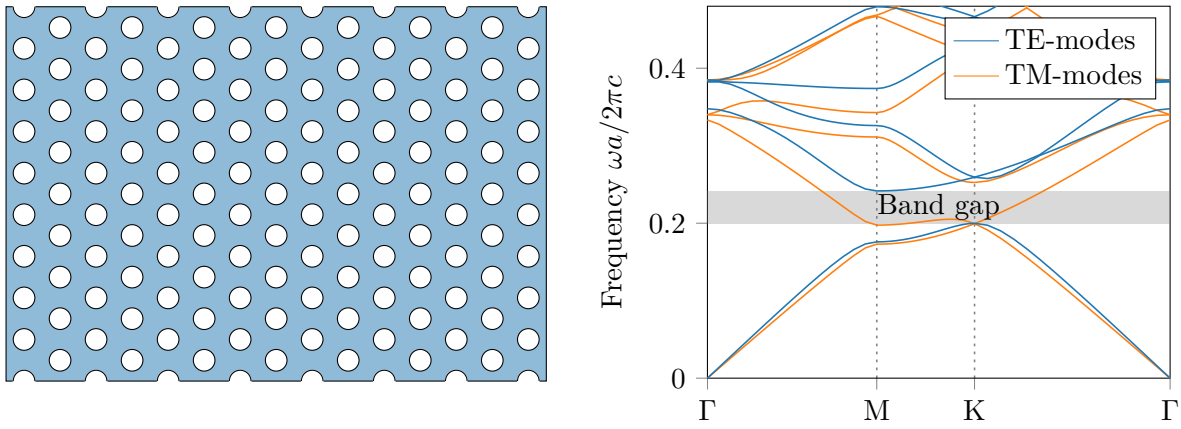

(a) **(b)**

Figure 2.3: (a) 2D triangular photonic crystal of air holes in silicon, where the air hole radius is $0.26a$. (b) The band structure for the structure in (a), where a band gap is found for TE-modes.

and beam splitters. The device investigated in this thesis is a silicon slab with air holes placed in a triangular lattice. The light confining properties can be approximated by a 2D PhC of air holes in a silicon slab with infinite thickness (Fig. 2.3a). The 2D PhC has mirror symmetry in the crystal plane and the modes in the crystal are either transverse-electric (TE) or transverse-magnetic (TM) [15]. TE means that the electric field is parallel to the crystal plane, while TM means that the magnetic field is parallel to the crystal plane. Since the frequency of a mode is governed by the interaction between the electric field and the dielectric function according to the variational principle (Eq. 2.17), it is expected that the dispersion relation for the two types of modes are generally different as shown in the band diagram (Fig. 2.3b) for the structure in Figure 2.3a. A band gap appears for TE-modes in the frequency range (0.2, 0.24), while there are no band gaps for TM-modes at any frequency range.

The dispersion relation for periodic systems are found by inserting the Bloch mode (Eq. 2.20) into Equation 2.11 with the resulting equation

$$\hat{\Theta}_{\mathbf{k}}\mathbf{u}_{\mathbf{k}}(\mathbf{r}) = \left(\frac{\omega}{c}\right)^2 \mathbf{u}_{\mathbf{k}}(\mathbf{r}), \tag{2.21}$$

where a new Hermitian operator is defined

$$\hat{\Theta}_{\mathbf{k}} \triangleq (i\mathbf{k} + \boldsymbol{\nabla}) \times \frac{1}{\varepsilon(\mathbf{r})}(i\mathbf{k} + \boldsymbol{\nabla}). \tag{2.22}$$

Solving the Hermitian eigenvalue equation for a given periodic medium gives the dispersion relation $\omega(\mathbf{k})$.

2.2.3 Photonic Crystal Slabs

As mentioned, the device considered in this thesis is a silicon slab with air holes placed in a triangular lattice (Fig. 2.4a). Light propagation in this device will be governed by the photonic crystal band gap in the crystal plane, while index guiding will determine the light confinement in the slab [15]. The light in the air surrounding the silicon slab will have the dispersion relation:

$$\omega(\mathbf{k}) = \frac{c}{\sqrt{\varepsilon}}\sqrt{\mathbf{k}_{\parallel}^2 + \mathbf{k}_{\perp}^2}, \tag{2.23}$$

where the wave vector $\mathbf{k}$ have been decomposed into components parallel and perpendicular to the silicon-air interface. If $\mathbf{k}_{\perp}$ is imaginary, the light will decay exponentially away from

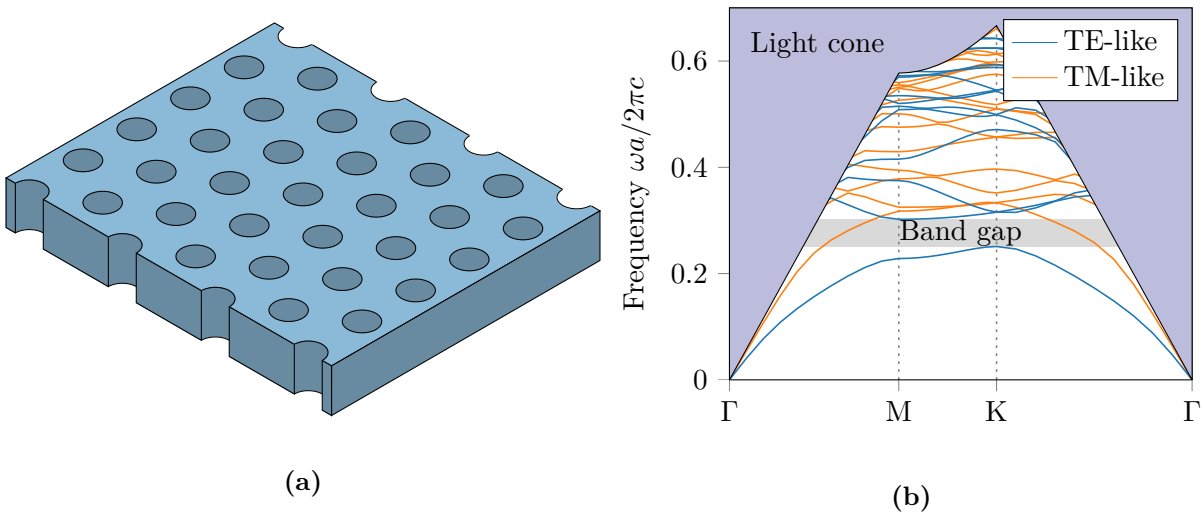

(a) **(b)**

Figure 2.4: (a) Photonic crystal of air holes in a silicon slab where the hole radius is $0.26a$. (b) The band structure for the structure in (a). An incomplete band gap for TE-like modes is visible. The continuum of modes not confined to the silicon slab by TIR is referred to as the light cone.

the silicon slab where it is confined by total internal reflection (TIR). On the other hand, if $\omega \geq c|\mathbf{k}_{\parallel}|/\sqrt{\varepsilon}$, the normal component of the wave vector is real. Above this threshold, there exists a continuum of modes propagating in the air. These modes will leak out of the silicon, and the photonic crystal slab will therefore not have a complete band gap such as two-dimensional photonic crystals (Fig. 2.3b). The continuum of leaky modes above this frequency, in the light cone, has to be included in the band structure, as shown in Figure 2.4b. The finite thickness of the slab also makes the classification of modes as TE or TM inaccurate. For an air-bridge system with air above and below the silicon, the modes can be categorized as TE- or TM-like depending on their symmetry with respect to the mirror plane in the middle of the slab [15]. TE-like modes are even upon reflection, while TM-like modes are odd. In systems without this mirror symmetry, such as photonic crystal made in silicon-on-insulator (SOI), the different polarizations are allowed to couple, and the band gap will disappear. However, if the dielectric contrast is strong, this coupling can be assumed to be weak [15].

2.2.4 Defects and Resonance Cavities

Linear Defect Waveguides

Without alterations, the photonic crystal is only a directional mirror for certain frequencies blocked by the PBG. However, optical components can be made by adding defects to the photonic crystal. If an entire row of air holes is removed from the silicon-air photonic crystal (Fig. 2.5a), a waveguide is made. Light with frequency in the photonic band gap can then be guided from one end of the waveguide to the other. The dispersion relation for a linear defect waveguide can be calculated by using the same equation as for an ordinary photonic crystal (Eq. 2.21). However, the translation symmetry is broken in one direction, making the BZ one-dimensional [23]. The band structure for the linear defect waveguide is found by calculating the bands in the symmetry direction and adding the bulk bands in the same direction for the corresponding photonic crystal [24].

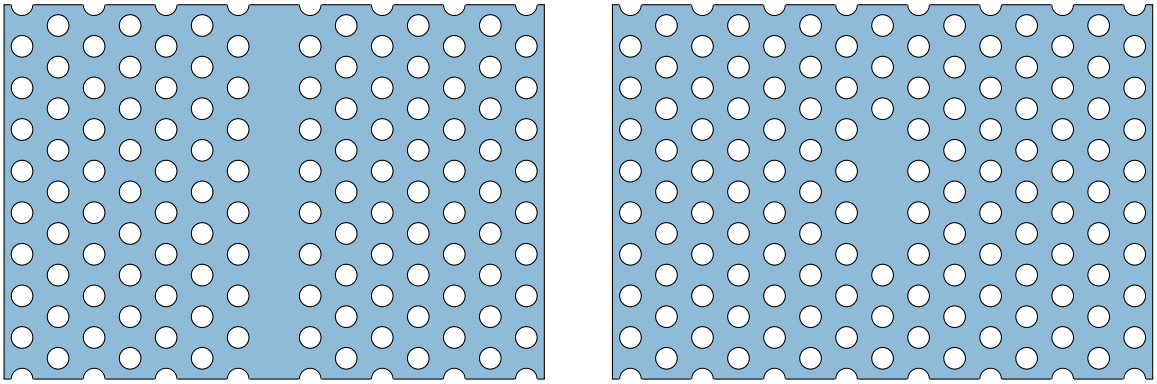

(a) **(b)**

Figure 2.5: (a) Photonic crystal waveguide made by removing a row of holes in the crystal. (b) A linear defect cavity made by removing three air holes.

Linear Cavities

A similar idea to the linear defect waveguide is to remove several adjacent air holes, but not an entire row. In analogy to the linear defect waveguide, light is allowed to propagate in the defect. However, the light is reflected by the PBG at the ends of the cavity, and thus the cavity supports standing waves compared to the waveguide where plane waves are supported.

For a resonance mode with frequency ω_0 one can define the quality factor as $Q = \omega_0\tau/2$, where the electric field energy decays by a factor $1/e$ after time τ. The quality factor can also be formulated as $Q = \omega_0/\Delta\omega$, where $\Delta\omega$ is the frequency bandwidth of the resonance mode. A high Q resonance will be trapped in the cavity for a long time and have a narrow bandwidth. The modes supported in the cavity will not be able to propagate in the photonic crystal due to the PBG. It is therefore no surprise that linear cavities in a 2D photonic crystal have a high quality factor [2]. In more practical systems, such as an air-bridge or SOI-photonic crystal, the light will be confined by the photonic band gap in the crystal plane and by TIR out of the crystal plane. The total quality factor is then related to the quality factor in-plane and out-of-plane, Q_{xy} and Q_z respectively, by

$$\frac{1}{Q_{\text{total}}} = \frac{1}{Q_{xy}} + \frac{1}{Q_z}. \tag{2.24}$$

If the loss out of plane is much larger than the loss in the photonic crystal plane, $Q_z \ll Q_{xy}$, the total Q-factor will be dominated by Q_z according to Equation 2.24. It is therefore of great importance to consider both losses when designing resonance cavities in photonic crystal slabs. Light confined to a small volume compared to its wavelength can be decomposed into a distribution of plane waves with wave vector $\mathbf{k}$ (see Fig. 2.6), according to Fourier analysis. If the width of the distribution is too broad, a portion of the light will not be confined to the slab by TIR. Consequently, the quality factor is dominated by the out-of-plane loss, and very high-quality factor cavities are difficult to design [25].

2.2.5 Photonic Crystal Drop Filter

By combining linear defect cavities and PhC-waveguides one can make different optical components. If a high-quality factor cavity is placed below a waveguide, a notch filter is made. Frequencies close to the resonance frequency of the cavity is attenuated strongly and the frequencies are filtered out of the frequency spectrum for the filter. If another waveguide is added below the resonance cavity, a drop filter is made. In this device, light with frequency close to the resonance is dropped from the bus waveguide to the receiver waveguide. The resulting

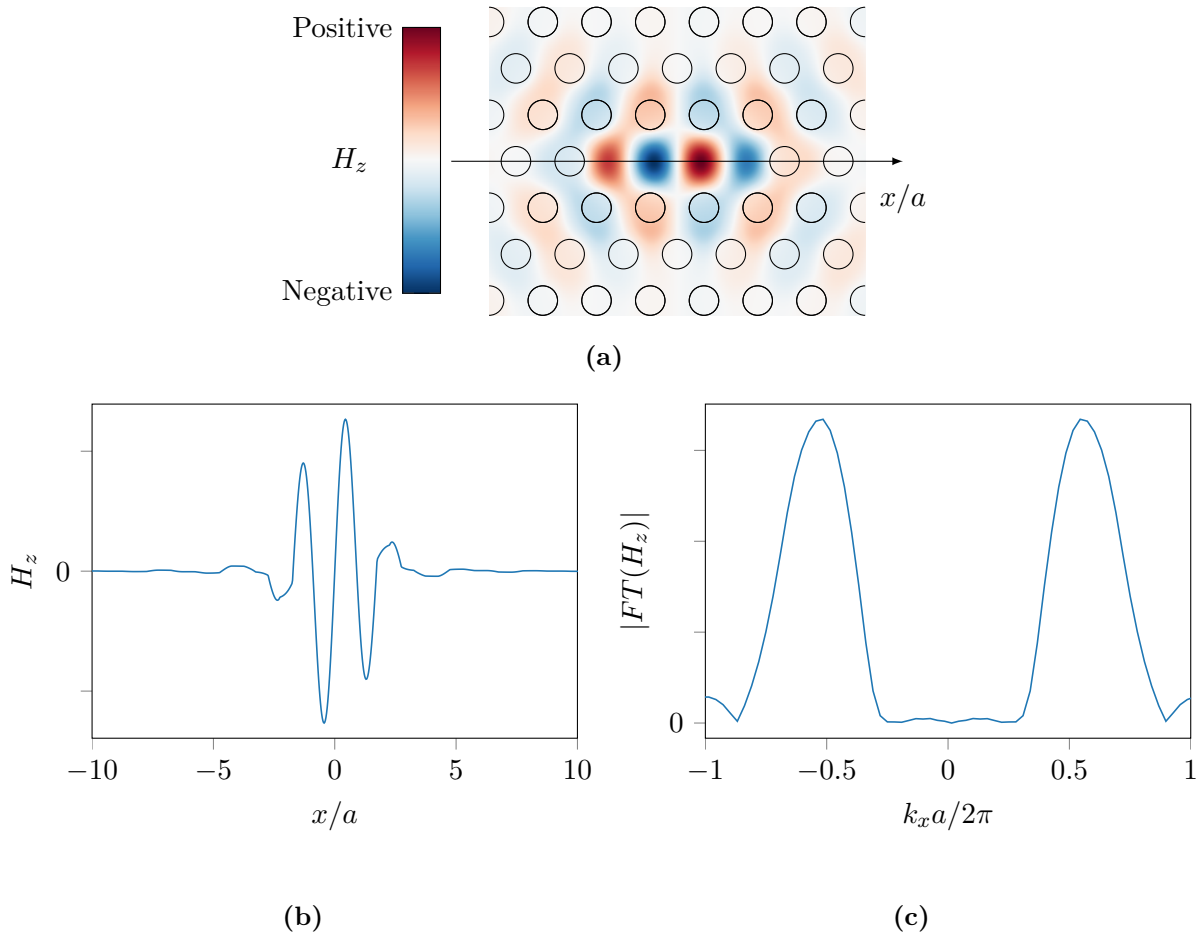

Figure 2.6: (a) The magnetic field in the out-of-plane direction for the fundamental mode of the linear defect waveguide in Figure 2.5b. (b) The magnetic field in the z direction along the center of the cavity. (c) The absolute value of the Fourier transform of the field in (b).

frequency spectrum consists of a single peak at the resonance frequency of the cavity. For simplicity, a system consisting of a standing wave resonator placed between a bus and a receiver waveguide is considered (shown in Figure 2.7). The amplitudes of the incoming and outgoing waves at the four different ports, $s_{\pm i}$, can be determined by using temporal coupled-mode theory (see [15, Chapter 10]) and assuming weak coupling [26]. In the weak coupling limit, the decay rate, $1/\tau_{\mathrm{WG}}$, is the dominating mechanism for power exchange between the waveguides and the resonator. The time evolution of the amplitude in the resonator, a, can be shown to be [26]

$$\frac{\mathrm{d}a}{\mathrm{d}t} = \left(i\omega_0 - \frac{1}{\tau_{\mathrm{air}}} - \frac{2}{\tau_{\mathrm{WG}}} \right) a + \kappa \sum_{i=1}^{4} s_{+i}, \tag{2.25}$$

where ω_0 is the resonance frequency, $1/\tau_{\mathrm{air}}$ and $1/\tau_{\mathrm{WG}}$ are the decay rates into the surrounding air and the adjacent waveguides (see Fig. 2.7), and κ is the input coupling coefficient for the modes propagating towards the resonator. The decay rate into the two waveguides are assumed to be equal, which can easily be realized by placing them an equal distance away from the resonator. The interpretation of Equation 2.25 is relatively straight forward. The amplitude in the resonator oscillates with a frequency ω_0, and after a time $\mathrm{d}t$ decays to either air or the adjacent waveguides by an amount equal to the decay rate times the amplitude in the resonator. Additionally, light enters the resonator from both waveguides by an amount proportional to the amplitude of the modes moving towards the resonator. The filter response of the system can be found by using power conservation and setting the amplitudes of the incoming waves [26]. We consider a system where the resonator is excited by light coming from the left in the bus waveguide, $s_{+1} = e^{i\omega t}$, while the other incoming amplitudes are set to zero. The total intensity transferred from the bus to the receiver is then

$$D(\omega) = \frac{|s_{-3}|^2 + |s_{-4}|^2}{|s_{+1}|^2} = \frac{\frac{2}{\tau_{\mathrm{WG}}^2}}{\left(\frac{1}{\tau_{\mathrm{air}}} + \frac{2}{\tau_{\mathrm{WG}}} \right)^2 + (\omega - \omega_0)^2}. \tag{2.26}$$

This is the equation for a Lorentzian peak with maximum at $\omega = \omega_0$. The decay rates are related to the quality factors as described in Section 2.2.4. At resonance the dropped intensity can be written

$$D(\omega_0) = \frac{2}{\left(\frac{Q_{\mathrm{WG}}}{Q_{\mathrm{air}}} + 2 \right)^2}. \tag{2.27}$$

A couple of conclusions can be drawn from this equation. When $Q_{\mathrm{air}} \gg Q_{\mathrm{WG}}$, the total power dropped to the receiver is close to 50% (a small fraction is lost to the surroundings) and the total Q-factor is dominated by the decay rate between cavity and waveguides from Equation 2.24. Increasing the dropped intensity comes at a cost of lowering the total Q-factor. In the case where $Q_{\mathrm{air}} \ll Q_{\mathrm{WG}}$, the dropped intensity is almost 0. The light coupled to the resonator from the bus decays to the surrounding air before it is able to couple to the receiver. Q_{air} will therefore set the limit for the transmission and total Q-factor. If Q_{air} is sufficiently high, the waveguides can be placed farther away from the resonator, thus increasing Q_{WG} and Q_{total}, while still having a fairly large transmission.

Typically, only the light propagating to the right in the receiver, through port 4, is of interest. From Equation 2.27 it is clear that 25% dropped intensity to the right port in the receiver is the theoretical maximum for the four-port system in Figure 2.7. By adding mirrors in both the bus and the receiver, the intensity at port 4 can be further improved [27]. Assuming perfect mirrors and neglible loss, $Q_{\mathrm{air}} \gg Q_{\mathrm{WG}}$, the dropped intensity at the right port is

$$|s_{-4}|^2 = \frac{1 + \cos\alpha}{2}, \tag{2.28}$$

where α is the phase introduced by reflection at the mirror and propagation from the cavity to the mirror and back. For a symmetrical cavity mode, the phase is $\alpha = \pi - kd$, where k is the

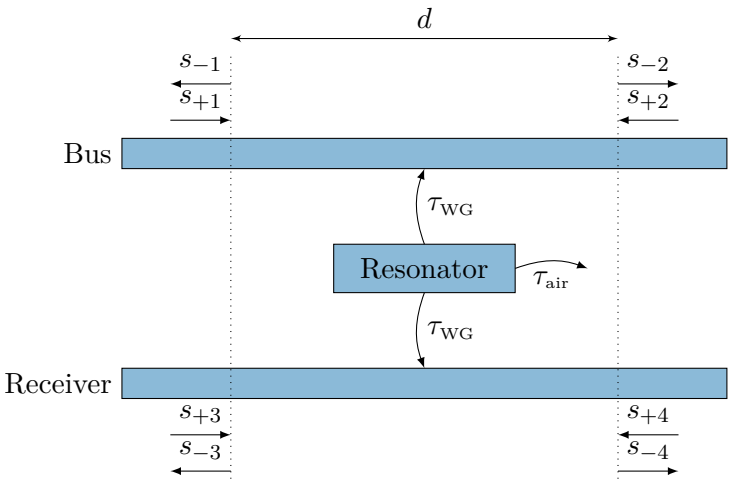

Figure 2.7: Drop filter made by placing waveguides above and below a standing wave resonator. Adapted from [26].

propagation constant in the waveguide and d is the distance from the center of the cavity to the mirror and back.

2.3 Biosensing

Biosensors are devices able to detect and convert a biological signal into an electrical signal. The biological signal of interest will typically be specific molecules found in body fluids such as blood, saliva, or urine. Examples of such biosensors are pregnancy tests and glucose tests for diabetics. Among the most common transduction principles are optical transduction where light is used to convert the biological signal to an electrical signal. The use of light has several benefits including the capability of remote sensing and multiplexed sensing within a single device [6]. Optical biosensing techniques can further be divided into two major categories: fluorescence-based detection and label-free detection [6]. The first detection principle can be extremely sensitive with a detection limit close to a single molecule. However, fluorescence-based detection is time-consuming and expensive due to the laborious labeling process. On the other hand, label-free biosensors can provide fast, direct, and cost-effective sensing with a relatively small sample volume. Label-free detection based on a change in the refractive index is the detection principle that will be discussed and tested in this project.

2.3.1 Refractive Index Sensing

The frequency shift of a resonance mode due to a change in the refractive index found using perturbation theory (Eq. 2.18) can be utilized for biosensing. Resonance modes confined to a silicon slab will have an evanescent tail in the surrounding media, and the frequency of the mode will therefore change when the surrounding medium is changed (see Fig. 2.8b). Selective biosensing can be achieved using this sensing principle by biofunctionalization of the silicon surface. Antigen-specific antibodies are placed on the silicon surface by silanization. When a solution containing the antigens is placed above the silicon surface, the antigens will bind specifically to the antibodies as illustrated in Figure 2.8a. The change in the refractive index above the silicon surface will depend on the concentration of antigens in the solution, and the frequency shift can be related to the concentration of antigens in the solution.

The performance of a refractive index biosensor is determined by the refractive index sensitivity, the magnitude of wavelength shift versus the change in the refractive index of the surrounding medium and the detection limit, i.e., the minimum amount of antigens detectable

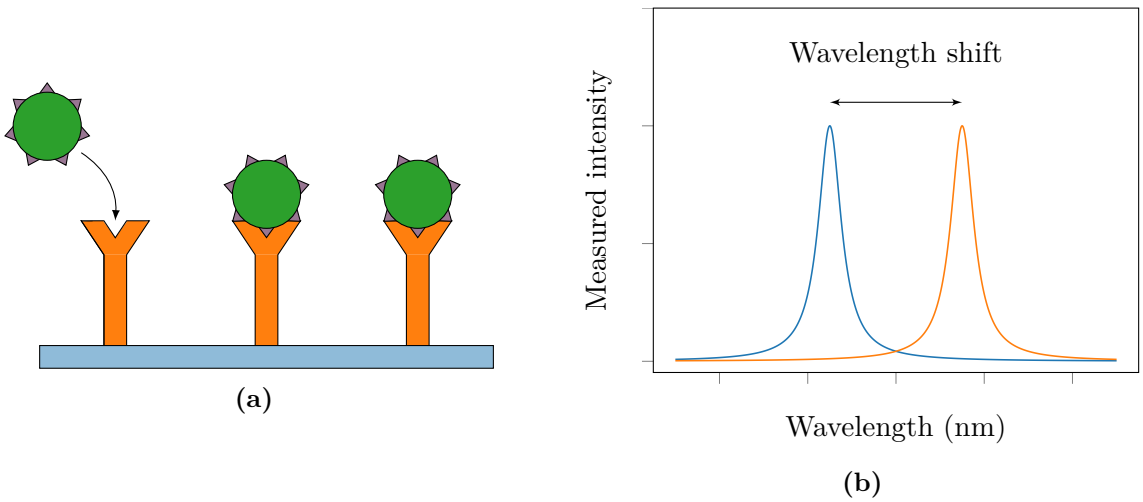

(a) (b)

Figure 2.8: (a) Binding of specific antigens to antibodies placed on the silicon surface. (b) Wavelength shift for a resonance mode where the refractive index of the surrounding media has changed.

by the sensor. The refractive index sensitivity is determined by how much the resonance mode is concentrated in the region where the refractive index changes as can be seen from perturbation theory (Eq. 2.18). Furthermore, the detection limit, DL, can be stated as

$$DL = \frac{R}{S}, \tag{2.29}$$

where R is the sensor resolution and S is the sensitivity of the biosensor [28]. It is therefore also important to consider the sensor resolution in addition to the sensitivity. The sensor resolution depends on several parameters, such as noise in the photodetector, noise in the light source, fabrication imperfections, the quality factor of the resonator, and the signal-to-noise ratio for the resonance peak [28]. The photonic crystal drop filter designed in this project will be used as a refractive index biosensor, and the quality factor and signal-to-noise ratio of the filter will be taken into consideration during design to improve the detection limit.

Chapter 3

Simulation and Fabrication Methods

The methods and tools used in this master's project are presented in this chapter. First, the different techniques used for solving electromagnetic problems are presented, followed by a short description of the different simulation software used for designing photonic crystal drop filters. The working principles and properties of the fabrication and characterization tools used when making photonic crystal devices are then explained.

3.1 Computational Electromagnetism

The three main problems solved in computational electromagnetism are frequency-domain eigenproblems, frequency-domain response and time-domain simulations [15].

3.1.1 Frequency-domain Eigenproblems

Finding the dispersion relation $\omega(\mathbf{k})$ in a given system is done by solving the eigenvalue problem (Eq. 2.11). For photonic crystals, the eigenvalue problem is periodic, and only the unit cell needs to be considered as long as the Bloch mode satisfies the transversality condition [15].

The eigenvalue problems (Eq. 2.11 or Eq. 2.21) are solved on a computer by discretizing space and the differential operators. The resulting linear system will take the form $A\mathbf{x} = \omega^2 B\mathbf{x}$, and solving this system yields the eigenfrequencies and eigenmodes of the system. With space discretized into N grid points, both A and B will be $N \times N$ matrices. The exact solution of the linear system above can be found in $O(N^3)$ time [29], which can be very time-consuming for 3D systems. Instead, an iterative eigensolver can be used to find the n lowest eigenvalues and eigenmodes in $O(N)$ time for the Hermitian eigenproblem as long as $n \ll N$ [29]. This can for instance be done by minimization of the Rayleigh quotient (Eq. 2.16) using a plane-wave basis [15, 30]. Non-periodic systems such as linear defect waveguides can be solved by a periodic solver by using the supercell approximation [24].

3.1.2 Frequency-domain Response

It is often of interest to find the response in a system to a constant frequency source. This is done by calculating the steady state electric field $\mathbf{E}$ (and magnetic field $\mathbf{H} = -\frac{i}{\omega\mu_0}\mathbf{E}$) for the given source $\mathbf{J}(\mathbf{r})\, e^{-i\omega t}$ using the eigenvalue equation (Eq. 2.13) with the current added

$$\left((\boldsymbol{\nabla} \times \boldsymbol{\nabla} \times) - \frac{\omega^2}{c^2}\varepsilon(\mathbf{r}) \right) \mathbf{E}(\mathbf{r}) = i\omega\mu_0 \mathbf{J}(\mathbf{r}). \tag{3.1}$$

In a similar manner as for the frequency-domain eigenproblems, the domain is discretized into N grid points resulting in a matrix equation in the form $A\mathbf{x} = \mathbf{b}$. The system can be solved in $O(N^2)$ time in general using iterative methods [29]. Transmission calculations, such as those

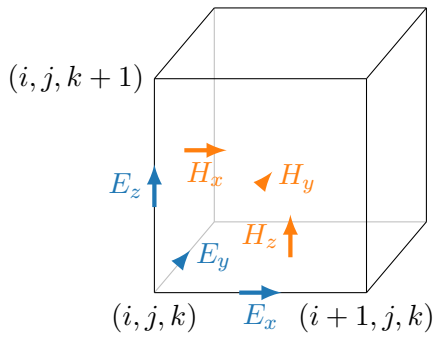

Figure 3.1: 3D Yee grid often used in FDTD simulations. The grid is staggered such that the different field components at a point (i, j, k) are not at the same position.

relevant for photonic crystal filters, require special treatment of the field at the edge of the computational region for the calculations to be correct. This is usually taken care of by placing a perfectly matched layer (PML) around the computational region which absorbs the field with no reflection [15].

3.1.3 Time-domain Simulations

The last method is to propagate the electric and magnetic fields in a structure by using the time-dependent Maxwell equations (Eq. 2.5-2.8). The finite-difference time-domain (FDTD) method is the most common technique using this principle [15]. Time and space are discretized in a grid, and finite differences are used instead of differentiation. The electric field at a time t is often calculated using the electric field at $t - \Delta t$ and the magnetic field at $t - \Delta t/2$. The spatial discretization is slightly more involved, but a Yee grid [31] is often used where the different components of each vector are placed on different locations in the grid (see Fig. 3.1) simplifying divergence and curl operations as well as satisfying physical boundary conditions naturally [32].

The sources used in FDTD simulations are not limited to constant frequency sources as were the case for frequency-domain simulations. One can therefore calculate the transmission and reflectance through a photonic crystal device for a range of frequencies at the same time by using a short light pulse and convert the time signals to frequency response using the Fourier transform. The frequency resolution in a time-domain simulation is inversely proportional to the simulation time according to the Fourier reciprocity theorem. Narrow frequency responses such as for high quality factor resonators can then be very time-consuming to simulate using FDTD, and frequency-domain simulations may be more suitable. Additionally, the time-step size must be proportional to the spatial resolution to maintain numerical stability meaning that the overall number of calculations increases rapidly with increased resolution. PML is also used in FDTD to take care of finite boundaries without reflections.

3.2 Simulation Software

The numerical packages and simulation programs used in this project are COMSOL Multiphysics, MIT Electromagnetic Equation Propagation (Meep), and MIT Photonic Bands (MPB).

3.2.1 COMSOL Multiphysics

COMSOL Multiphysics is, as the name implies, a software platform for modeling and simulating devices in a diverse set of scientific and engineering fields. Photonic devices such as photonic crystal filters can be designed and simulated using the *Wave Optics Module*. Included in this module is modal analysis, which can be used for effective refractive index calculations and

boundary mode analysis, which can be used to calculate the transmission and reflectance in photonic devices. These different analysis methods are frequency-domain methods where the finite-element method (FEM) is used to discretize space into a non-rectangular grid. The use of FEM when discretizing makes it possible to represent geometries such as circles far more accurately without increasing the number of grid points compared to a standard rectangular grid. COMSOL will be used for effective index calculations and for simulating transmission through photonic crystal filters.

Short tutorials on transmission calculations and effective index calculations in COMSOL are given in Appendix A.

3.2.2 MIT Photonic Bands

MPB is an open-source software package for solving frequency-domain eigenproblems in periodic dielectric structures. This is done by using a preconditioned conjugate-gradient minimization of the Rayleigh quotient (Eq. 2.16) for the periodic Bloch operator in Equation 2.22 [30]. MPB comes with a Python interface for scripting and message passing interface (MPI) for efficient parallel computing. MPB is used in this project to calculate band structures for photonic crystals and photonic crystal waveguides. For the latter, the supercell approximation will be used.

A tutorial on calculating the band structure for a photonic crystal waveguide is given in Appendix C.

3.2.3 MIT Electromagnetic Equation Propagation

Meep is an open-source software package for electromagnetic simulations using the FDTD method [32]. This allows for calculating transmission and reflectance spectra for photonic devices, in addition to analysis of resonant modes. Meep provides scripting interface in Python and supports parallel computing with MPI. The latter is very useful when doing large 3D simulations on supercomputers. Mirror and rotational symmetries are supported, which can be exploited to reduce simulation time significantly for symmetric systems. Analysis of resonant modes with high quality factors can be done efficiently in Meep using an included library called Harminv. This library uses a filter diagonalization method suggested by Mandelshtam et al. [33] to decompose time signals into exponentially decaying sinusoids. This method is not limited by the Fourier reciprocity theorem in the same way as curve fitting a Lorentzian to a transmission spectrum is, resulting in an accurate calculation of the quality factor in almost an order of magnitude fewer time steps [32].

In Appendix B, tutorials showing how to analyze resonant modes and simulate transmission through a drop filter are given.

3.3 Fabrication and Characterization

The instruments and methods used to fabricate and characterize photonic crystals and waveguides are presented in this section. Additionally, the material system used in the fabrication will be discussed briefly.

3.3.1 Silicon-on-insulator

The silicon-on-insulator material system is regarded as one of the most promising candidates for large scale manufacturing of integrated photonic circuits [34]. There are three main reasons for this. Firstly, crystalline silicon has a very low absorption for wavelengths longer than 1200 nm, including the wavelengths around 1550 nm which are commonly used in telecom. Thus, key optical components such as lasers and detectors already exist for the same wavelength range.

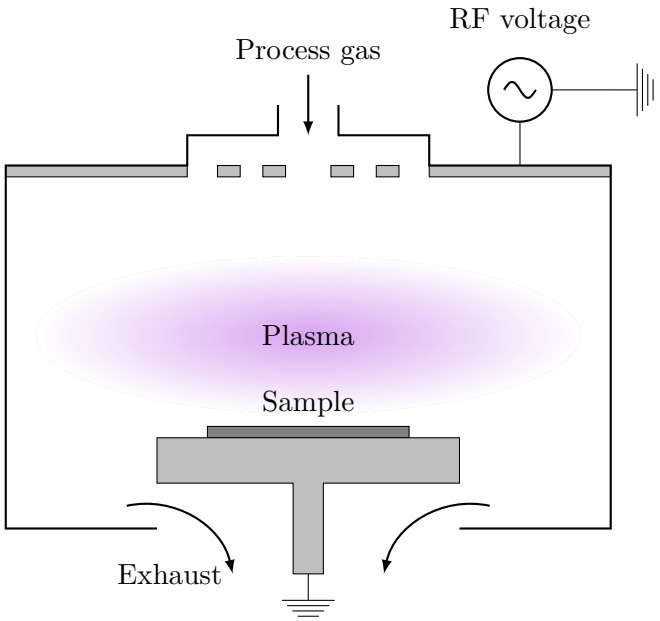

Figure 3.2: Schematic of a PECVD reaction chamber.

Secondly, the high refractive index contrast between silicon and silicon dioxide (SiO_2) allows for strong confinement of light. For instance can light with wavelength 1550 nm be confined in a SOI strip waveguide with cross-section 220x520 nm [34]. Strong confinement of light in turn allows for large scale integration of optical components. Finally, the SOI system is compatible with already existing semiconductor manufacturing technology made for silicon, which makes mass production viable.

There are however a few drawbacks by using SOI for integrated optics. The high refractive index contrast makes the fabricated structures sensitive to fabrication variations. A thickness change in the orders of nanometers can shift the resonance wavelength of SOI strip ring resonators in the order of nanometers [34]. Additionally, crystalline SOI is fairly expensive due to a complicated fabrication process, making prototyping with this material unfeasible. Alternatively, one can use amorphous silicon (a-Si), which has a higher loss but is easier to fabricate with for instance chemical vapor deposition (CVD).

3.3.2 Plasma Enhanced Chemical Vapor Deposition

Chemical vapor deposition is the process of depositing a thin film on a substrate by using gaseous reactants [35]. The different precursors are pumped into the reactor where a substrate is placed, energy is supplied, and a chemical reaction between the different precursors can occur. An intermediate film precursor is formed and diffuses to the substrate surface. Adsorption occurs at the surface, and a thin film is made by surface reactions of the film precursor. The by-products of the different chemical reactions are then removed from the reactor by vacuum pumps.

The type of CVD used in this project is the plasma-enhanced chemical vapor deposition (PECVD), where a plasma is used to sustain the chemical reaction in the vacuum chamber [35]. A schematic of a typical reaction chamber in a PECVD is shown in Figure 3.2. The substrate holder is grounded, while the top electrode is connected to a radio frequency (RF) power source. A plasma will then be created when the gaseous precursor is pumped into the reaction chamber. The temperature needed in a PECVD is considerably lower than for non-plasma CVD processes due to the supply of energy from the plasma. Less cleaning of the chamber is therefore needed for PECVD resulting in less downtime [35].

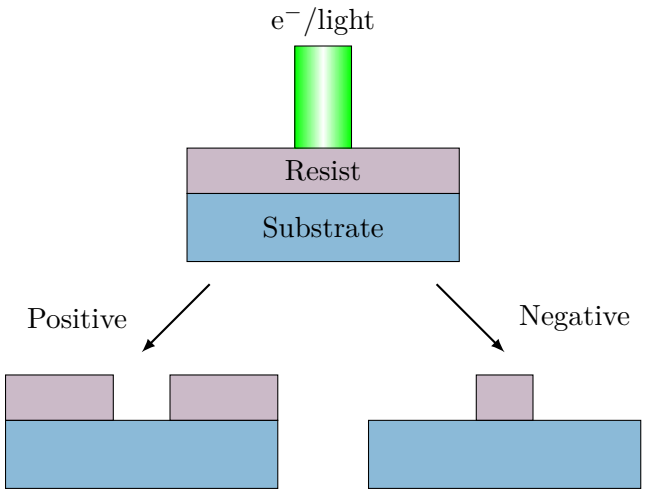

Figure 3.3: Resist is exposed by light or an electron beam and developed. The exposed area will be removed when developing a positive resist, while the unexposed area will be removed when developing a negative resist.

a-Si thin films can be made by using PECVD with silane gas (SiH_4) as the precursor. The net reaction equation is

$$SiH_4(g) \longrightarrow Si(s) + H_2(g). \tag{3.2}$$

The plasma-assisted chemical reactions occurring above and at the substrate surface are very complex, and the properties of the deposited thin film depend on many variables such as RF power and frequency, gas composition, chamber pressure, substrate temperature and electrode separation [35]. The optical properties of the deposited a-Si strongly depend on the quality of the film. Low uniformity and high surface roughness will be detrimental to the overall performance of photonic components due to scattering losses and variation in the refractive index.

3.3.3 Lithograhpy

Lithography generally refers to methods for transferring a pattern onto a planar surface. This technique has been a keystone in semiconductor manufacturing technology since its start, and the transferring of submicron features from a mask onto a silicon wafer is referred to as microlithography or photolithography due to the use of light in the process [35]. The term lithography will be used here, since both electron-beam lithography (EBL) and photolithography will be used in this project. A substrate covered by a light or electron sensitive resist film is exposed by light or electrons in areas specified in a mask. EBL and maskless photolithography uses direct writing where an e-beam or a laser is scanned across the resist at positions specified in a digital mask. Direct writing is slower than photolithography using a mask aligner with a physical mask, where the entire sample is exposed at the same time. This is especially the case for electron beam lithography where the resolution is determined by the current of the electron beam. To increase the resolution, the spot size, and therefore the current, has to be reduced, which will result in increased exposure time.

Depending on resist chemistry, the exposed areas are either made less or more soluble. These resists are called negative and positive resists, respectively. The exposed sample is placed in a resist-specific chemical called developer, and the exposed or unexposed areas are removed (see Fig. 3.3). The pattern from the mask will then be transferred to the resist for a positive resist, while a negative of the pattern will be transferred to the resist for a negative resist.

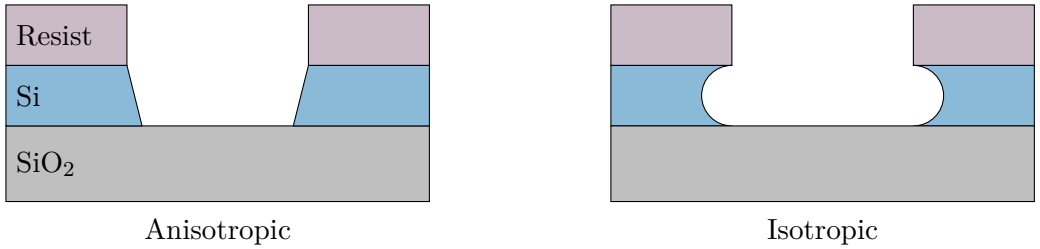

Figure 3.4: Sidewall profiles for anisotropic and isotropic etching.

3.3.4 Etching

Lithography is often followed by an etching step. By using the patterned resist as an etching mask, the pattern can be transferred onto the sample by removing material from the regions not covered by resist (see Fig. 3.4). The different etching techniques can generally be separated into two categories: dry- and wet etching depending on the phase of the etchant used. Dry etch exposes the sample to a gaseous plasma, while liquid chemicals are used in wet etch. For fabrication of photonic crystals and other optical components, there are several important etch parameters, especially the etch profile and the selectivity.

Etch Profile

The etch profile refers to the shape of the sidewalls of an etched feature. The two main etch profiles are shown in 3.4. An isotropic sidewall profile is created when the etch rate is equal in all directions. Isotropic sidewalls are usually made when using a wet etch. The entire sidewall is exposed to the etchant, and since the etching is done by a chemical reaction between the etchant and the sidewall, the profile will be isotropic. An anisotropic sidewall is made when the etch rate is much larger perpendicular to the substrate than in the other directions. Anisotropic sidewalls are mainly achieved using dry etch systems, where ions in a plasma are directed towards the sample surface with an electric field. The directionality of the ions causes the etching to take place only parallel to the sample surface. Additionally, a polymer made by etching the resist with a specific etchant can be deposited at the sidewalls resulting in a decreased etch rate perpendicular to the sidewalls [35]. The roughness of the sidewalls can then be decreased. It is desirable to have steep sidewalls both for strip waveguides and photonic crystals since breaking of symmetry can cause coupling of TE and TM-modes [15].

Selectivity

The selectivity of an etchant is the etch rate of the material being etched relative to the etch rate of another material exposed in the etching process. High selectivity is usually important when etching. If the selectivity in a system is low, the resist mask is etched almost as fast the masked material. Wet etch is usually selective as the chemical reactions responsible for the etching are material selective. Dry etching, on the other hand, is not necessarily very selective. One of the mechanisms responsible for the anisotropic sidewall profile is sputtering by accelerated ions, which will not depend on the material being etched. Selectivity is not necessarily problematic when fabricating optical components using SOI. The resist can easily be made sufficiently thick compared to the 220 nm thick silicon thin film reducing the need for high selectivity etching. However, when making an air-bridge structure using SOI, the SiO_2 beneath the silicon thin film is etched away, leaving a free-standing silicon membrane. The underetching of the SiO_2 has to be very specific in order to remove a sufficient thickness of the oxide layer without etching the silicon thin film.

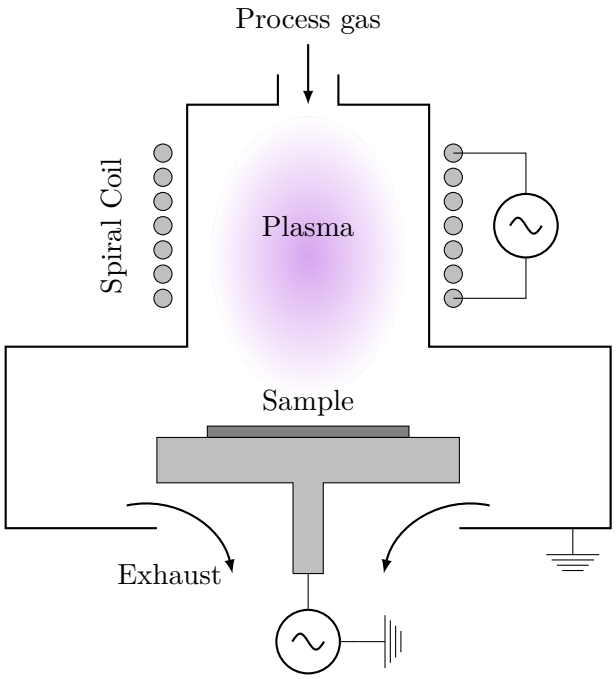

Figure 3.5: Schematic of a ICP-RIE reaction chamber.

Inductively-Coupled Plasma Reactivate Ion Etching

Reactive-ion etching (RIE) is a technique where the selectivity of a chemical etch, and the anisotropy of a physical etch is combined. A plasma of reactive ions is created between a grounded and an RF-powered electrode where the sample is placed. The sample holder will develop a negative voltage due to the deposition of electrons by the RF-field. The voltage difference between the sample and the plasma accelerates the positive ions in the plasma towards the sample surface. Directionality and anisotropic etching are achieved due to the DC self-bias of the sample holder, while the positive plasma ions react selectively with the sample giving the etch selectivity [35]. The pressure is relatively low for standard RIE techniques giving a low etch rate. This is especially troublesome for etching smaller geometries, such as photonic crystal holes, where loading effects decrease the etch rate significantly compared to larger areas [35]. The main reason for the slow rate is the low pressure needed to create a plasma by using parallel electrodes resulting in a low-density plasma [35]. Inductively-coupled plasma reactive-ion etching (ICP-RIE) is a technique where the plasma density is increased compared to standard RIE without increasing the pressure of the chamber. An inductive coil is placed above the reaction chamber, creating a high density plasma, while an RF-field is set up between two electrodes as for standard RIE (see Fig. 3.5). The inductive coil is responsible for creating a high density plasma, while the electrodes are responsible for directing the ions towards the sample surface. The ion energy and current are decoupled, and the etch rate can be increased without increasing the energy of the ions, which could have resulted in sputtering.

3.3.5 Scanning Electron Microscopy

The main characterization tool used in this project is the scanning electron microscope (SEM). Electrons are accelerated, focused, and scanned over the sample by electromagnetic coils (see Fig. 3.6). When the focused electron beam strikes the sample, secondary and backscattered electrons are emitted as well as characteristic and continuous X-rays [35]. The electrons are detected and counted, and an image is made by raster scanning the beam over the sample and mapping the number of electrons to pixel intensity. The contrast mechanism in the image

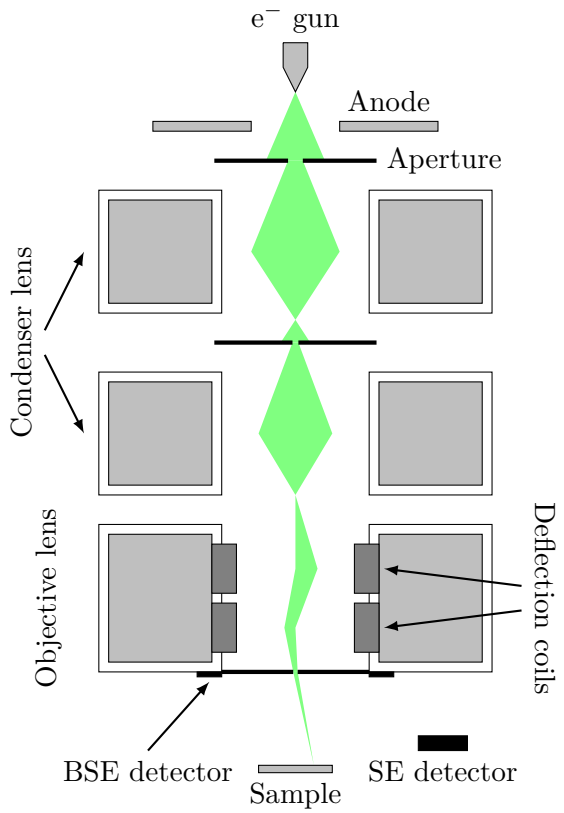

Figure 3.6: Schematic of a scanning electron micropscope.

depends on the electrons detected. Only secondary electrons generated near the surface are able to leave the sample due to their low energy. The number of secondary electrons emitted from the sample surface and detected, and therefore the contrast in the image, will strongly depend on the topography of the surface. On the other hand, the number of emitted backscattered electrons increases with increasing atomic number. Backscattered electron images therefore have compositional contrast. Additionally, the backscattered electrons escape from deeper in the sample, making the contrast less dependent on topography than for secondary electron images [36]. The energy of the different types of electrons also has implications for the placement of the detectors. Secondary electrons are usually detected using an Everhart-Thornley detector placed next to the sample stage, while backscattered electrons with their high energy are measured by a detector placed around the electron beam aperture (see Fig. 3.6).

Chapter 4

Experimental Procedure

The experimental procedure used for simulating, fabricating, and characterizing photonic crystal devices in this project is presented in this chapter. The different simulations performed are described and motivated, and figures explaining the different simulation geometries are shown. The fabrication and characterization processes are listed with sufficient detail to be reproducible.

4.1 Simulation

The photonic crystal drop filter consists of three components: input and output waveguides and a resonance cavity. The waveguides were analyzed and optimized using MPB and Meep, while the resonance cavity was optimized using Meep with Harminv. The coupling between the different components was investigated using COMSOL and Meep.

Simulation Parameters

Many of the different photonic crystal components investigated have common simulation parameters. All components are based on a triangular silicon photonic crystal with a lattice constant a, which is used as a length scale. For 3D simulations the height, h, is chosen to be 0.55, corresponding to a 220 nm thin film if the lattice constant is 400 nm. The resolution was set to between $a/15$ and $a/20$ for 3D simulations and between $a/16$ and $a/20$ for 2D simulations.

The refractive indices used for the different materials are listed in Table 4.1 and should be valid at a wavelength of 1550 nm [37–39]. The refractive index of the biolayer is chosen to be the same as used by Lee and Fauchet [10], which is close to the refractive index measured for a thin film of APTES [40]. The refractive index for 2D SOI is based on the effective refractive index calculation shown in Appendix A.

Table 4.1: Refractive indices used in simulations.

Material	Refractive index
Air	1
Silicon	3.48
SiO_2	1.44
Water	1.32
Biolayer	1.45
2D SOI	2.88

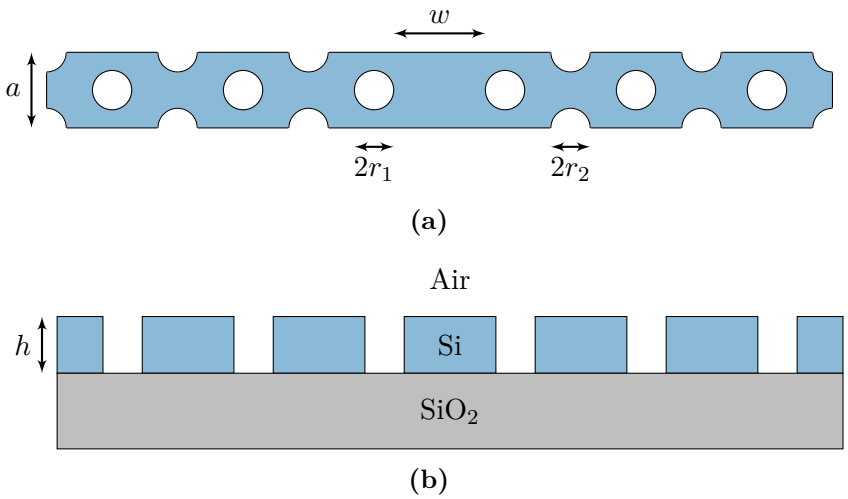

Figure 4.1: Supercell used for calculating the dispersion relation and group index for waveguides. r_1, r_2 and w shown in (a) are varied in the different simulations.

4.1.1 Photonic Crystal Band Structure

The dispersion relations for light in bulk photonic crystals and linear defect waveguides are important to investigate when designing a photonic crystal drop filter. The bulk photonic crystal will determine which resonance frequencies can be excited in a photonic crystal resonator and the band of frequencies guided by a linear defect waveguide. Furthermore, tuning the waveguide may be needed for optimizing coupling between the waveguide and resonator as well as for improving the transmission of the waveguide.

Gap Size

The band structures for the 2D triangular photonic crystal were calculated for radii between 0 and $0.5a$ using MPB. The band gap size for each radius was calculated only considering wave vectors at M and X since the band minima and maxima are found for these vectors. Only TE-modes were considered since the band gap for TE-modes is much larger than for the band gap for TM-modes in a 2D triangular photonic crystal of air holes in silicon [15].

Waveguide Tuning

Next, the dispersion relation and the group velocity for a linear defect waveguide were investigated. The frequency supported by the designed resonance cavity has to be guided by the waveguide for the filter to work properly. Furthermore, intrinsic loss mechanisms and the reflection loss scale as $1/|v_g|$ [41, 42], where v_g is the group velocity of the light guided in the waveguide. It is therefore important to make sure the frequency of interest has a sufficiently high group velocity in the waveguide. The dispersion relation, and thus the group velocity, for light in photonic crystal waveguides with different radii were calculated. The effect of changing r_1 and r_2 shown in Figure 4.1 was then investigated, as this is suggested by Frandsen et al. as a method for tuning the dispersion relation for linear defect waveguides [43]. Additionally, increasing the width of the waveguide has been used to redshift the band of guided frequencies [44]. Therefore, the dispersion relations for waveguides with increased width were also calculated. The dispersion relations for all waveguides were calculated using the supercell approximation as illustrated in Figure 4.1, and projecting the **k**-vector along the linear defect [24]. The transmission of PhC waveguides in 3D SOI and 3D air-bridge structures were simulated in Meep to compare the performance of these structures.

Band Edge Frequency

Fabricated devices can deviate slightly from the designed and simulated devices. The refractive index of the silicon thin film as well as the buried oxide, can be different than what was used in simulations. Additionally, the lattice constant, hole radius, and thin film thickness measured for fabricated devices deviated from the intended sizes. The shift in band gap, and therefore band edge frequency, due to fabrication imperfections was estimated by calculating the band edge frequency for a variation of slab thickness, waveguide width, and hole radii. The calculations were done in MPB exploiting that the band edge frequency occurs for $\mathbf{k}$ at the Brillouin zone boundary to reduce the number of calculations.

4.1.2 Drop Filter

The three main components of the photonic crystal drop filter, the resonance cavity and the input and output waveguides, were investigated and optimized using Meep. As pointed out in Section 2.3.1, both the quality factor and the signal-to-noise ratio of the filter will determine the performance of the biosensor made using a PhC drop filter. The quality factor of the resonator will set an upper limit for the quality factor of the filter, while the coupling between waveguide and resonator will determine the transmitted power at the resonance frequency, and thus determine the signal-to-noise ratio.

Quality Factor Optimization

The resonance cavity investigated in this project is the linear cavity made by removing air holes from a bulk photonic crystal (Sec. 2.2.4). In the project work prior to this project, the heterostructure cavity [44–46] was found to give higher quality factors than cavities where smaller air holes were placed inside the cavity [47] or air holes surrounding the cavity were displaced [25, 48, 49]. The effect on the resonance frequency and quality factor when increasing the cavity width and the heterostructure width was simulated using Meep and Harminv. The effect of increased cavity width was investigated by comparing a cavity with 19 removed holes and a cavity where an entire row of holes was removed (Fig. 4.2a and Fig. 4.2b). The heterostructure width (as shown in Figure 4.2a) was changed from $3a_3+3a_2$ to $7a_3+3a_2$ and the quality factors and mode profiles were calculated using Meep. A Gaussian pulse was placed in the middle of the resonator to excite the resonance modes which were analyzed using Harminv.

Waveguide-Resonator Coupling

With the quality factor of the unloaded resonator fixed, the transmission in the drop filter will be determined solely by the decay rate between waveguide and resonator. The waveguide-resonator distance dependence on the decay rate was found by calculating the total quality factor for a heterostructure cavity with parallel waveguides placed above and below the resonator. The distance between the resonator and the waveguides was varied between two and six rows. The calculations were done in 2D and 3D for both an air-bridge and an SOI photonic crystal. The results were then validated for a 3D SOI drop filter using Meep. The effect of placing mirrors in the input and output waveguides was then investigated using COMSOL since this allows for outputting the steady state electric field norm at a given frequency which can provide useful insight. A PhC drop filter designed in the project work prior to the master's project was used, and mirrors were made by terminating the waveguides in the photonic crystal, as shown in Figure 4.3. The transmission was calculated for mirrors placed 11 and 12 rows away from the middle of the cavity. The findings were confirmed for a 3D drop filter by calculating the dropped transmission using Meep. Additionally, a filter with a tilted output waveguide (see Fig. 4.4) was tested, since the cavity will overlap more with the output waveguide in this configuration, giving an increased decay rate, compared to the filters where resonator and waveguides are parallel

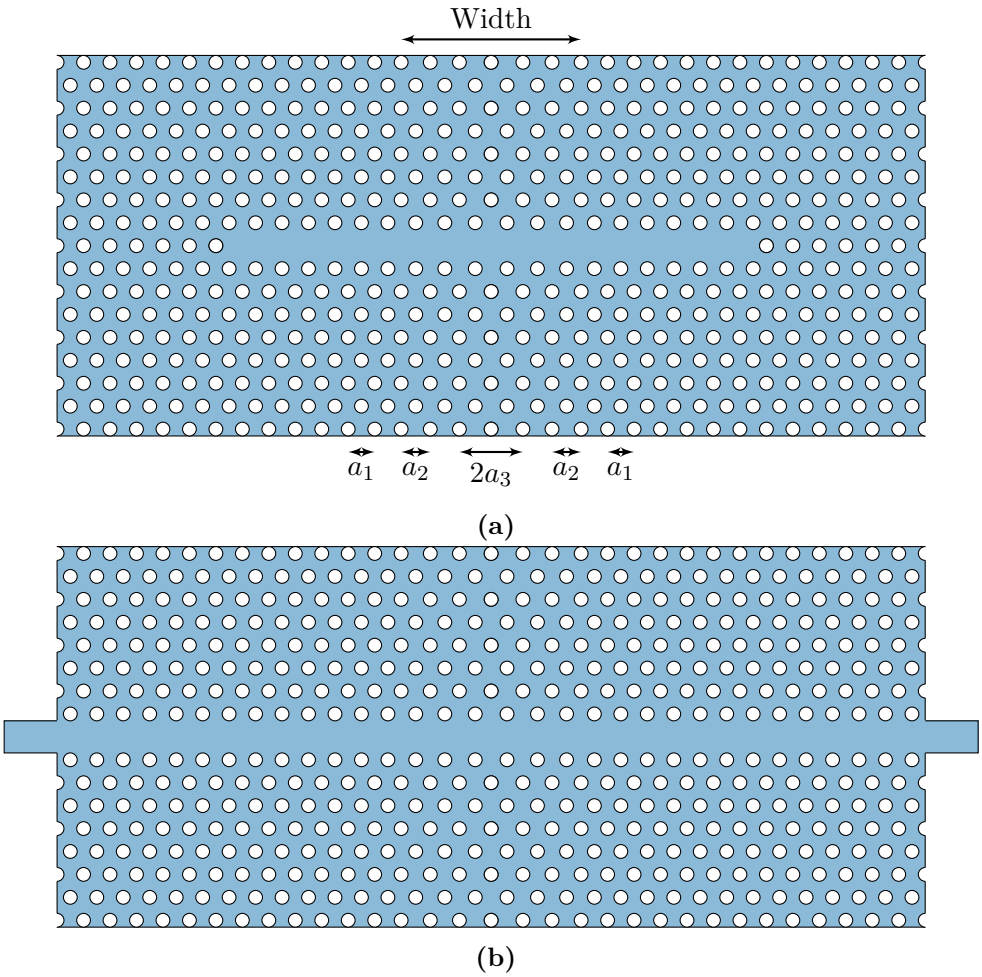

Figure 4.2: Heterostructure cavities where (a) 19 holes are removed and (b) an entire row is removed. The width of the heterostructure is indicated in (a), where this is set to $3a_3 + 3a_2$. Widening of the heterostructure is done by increasing the middle section from $2a_3$ to $6a_3$.

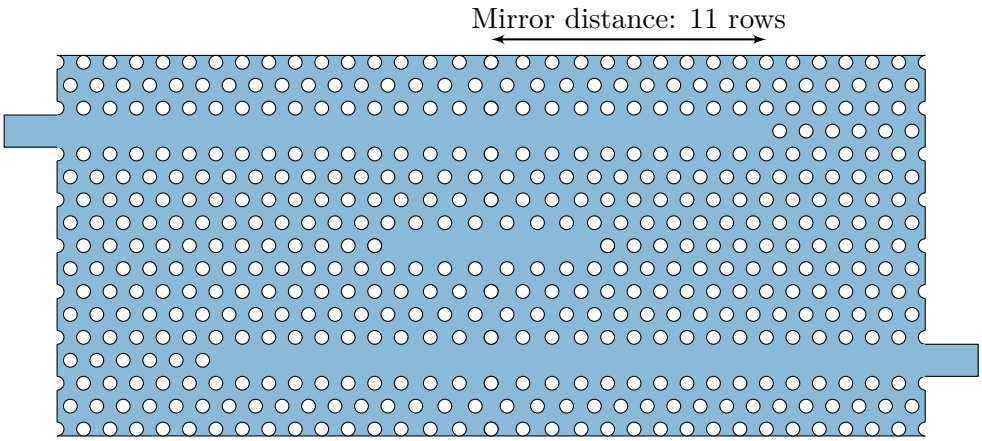

Figure 4.3: Drop filter with heterostructure cavity and waveguide mirrors placed 11 rows away from the center of the cavity.

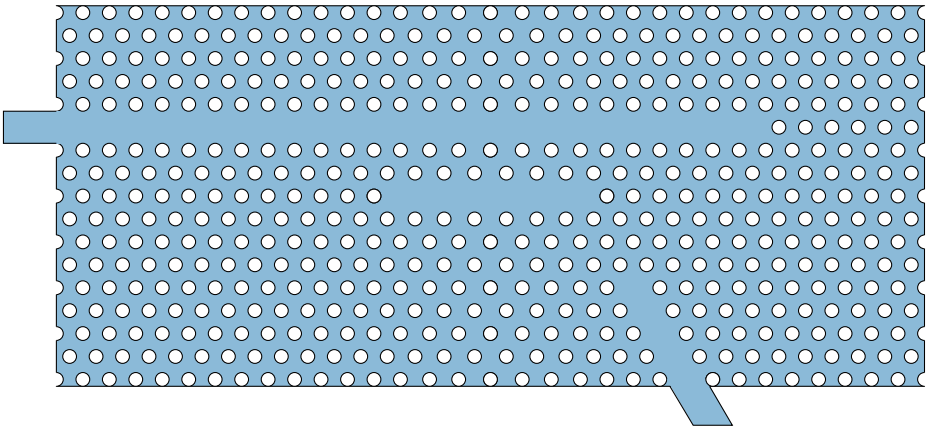

Figure 4.4: Drop filter with heterostructure cavity where the output waveguide is tilted 60°.

[50]. Hole radius taper [51, 52] discussed in the project work prior to the master's project and a 7-10% widened photonic crystal waveguide was used for all photonic crystal filters.

4.1.3 Multiplexing

Placing photonic crystal filters with different lattice constants next to each other to create a multiplexed device [53, 54] was studied in the specialization project. The resonance frequency of a drop filter scales linearly with the lattice constant as discussed in Section 2.1.2. One can therefore create a multiplexed device with several tunable resonance peaks by placing drop filters without mirrors with different lattice in series. The simulation was repeated here, but the number of filters was increased from two to four, the widths of the cavities were reduced, and the output waveguides were widened by reducing the radii next to the waveguide instead of removing two rows of air holes as done earlier.

4.1.4 Biosensing

An optimized SOI photonic crystal drop filter was used to simulate refractive index sensing of antigens by placing a 20 nm thick layer with a refractive index of 1.45 above the silicon thin film (see Fig. 4.5). Additionally, the redshift due to the added biolayer for the resonance cavity studied earlier was calculated to compare SOI and air-bridge structures.

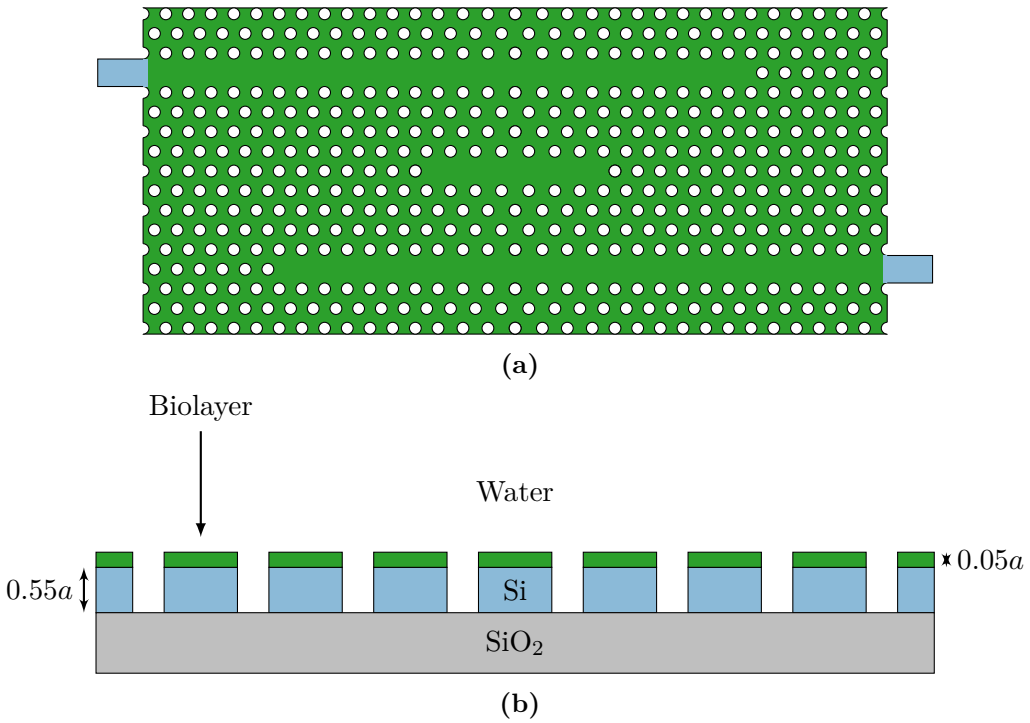

Figure 4.5: Overview and cross-section of mirrored drop filter with a $0.05a$ biolayer placed on the silicon thin film.

4.2 Fabrication

The different fabrication steps are presented in the same order as the fabrication process flow. Figure 4.6 shows the main processing steps for producing the SOI waveguides and photonic crystals. A 4-inch crystalline silicon (c-Si) wafer with a 2 µm thermally grown SiO_2 top layer was used as a starting point. The wafer was scribed and cleaved manually into 15x15 mm^2 chips before further processing.

4.2.1 Silicon Deposition

The PECVD system used for depositing a-Si in this project is an Oxford Instruments PlasmaLab System 100. The process parameters used for deposition are summarized in Table 4.2, and the following process steps were used:

Cleaning: Ultrasonic bath in acetone for 5 min was done to remove dust from scribing and breaking. The ultrasonic bath was followed by rinsing in isopropanol (IPA) and drying with N_2.

Preconditioning: In order to stabilize growth conditions, a preconditioning step was performed on a dummy silicon wafer by depositing a-Si for 3 min using the same parameters as for the thin film deposition (Tab. 4.2).

Deposition: 220 nm a-Si was deposited on a SOI sample for 170s using the parameters in Table 4.2.

4.2.2 Electron Beam Lithography

The SOI samples were patterned for etching by using the Elionix ELS-G100 100 kV electron beam lithography system. Standard lithography steps developed by previous masters's students [1–3] were altered slightly and are summarized below.

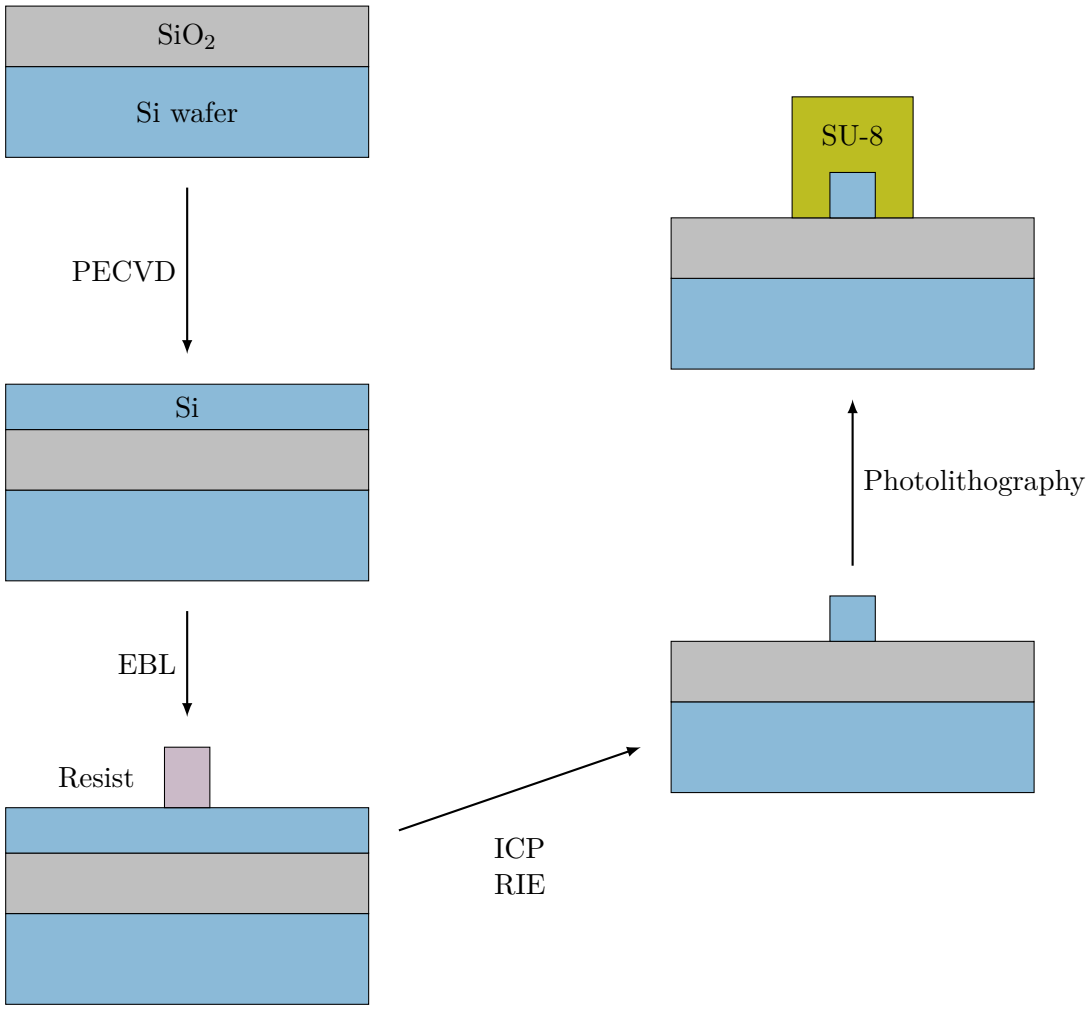

Figure 4.6: Overiew of the main processing steps used for fabricating a photonic crystal with inverted taper waveguide covered by a polymer waveguide using SOI.

Table 4.2: Process parameters for deposition of a-Si.

Parameter	Setting
SiH_4	50 sccm
Ar	150 sccm
Pressure	500 mTorr
LF power	200 W
Temperature	300 °C

Cleaning: Ultrasonic bath in acetone for 5 min followed by rinsing in IPA and drying with N_2 to remove handling dust.

Spin Coating: Spin coating was done directly after cleaning. A CSAR 6200.13 resist film was spun onto the SOI samples at 4000 RPM for 60s with an acceleration of 500 RPM/S for 7s. This gave a film thickness of approximately 490 nm measured with reflectometry.

Soft bake: 150 °C on a hotplate for 1 min.

Exposure: Exposure was done with a beam current of 1 nA and an exposure dose of 350 µC/cm^2. The pattern was divided into write fields of 500x500 µm^2. Exposure with 1 pA/1 nA was also tested.

Development: Exposed samples were immersed in an AR 600-546 developer for 1 min. The development was stopped by dipping the sample in IPA followed by rinsing in another beaker with IPA.

Removal: The patterned resist was removed after etching in an ultrasonic bath of AR 600-71 for 5 min. Rinsing was done using IPA, and the sample was dried with N_2 afterward.

4.2.3 Etching

Etching was done directly after plasma cleaning using a PlasmaLab System 100 ICP-RIE 180 from Oxford Instruments following the flow presented below:

Plasma cleaning: After development, the sample was plasma cleaned with a Diener Electronic Femto plasma cleaner to remove small pieces of resist left on developed regions. An O_2 gas flow of 100 sccm and a generator frequency of 20 kHz was used for 1 min.

Preconditioning: A dummy silicon sample was etched for 3 min using the process parameters presented in Table 4.3 to stabilize etching conditions.

Etching: The SOI sample with patterned resist was placed on a silicon carrier wafer and etched using the same parameters as above (Tab. 4.3) for 1 min.

Table 4.3: Process parameters for silicon etching using ICP-RIE.

Parameter	Setting
SF_6	7.5 sccm
CHF_3	50 sccm
CCP power	40 W
ICP power	600 W
Temperature	20 °C
Etch time	45 s

4.2.4 Photolithography

After etching and removal were done, polymer waveguides [55] were made using a Heidelberg Maskless Aligner MLA150. The following process steps were used:

Cleaning: The sample was cleaned by an ultrasonic bath for 5 min in acetone if this step did not follow directly after stripping of EBL-resist. Rinsing with IPA and drying with N_2 were done after the ultrasonic bath.

Priming: Plasma cleaning with 100 sccm O_2 and generator frequency of 20 kHz was done for 1 min before priming the sample with hexamethyldisilazane (HMDS).

Spin Coating: SU-8 2003.5 was spun onto the samples at 5000 RPM for 30s giving approximately a 2 µm thick thin film.

Soft Bake: Baking at 95 °C on a hotplate for 3 min was done to remove solvent in the resist.

Exposure: Exposure was done with a dose of 3050 mJ/cm^2 using a 375 nm laser.

Post Exposure Bake: Baking at 95 °C on a hotplate for 3 min was done to catalyze polymer reactions in the resist [35].

Development: The exposed samples were developed by stirring calmly in mr-Dev 600 for 1 min, followed by a development stop in IPA.

Hard Bake: 150 °C on a hotplate for 5 min to harden the resist.

4.2.5 Sample Cleaving

A Dynatex DX-III scriber and breaker tool was used to break the samples into suitable pieces for SEM analysis and optical characterization. The samples were scribed and cleaved along the {100}-planes of the silicon crystal using an "edge-scribe mode" to avoid scribing of optical components such as strip waveguides.

4.3 Characterization

4.3.1 Scanning Electron Microscopy

The fabricated samples were investigated using a FEI Apreo SEM. The main purpose of the SEM analysis was to measure the sizes of patterned features to compare with the designed mask and to inspect the quality of the fabricated devices. An acceleration voltage of 10 kV and a current of 0.2 nA were used when taking images of the surface, while an acceleration voltage of 30 kV was used when taking cross-section images to avoid charging. Image analysis was done by using the Canny algorithm for edge detection [56] and circle Hough transform for circle detection [57] in Matlab. Features in processed images were measured using ImageJ [58].

4.3.2 Optical Characterization

The optical setup used for characterization is illustrated in Figure 4.7 and the different components are listed in Table 4.4. The samples were placed on the XYZ stage and aligned with the input and output fiber by using a microscope. The IR camera was then used to choose the height of the input fiber that maximized coupling of light into the chip. The height of the output fiber was then adjusted to maximize the current measured by the photodetector. After the alignment of fibers, the laser was tuned in the region 1620 nm to 1480 nm and transmission spectra were recorded.

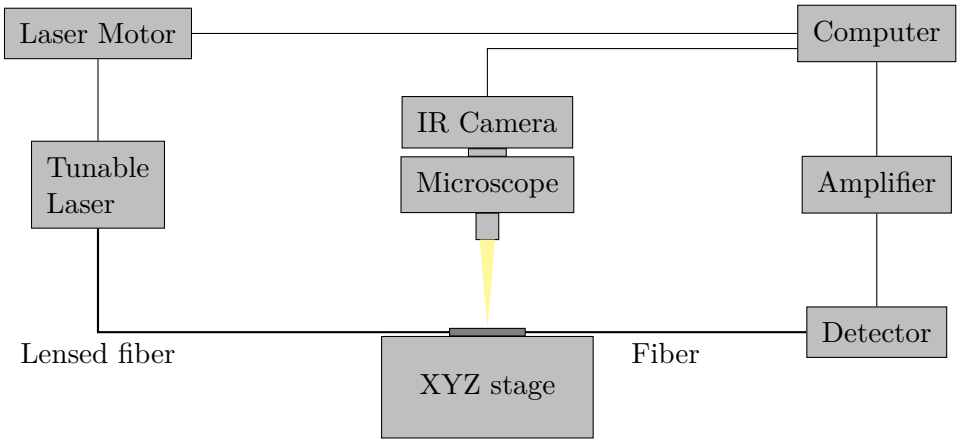

Figure 4.7: Optical setup for transmission measurements on fabricated samples.

Table 4.4: Model and manufacturer of the components used in the optical setup

Component	Manufacturer and model
Laser diode driver	Newport 505
Temperature controller	Newport 325
Laser motor	Thorlabs TDC001
Laser	Thorlabs TLK-L1550M
Fiber Polarizer	Thorlabs
Lensed Fiber	Nanonics Imaging
XYZ stage	Elliot Scientific MDE881
Microscope	Leitz Wetzlar
Objectives	Olympus LMPlan 10x IR, SLMPlan 20x
IR Camera	Hamamatsu C14041
Photodetector	InGaAs PIN diode
Amplifier	Thorlabs PDA200C

Chapter 5

Results and Discussion

In this chapter, the results from simulations, fabrication, and optical measurements are presented and discussed separately. The simulations results are presented first since the parameters used when fabricating photonic devices are based on the simulation results. Later, the results from the characterization of the fabricated sample are discussed, and the performance of the fabricated devices is compared to the simulation results.

5.1 Simulations

3D simulations of SOI and air-bridge structures, as well as simulations of the corresponding 2D structures using the effective index approximation, were performed. 2D simulations are mainly used for investigating trends in waveguide tuning, while 3D simulations are used when simulating resonance cavities, drop filters, and waveguides. The validity of the 2D simulations of these types of structures is also discussed.

The starting point for the simulations is the band structures for the photonic crystal and the linear defect waveguide. The photonic band gap and the dispersion relation for the PhC waveguide determine the operating frequency range of the photonic crystal drop filter. Straight PhC waveguides are then simulated with 2D and 3D FDTD to confirm the findings in the band structure simulations. Next, the heterostructure cavities are optimized by using 3D FDTD and coupling between waveguide and cavity is investigated. With all the components of the drop filter optimized, full 3D simulations of the drop filter are performed, and the effect of adding a biolayer on top of the structure is investigated. Additionally, a multiplexer with four tunable resonance peaks is simulated using 2D FDTD.

5.1.1 Photonic Crystal Band Gap

The band gap size (defined in Sec. 2.1.2) for TE-modes in a 2D photonic crystal where the hole radius is varied between 0 and $0.5a$ is shown in Figure 5.1. The effective index approximation is used for the silicon slab. The maximum gap size of 40.5% for this system is found for $r = 0.414a$. A gap size of 10% is found for a hole radius between $0.23a$ and $0.49a$. The gap size of the photonic crystal effectively determines the frequency range where light can be guided in the photonic crystal by a linear defect waveguide as shown in Figure 5.2a and Figure 5.2b for an SOI photonic crystal. The tunable laser used for optical measurements in this project has a wavelength tunable in the range 1480 nm to 1620 nm. A PBG size of 9% is therefore needed to cover the whole wavelength range. Since the guided modes in a linear defect waveguide typically do not cover the whole gap size as seen in Figure 5.2a and Figure 5.2b, a larger PBG than the wanted transmission bandwidth is needed. However, it is not really necessary to cover the whole range of tunable wavelengths. For a single photonic crystal drop filter with a quality factor of 1000 and a resonance wavelength of 1550 nm, the resonance width will be 1.55 nm. A PBG size

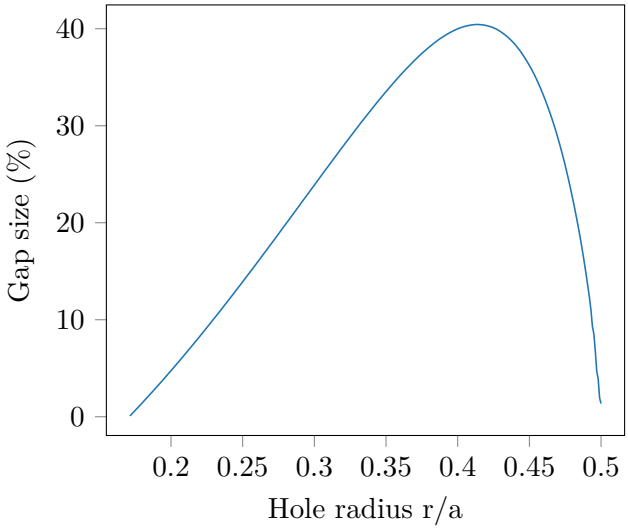

Figure 5.1: Gap size as a function of r/a for 2D photonic crystals of air holes in silicon where the effective refractive index approximation is used for the refractive index of the silicon.

of ∼1% is then needed to surround the resonance peak by a few nanometers of PBG to separate the peak from noise. The gap size needed for a multiplexer where several drop filters are put in series is larger, but since the resonance shift due to binding of the proteins used in our group typically is smaller than 1 nm [59], the gap size needed to separate the different peaks without overlap during biosensing is still much smaller than the tunable range of the laser. The gap size needed will of course also depend on the position of the resonance frequency compared to the band edge of the linear defect waveguide. A gap size of 10% is used as a lower bound for the photonic crystal devices studied here, corresponding to a band gap of 150 nm as this should give a sufficiently large operating wavelength range.

5.1.2 Waveguide Tuning

The linear defect photonic crystal waveguide is one of the main components of the photonic crystal drop filter and determines the frequency range that can be guided in and out of the photonic crystal drop filter. As can be seen in Figure 5.2b only a few of the lowest-lying guided modes are below the SiO_2 light line. Modes with a frequency above the light line will radiate to the cladding, and will therefore be lossy. This can be detrimental for the transmission of the mode in a waveguide [60]. It can also be seen from Figure 5.2b that the group velocity of the lowest-lying modes goes to zero for wave vectors approaching the BZ boundary. This is due to coupling of forward and backward propagating waves forming a standing wave at this wave vector [61]. Light with a frequency equal to or smaller than the frequency of this mode is not guided by the waveguide, and the frequency of the standing wave is therefore called the band edge [61].

The calculated dispersion relation and group index for the lowest-lying TE-like modes for a 2D photonic crystal with r/a between 0.2 and 0.38 using the effective index approximation are shown in Figure 5.3. The 2D dispersion relations closely resemble the dispersion relation of the lowest-lying modes for the SOI waveguide. It is clear that reducing the hole radius redshifts the band edge frequency. The perturbation theory for shifting material boundaries is generally much more complicated than for a small change in the dielectric function [20]. However, the hole radius dependence on the band edge frequency is sufficiently explained by the variational principle (Eq. 2.16). The mode is more confined to the silicon for a small hole radius than for a large radius since the waveguide essentially has become wider. Thus, one can expect a lower frequency for a small hole radius than for a large hole radius according to the variational principle. Figure 5.3b

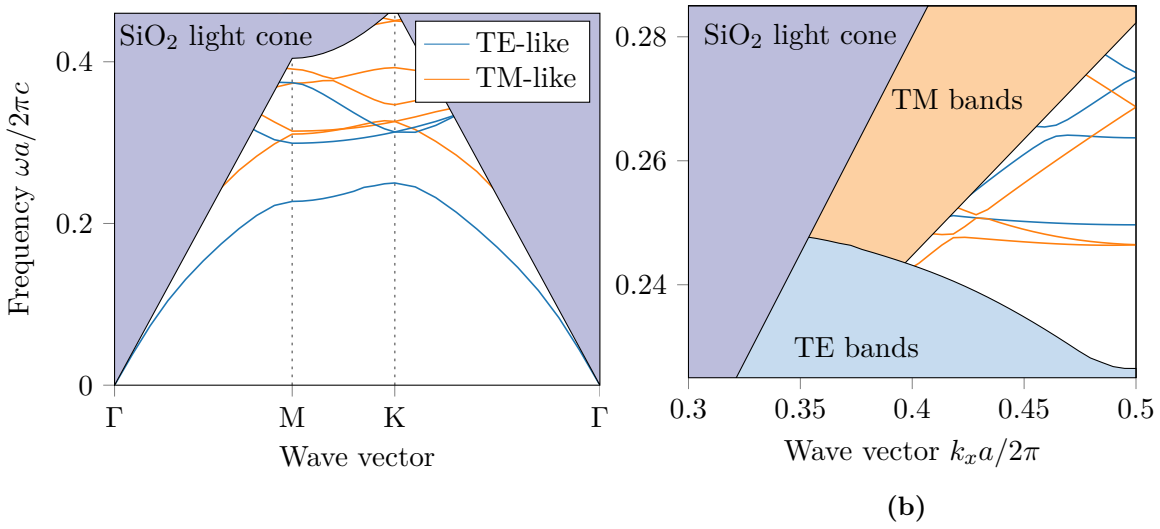

Figure 5.2: (a) Band diagram for an SOI photonic crystal of air holes in silicon. An incomplete band gap for TE-modes is found for frequencies between 0.25 and 0.3. (b) Band structure for a linear defect waveguide made by removing 1 row of holes from the structure in (a).

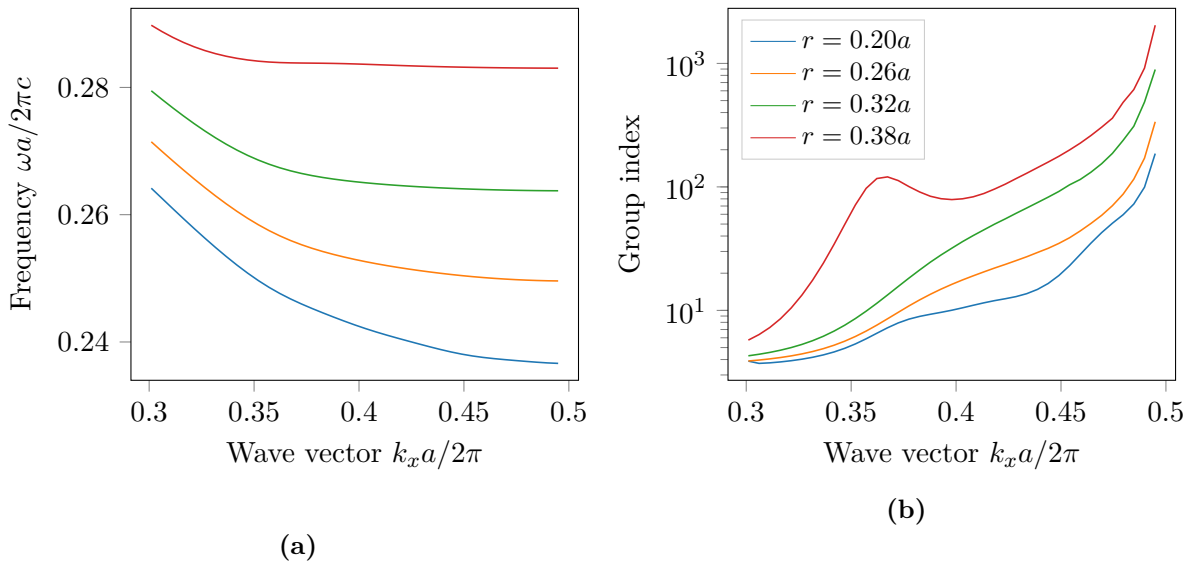

Figure 5.3: Dispersion relation and group index for r/a ratio between 0.2 and 0.38. (a) The band edge frequency decreases with decreasing air hole radius and (b) the group index decreases with decreasing air hole radius.

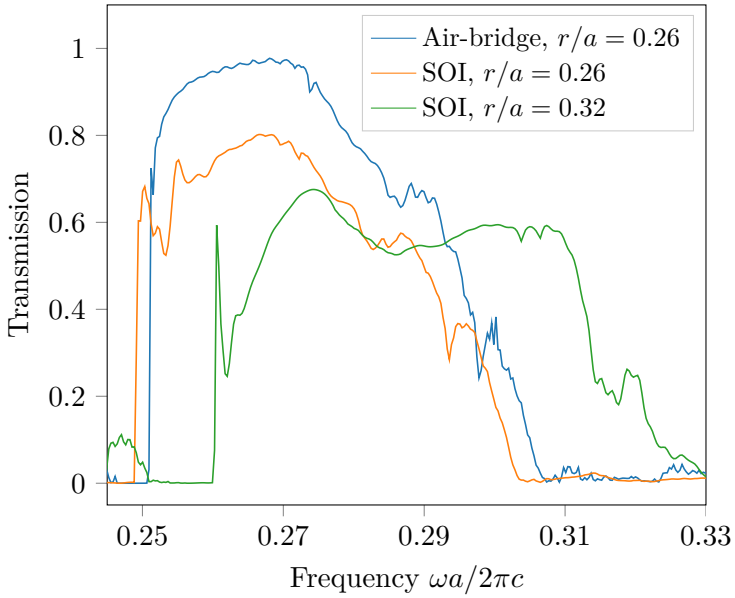

Figure 5.4: Transmission in PhC waveguides using 3D FDTD. The air-bridge waveguide has a larger transmission than the corresponding SOI waveguide. Increasing the hole radius increases the transmission window, and decreases the overall transmission.

also shows that the group index increases with increasing hole radii over the whole frequency range investigated here. Since the group velocity goes to zero at $k_x a/2\pi = 0.5$, the group index will diverge for this wave vector and is therefore omitted from the calculations. Intrinsic loss such as material absorption and extrinsic scattering loss due to fabrication imperfections are proportional to the group index [41, 42]. Kubo et al. report significantly reduced transmission through a standard linear defect waveguide for light with a group index above 30 [62]. A small hole radius giving a sufficiently large band gap is therefore preferable. In Figure 5.4, the transmission through air-bridge and SOI PhC waveguides with $r/a = 0.26$ and $r/a = 0.32$ are shown. For hole radius of $0.26a$, the transmission bandwidth is similar for SOI and air-bridge, but the transmission is larger for the air-bridge PhC waveguide. The SiO_2 light line decreases the transmission since coupling to leaky modes is enhanced. Increasing the hole radius reduces the transmission, especially in the slow light regime, while the width of the transmission band is increased. It is also important to investigate the tunability of the dispersion relation for the lowest-lying modes. The dispersion relations for 2D photonic crystal waveguides where the radius of the first and second row of air holes next to the waveguide are varied are shown in Figure 5.5. The dispersion relations show that decreasing the radius of the first row of holes has a bigger impact on the band edge frequency than decreasing the radius of the second row of holes. On the other hand, from Figure 5.5b, one can see that the group index mainly depends on the radius of the second row of air holes. Changing the hole radius of these two rows is therefore a simple method for tuning the dispersion relation of the linear defect waveguide, and can be useful for guiding light with a frequency originally associated with a large group index and therefore low transmission. Similar findings are presented by Frandsen et al. [43]. The electric field of the lowest-lying modes extends over the two rows next to the waveguide, and a change in dispersion characteristics is expected when the hole radii change [43].

For heterostructure cavities that will be discussed later, the resonance frequency is lower than the band edge frequency of the standard linear defect waveguide and a redshift of the band edge frequency is therefore needed to make a drop filter with a heterostructure cavity function properly. As discussed above, reducing the radius of the row of air holes next to the waveguide can be used to tune the band edge frequency. A different method of tuning the

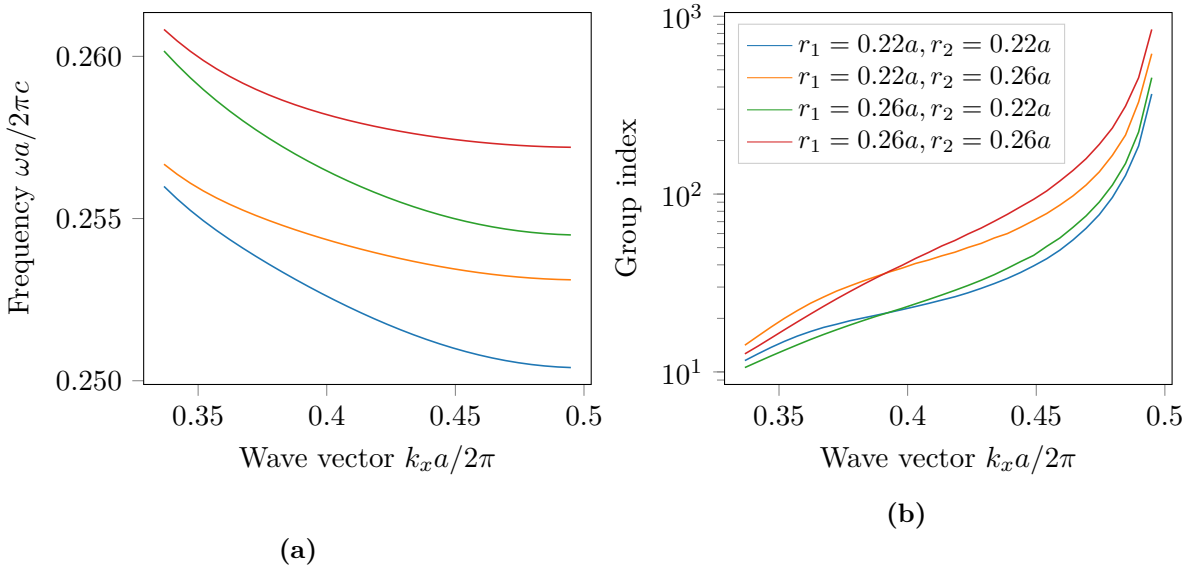

Figure 5.5: Dispersion relation and group index for waveguides where the hole radius in the two rows next to the waveguides are tuned. (a) Changing the hole radius in the first row next to the waveguide mainly affects the band edge frequency, while (b) changing the next row of holes changes both band edge frequency and group index. Both band edge frequency and group index decrease with decreasing air hole radius.

band edge frequency is to displace the photonic crystal above and below the waveguide to make the waveguide wider. The effect on the band edge frequency by widening the waveguide is compared to reducing the first row radius for an SOI photonic crystal waveguide with $r = 0.26a$ in Figure 5.6. The band edge frequency is calculated for a waveguide widened up to 20%, while the hole radii in the row next to the waveguide are decreased from $0.26a$ to $0.14a$ since this corresponds to a 20% increase in waveguide width. The band edge frequency for the two methods strongly correlates suggesting that either method can be used to redshift the band edge frequency. The reduction of hole radius has the advantage of not changing the overall photonic crystal, which makes it easier to add components such as bends in the photonic crystal [1]. However, a reduction in hole radius complicates etching due to the loading effects mentioned in Section 3.3.4. For the devices considered in this project, bent waveguides are not much used and displacing the photonic crystal to increase the waveguide width is therefore used as a method for redshifting the band edge.

5.1.3 Band Edge Frequency

The band edge frequency of the photonic crystal waveguide can be used as a reference point when doing transmission measurements on fabricated devices. No light is transmitted below the frequency, and the transmission increases rapidly above it, making it easy to locate. With the band edge frequency of a photonic crystal known, one can easily pinpoint the region where the resonance frequency of a drop filter made in the same crystal should be found. The lattice constant and the hole radius of a fabricated device is set such that the band edge frequency is in the tunable range of the laser used for optical measurements, preferably towards the long wavelength end of the range. From Figure 5.6 a unitless band edge frequency of 0.2505 is found for a photonic crystal with 10% widened waveguide, hole radius $r = 0.26a$ and a silicon thickness of $0.55a$. Setting the lattice constant to 400 nm should then give a band edge wavelength of approximately 1597 nm. However, since several of these parameters are susceptible to fabrication fluctuations [1–3], it can be useful to find a wider estimate for the band edge frequency by varying the different parameters slightly around the values above. The band edge frequency

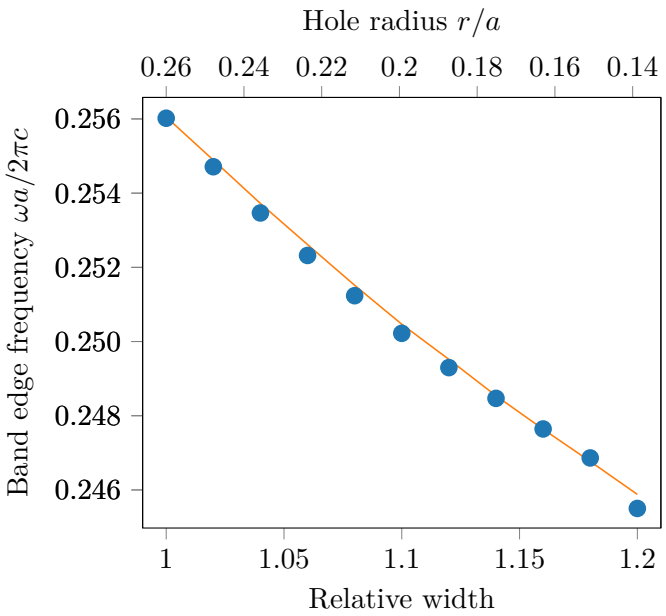

Figure 5.6: Band edge frequency for widened waveguide (blue dots) compared to waveguide where the radius is reduced in the rows next to the waveguide (orange line). The band edge frequency shift is similar for the two methods.

Table 5.1: Quality factors and resonance frequencies for the fundamental mode in a heterostructure cavity for three different material systems.

Material system	Resonance frequency $\omega a/2\pi c$	Quality factor
3D SOI	0.2535	91,500
3D air-bridge	0.2557	1,200,000
2D SOI	0.2454	130,000

where hole radius, waveguide widening, and silicon thickness is varied slightly is shown in Figure 5.7. A linear relationship between the band edge frequency and the parameter varied is found for all parameters. It should be sufficient to fabricate devices with lattice constants between 390 and 410 nm, accounting for variations in waveguide width and hole radius. The band edge frequency also depends on film thickness and refractive index. The refractive index of the silicon should be fairly constant if the PECVD recipe is not altered, while the film thickness is set to 220 nm to satisfy single mode conditions for the SOI strip waveguide [34]. This film thickness corresponds to $0.564a$ and $0.537a$ for the lattice constants above, which does not shift the band edge frequency significantly, as seen in Figure 5.7.

5.1.4 Quality Factor Optimization

Heterostructure cavities [44–46] are used in the photonic crystal drop filters designed in this project. In the project prior to this thesis, a quality factor of $\sim 12,300$ and a unitless resonance frequency of 0.2689 was found for an SOI heterostructure cavity with hole radius $0.32a$. As discussed in Section 5.1.2, a reduced hole radius leads to an overall increase in group velocity, which in turn decreases waveguide loss. The same heterostructure cavity as considered in the project work with reduced hole radius to $0.26a$ was simulated using 3D FDTD, and a resonance frequency of 0.2573 and a quality factor of 22,300 was calculated. The frequency shift is consistent with the band edge frequency shift found when decreasing the hole radius of the photonic crystal discussed above. The increased quality factor can be explained by a shift of the light line $\omega = c|\mathbf{k}|/\sqrt{\varepsilon}$. The width of the light cone is proportional to the frequency, and

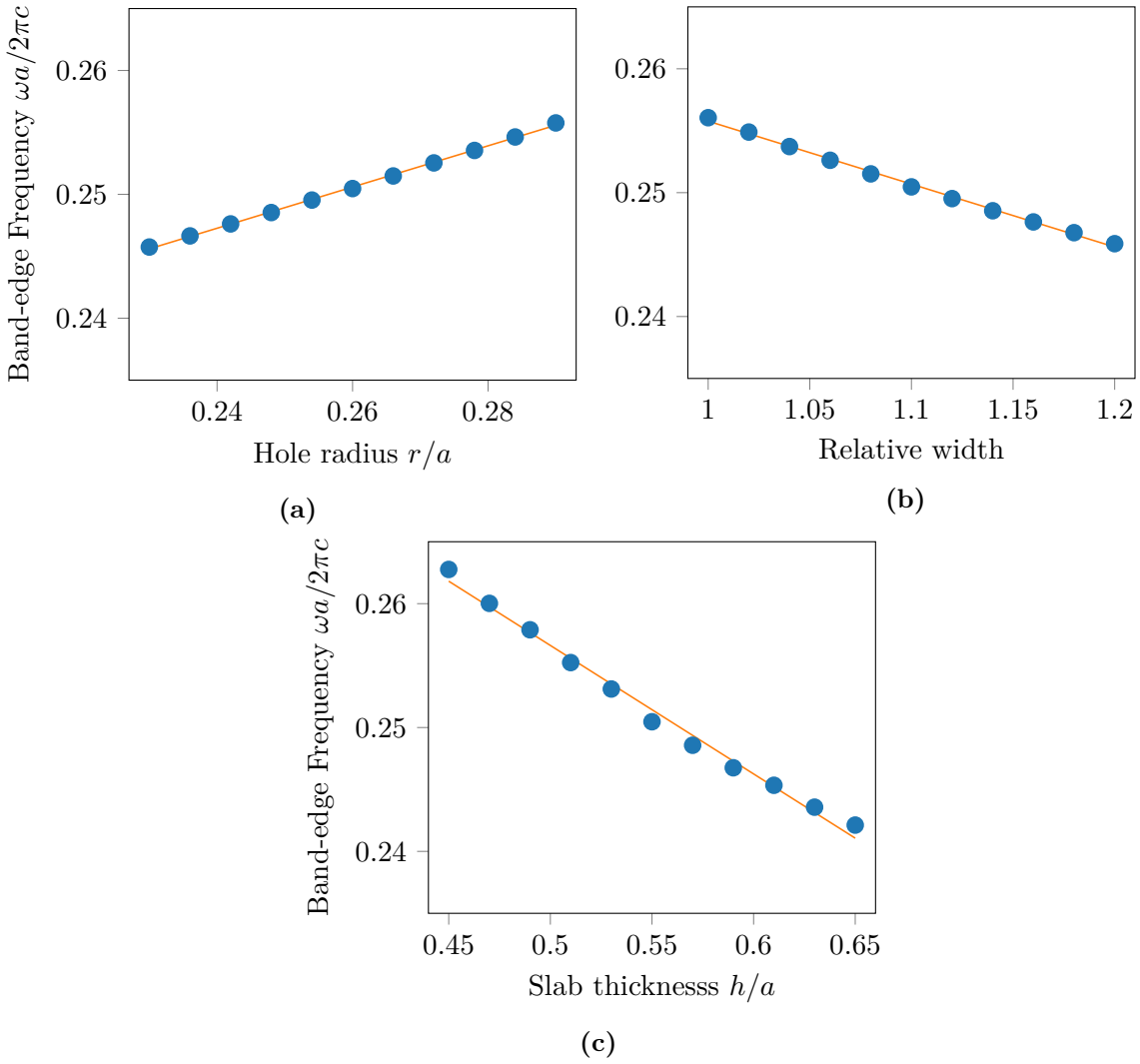

Figure 5.7: Band-edge frequency as a function of hole radius, relative width of waveguide and slab thickness, where the hole radii is $0.26a$, the relative width is 1.1 and the slab thickness is $0.55a$ while the others are varied. The blue dots are calculated frequencies, and the orange line is a linear fit to the data.

a smaller portion of the resonance mode for $r = 0.26a$ will therefore be lossy, even though the resonance modes for the two hole radii are nearly identical.

The resonance cavities discussed above have waveguides placed four rows above and below the cavity. If the loss to the waveguides is much smaller than the loss to the air/cladding, these waveguides will only affect the quality factor by a small amount. This will not necessarily be the case if the quality factor is increased further, and the waveguides were therefore omitted for the other heterostructure cavities considered here. The quality factor for the heterostructure cavity above with $0.26a$ and without waveguides was calculated to be 25,200, indicating that the coupling to the waveguides is sufficiently low to not change the quality factor significantly. To investigate the cavity size influence on the quality factor and resonance frequency, a heterostructure with an entire row of air holes removed was simulated using 3D FDTD. The quality factor increased from 25,200 to 91,500, while the resonance frequency was redshifted to 0.2535. The increase can be explained by the smoother decay of the mode outside the heterostructure and by a shift of the light line. The wave vector distribution width of the mode will be narrowed around $ka/2\pi = 0.5$, while the light cone will be closer to $ka/2\pi = 0$ due to the redshift of the resonance frequency, as shown in Figure 5.9a. It might seem contradictory to remove the entire row since the structure now will be a waveguide rather than a cavity. However, the confinement in the heterostructure cavity is due to the shift in lattice constant which results in a redshift to a frequency range below the lowest-lying modes of the linear defect waveguide (see Fig. 5.2b) where no propagating modes exist [45]. For comparison, the resonance frequency and quality factor for the heterostructure cavity with a removed row were calculated for an air-bridge. A quality factor of 1,200,000 was found, which is more than an order of magnitude larger than for the same SOI heterostructure cavity, similar to the relationship found in the project work. The quality factor for the air-bridge heterostructure is also comparable to the quality factors found by Song et al. [45]. The quality factor for the same structure using the 2D effective index approximation was found to be 130,000. The resonance frequencies and quality factors for the standard heterostructure cavity with a removed row for the three different material systems are shown in Table 5.1.

A natural development of the heterostructure with a removed row is to increase the width of the heterostructure itself. The widened heterostructure cavity described in Section was simulated using 3D FDTD and a resonance mode with frequency 0.2528 and a quality factor of 414,000 was found. Additionally, a different resonance mode with frequency 0.2541 and quality factor of 5,000 was also found. The resonance mode in the middle of the widened and the standard heterostructure cavity are shown in Figure 5.8. The widened heterostructure has a wider resonance mode as expected. Following Fourier theory, one would expect the wave vector distribution for the widened heterostructure to be narrower than for the standard heterostructure. In Figure 5.9, the Fourier transform of the resonance mode in the middle of the silicon slab along the defect is shown. The wide heterostructure mode has a narrower wave vector distribution as expected. A narrow wave vector distribution implies low radiation loss to the cladding and explains therefore the increase in quality factor.

5.1.5 Waveguide-Cavity Coupling Efficiency

With both waveguide and resonator sufficiently optimized, the focus can be put on the waveguide-cavity coupling. The coupling strength as a function of cavity-waveguide separation was estimated by placing waveguides with 10% increased width above and below the heterostructure cavity with a removed row and calculating the quality factor of the resonator. The waveguide-cavity separation was varied from two to six rows, and the coupling quality factor was estimated using Equation 2.24. The calculated coupling quality factors for SOI, air-bridge, and 2D SOI are shown in Figure 5.10. An exponential relation between the coupling quality factor and the waveguide-resonator separation is found, similar to what found by Faraon et al. [50]. The resonance mode decays exponentially in the photonic crystal, and the relationship between

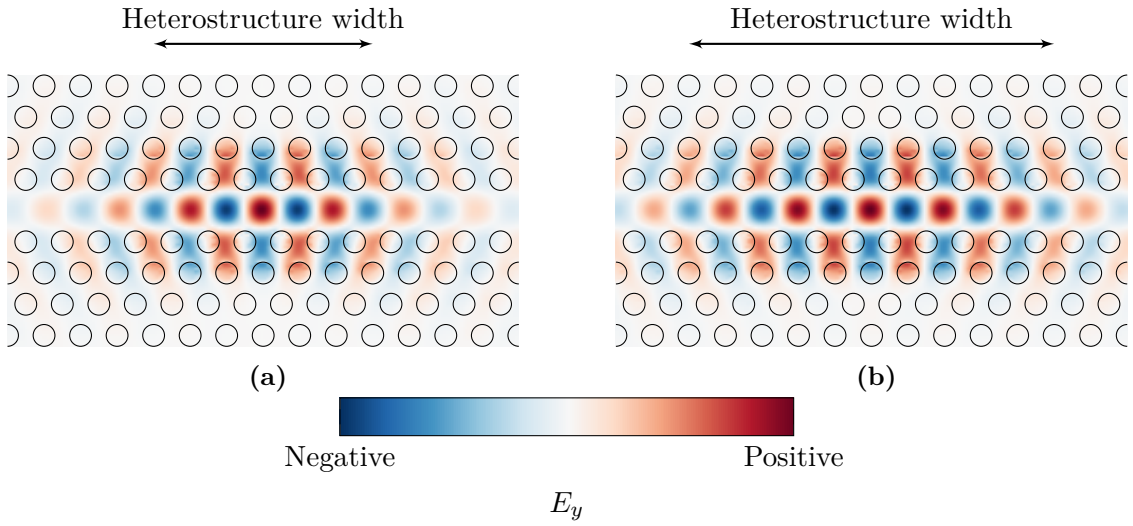

Figure 5.8: Resonance mode in the middle of the silicon slab for a standard and a widened heterostructure cavity.

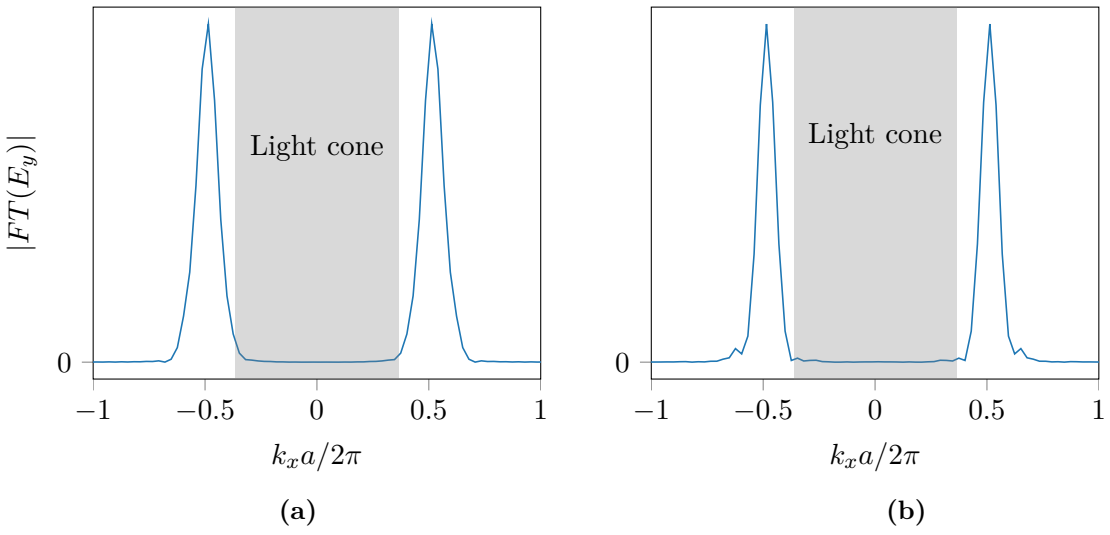

Figure 5.9: Fourier transform of the resonance mode in the middle of the silicon slab along the linear defect for (a) a standard heterostructure cavity and (b) a widened heterostructure cavity.

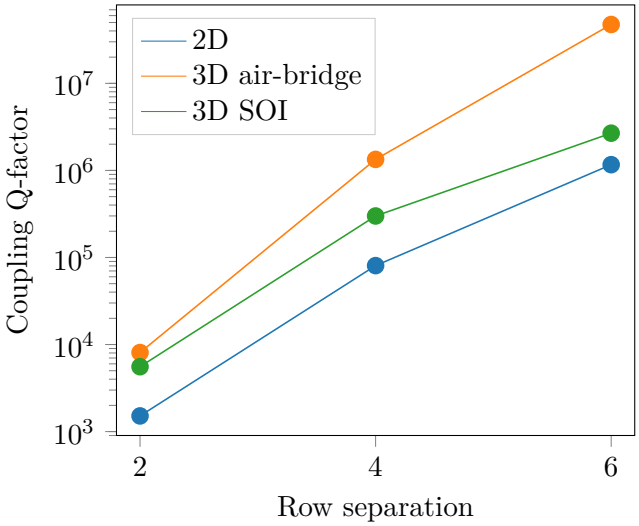

Figure 5.10: Coupling quality factor for heterostructure cavity between two parallel waveguides with 10% increased width.

waveguide-resonator separation and coupling quality factor is therefore as expected.

An SOI drop filter similar to the one considered in the project specialization with hole radius $0.32a$ and four rows between waveguide and cavity was simulated using 3D FDTD, and the dropped and transmitted intensity is shown in Figure 5.11a. The low transmission in the straight guide is explained by the hole radius and the widening of the waveguide for this structure. As mentioned above, a hole radius of $0.32a$ results in a high group index, which can result in high reflection loss at interfaces between PhC waveguide and strip waveguide [51, 52]. Additionally, the waveguide width in this structure was increased with 7%, which can have resulted in a too small band edge frequency shift. The most striking difference between the 3D drop filter and the 2D drop filter simulated earlier is nevertheless the intensity of the resonance peak in the spectrum for the receiver waveguide. As can be seen in Figure 5.11b, the dropped intensity at resonance is approximately 0.3% of the transmitted intensity at the same frequency. This is in stark contrast to the 2D drop filter where the resonance peak had a relative intensity of 31.4%. The difference is explained by the coupling quality factor in Figure 5.10 and the resonator quality factor in Table 5.1. Using Equation 2.27 a dropped intensity of 29% and 7% is found in 2D and 3D respectively using the cavity quality factors in Table 5.1. Since the quality factor in 3D is significantly reduced when increasing the hole radius from $0.26a$ to $0.32a$, the difference in dropped intensity at resonance is fairly well explained by the difference in resonator quality factor from 2D to 3D. A drop filter with hole radius $0.26a$, 10% widened waveguide, and a cavity-waveguide separation of two rows was then simulated, and the transmission spectrum for the bus and receiver waveguide is shown in Figure 5.11c. The increased quality factor of the resonator and the decreased coupling quality factor improves the dropped intensity at resonance, while the widened waveguide with smaller holes improves the transmission overall. The quality factor of the resonance peak shown in Figure 5.11d was calculated to be 11,500 using Harminv.

The effect of placing mirror boundaries in the bus and receiver waveguide was then tested for the 2D drop filter discussed above by terminating the waveguides 11 and 12 rows away from the center of the resonator. 2D FDTD was used to calculate the transmission spectrum for the filters, and the electric field norm at resonance were calculated in the frequency domain. The transmission spectra are shown in Figure 5.12 together with the corresponding steady state electric field norm at resonance. The intensity is close to zero at resonance for the mirrors placed 12 rows away from the cavity, while the relative transmission is approximately 78% for the drop

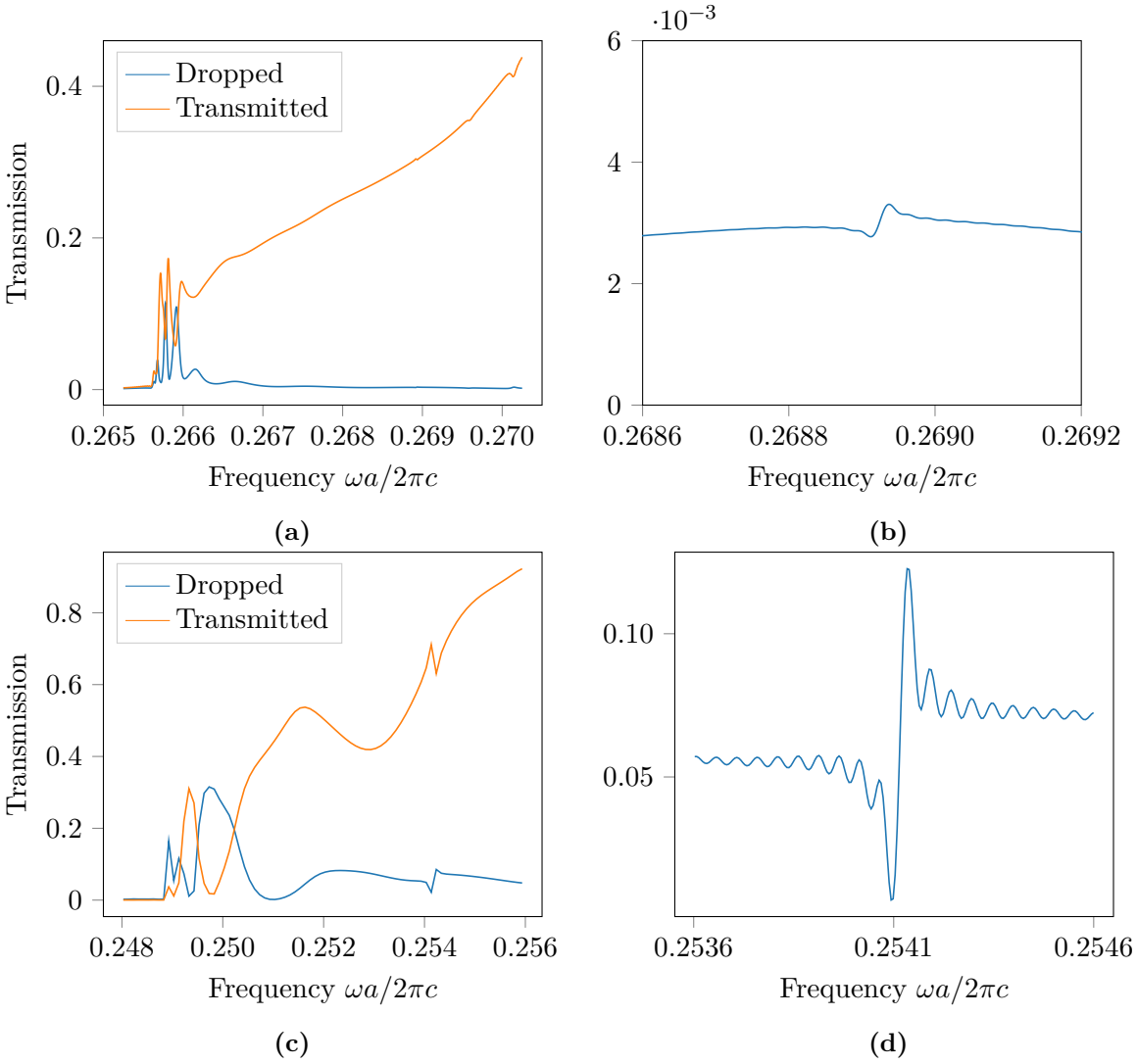

Figure 5.11: (a) Dropped and transmitted intensity for 3D SOI drop filter with $r = 0.32a$ and waveguide-resonator separation of four rows. Overall low transmitted intensity and almost neglible dropped intensity at resonance. (b) Dropped intensity at resonance is approximately 0.3%. (c) Dropped and transmitted intensity for 3D SOI drop filter with $r = 0.26a$ and waveguide-resonator separation of two rows. Transmission is increased and the resonance peak intensity is improved which can also be seen in (d).

filter with mirrors 11 rows away from the cavity center. The heterostructure makes it difficult to calculate the absolute phase shift introduced by propagating back and forth from the mirror boundaries since the wave vector will depend on the position in the waveguide. However, one can use Equation 2.28 to estimate α from the transmission at resonance in Figure 5.12a. The resonance transmission is approximately 1% resulting in $\alpha = 2.941$. The propagation constant in the waveguide for light with frequency equal to the resonance frequency in Figure 5.12b is $2.275/a$. The phase introduced by shifting the distance from mirror to cavity by a lattice constant is then 6.825 if the resonance frequency is assumed to remain constant. This phase shift will give a transmission of 92.8% using Equation 2.28. The difference between the theoretical transmission and the simulated in Figure 5.12b can be explained by the shift in resonance frequency when shifting the mirror boundary. If the frequency changes, the propagation constant in the waveguide will be changed, and the phase difference will not be as simple as stated above. Additionally, the waveguides terminated in the photonic crystal are not necessarily perfect mirrors, and the insertion loss in and out of the photonic crystal may have reduced the overall transmission. The improved transmission comes at the cost of a reduced total quality factor according to Equation 2.24. This is illustrated by the quality factors for the resonances shown in Figures 5.12c and 5.12d. These were calculated using Harminv to be 250,000 and 52,000, respectively.

A mirror in the bus waveguide was added to the SOI drop filter with $r = 0.26a$ discussed earlier. The already existing mirror in the receiver waveguide was shifted such that the mirror distance in both waveguides was 11 rows. The filter was simulated in 3D FDTD, and the transmission spectra shown in Figure 5.13 was calculated. Transmission of nearly 45% is achieved at resonance, compared to approximately 10% for the other configuration. Additionally, a quality factor of 9,800 was found with Harminv, which is only a slight reduction compared to the other drop filter. Placing mirrors in both waveguides allows for tuning of the transmission and the total quality factor of the filter. Instead of adding or removing air holes to change the mirror distance, one can change the radius of the air hole terminating the waveguide [27]. Changing the hole radius allows for finer tuning of the transmission since the mirror distance no longer is determined by an integer multiple of the lattice constant. A drawback with the drop filter with photonic crystal mirrors in both waveguides is that the multiplexing is no longer possible. Instead of creating mirrors by terminating the waveguides in the photonic crystal, one can in principle create a resonant mirror in the bus waveguide by adding a cavity supporting the same resonance mode as the drop filter cavity above the bus as suggested by Zhang et al. [27].

The drop filters considered so far have parallel bus and receiver waveguides. For all filters, light couples from bus to receiver close to the band edge frequency as can be seen in Figure 5.11a and 5.11c. This is especially apparent for the drop filter with mirrors in both waveguides 5.13a, where relatively high transmission occurs for a large band of frequencies. It is believed that the transmission is due to the overlap between the waveguides. A drop filter where the receiver waveguide was tilted was simulated using 3D FDTD, and the resulting transmission spectra are shown in Figure 5.14. The bus waveguide is terminated 11 rows away from the middle of the cavity, while the receiver waveguide is tilted 60° and placed three rows below the cavity and 4 rows next to the cavity center. A transmission peak with 20% relative intensity and a quality factor of 14,000 was found. Additionally, nearly zero transmission occurs for frequencies different than the resonance frequency. The coupling between cavity and receiver is efficient since the evanescent field tails of the cavity field are oriented 30° on the cavity axis as seen in Figure 5.14c [50], while the coupling between bus and receiver is greatly reduced due to the much smaller overlap. Tilted receiver waveguides can be particularly useful when designing multiplexer structures using photonic crystal drop filters since the high transmission near the band edge for parallel drop filters can make the multiplexer transmission spectrum more difficult to interpret.

A different method for improving the overall performance of the drop filter is to change from

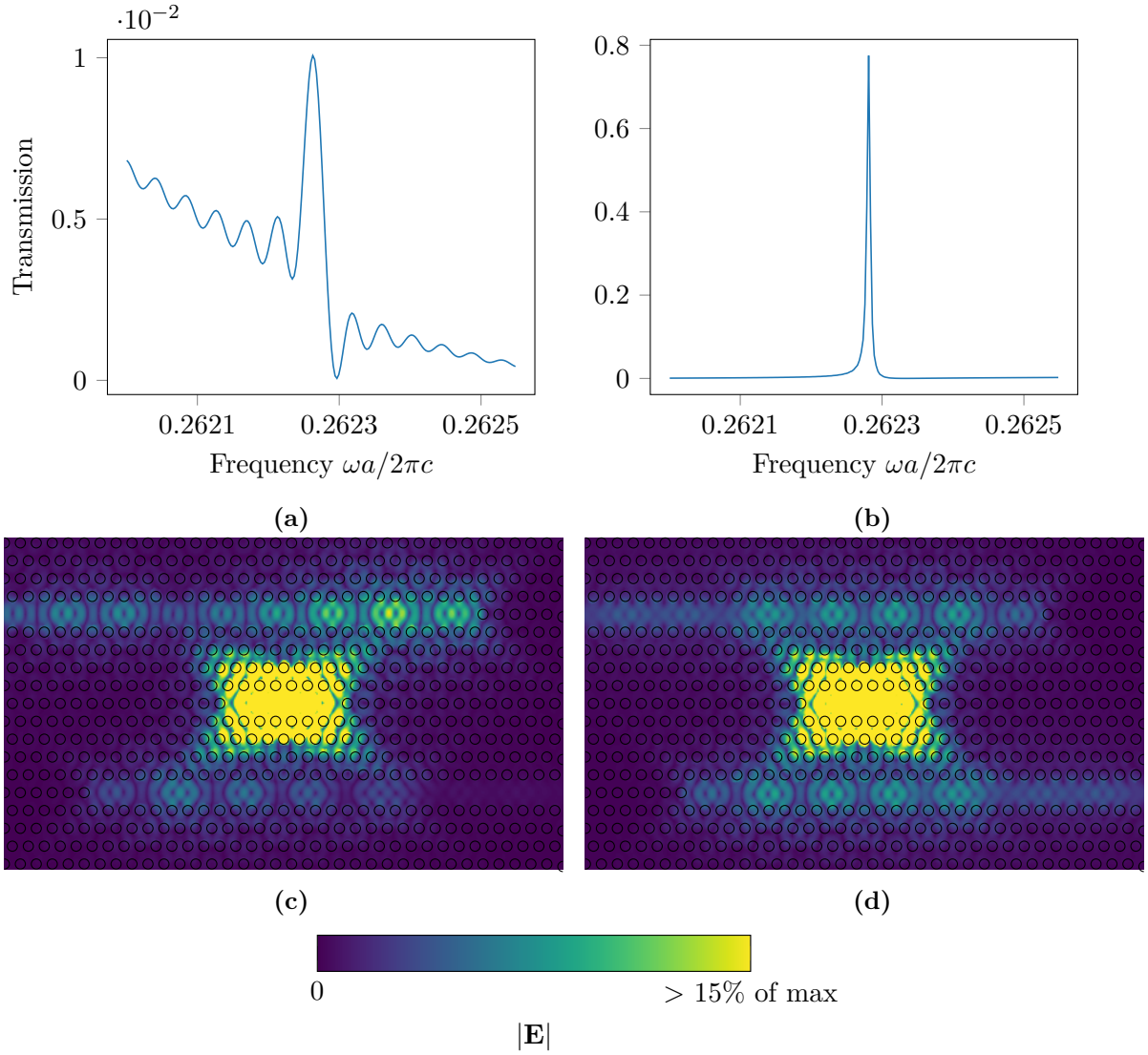

Figure 5.12: Dropped intensity in drop filter with mirrors placed (a) 12 and (b) 11 rows away from the center of the resonance cavity. The intensity at resonance is increased from 0.1% to nearly 80% from (a) to (b). The electric field norms for the two drop filters are shown in (c) and (d), where the scale of the colormap is adjusted to highlight the field at the input and output. In (c) the electric field norm goes to zero at the lower output, while in (d) the field norm is nearly equal at the input and output implying high transmission.

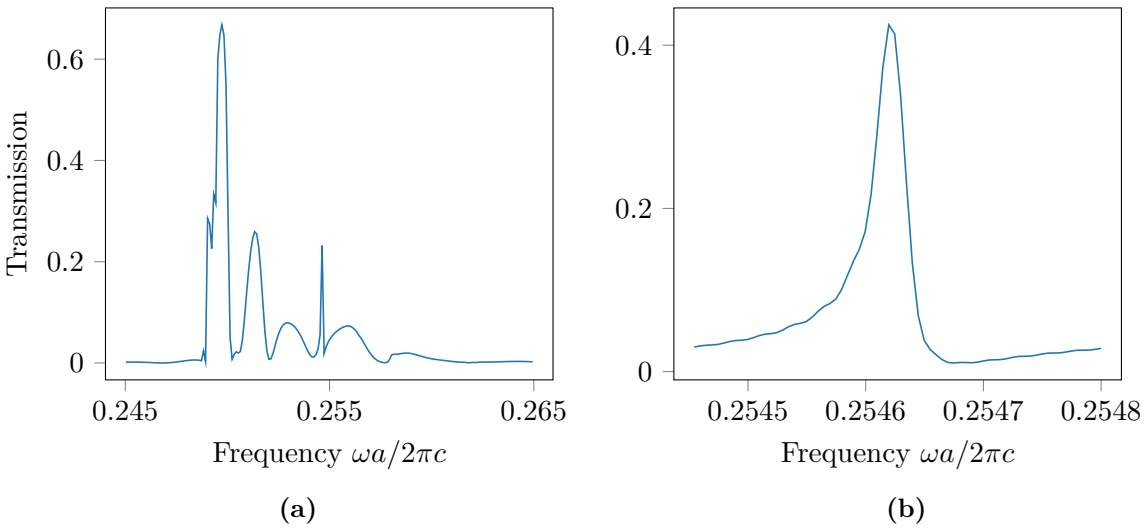

Figure 5.13: Transmission spectra for SOI drop filter with mirrors placed in bus and receiver waveguide. The spectrum in (b) has a higher spectral resolution explaining the difference in peak height compared to (a).

an SOI PhC to an air-bridge. The quality factor of the unloaded resonance cavity is more than 10 times higher than for SOI (see Tab. 5.1). From Figure 5.10, a high transmission should be achievable using a waveguide-resonator separation of four rows where the coupling quality factor is 300,000. The total quality factor of the filter will then be at least 130,000 using Equation 2.24, which is more than 10 times higher than for the SOI drop filter simulated above.

5.1.6 Multiplexing

A multiplexer based on the 2D drop filter simulated in the project work mentioned in Section 5.1.5 was simulated in 2D using Meep. Four drop filters were placed in series, and the lattice constants of the four photonic crystals were set to distribute the resonance peaks evenly in the wavelength range 1480 to 1620 nm. The drop filter has a unitless resonance frequency of approximately 0.262, and the lattice constants were therefore chosen to 417 nm, 409.7 nm, 402.3 nm and 395 nm for the four photonic crystals. The transmission spectrum for the multiplexer is shown in Figure 5.15a. Resonance peaks are found at 1507.5 nm, 1532.9 nm, 1562.8 nm and 1592 nm, almost exactly as intended. Additionally, one larger peak is found in the spectrum at 1580 nm. Compared to the result presented in the project report (see Fig. 5.15b), the performance of the multiplexer is improved significantly. The number of controlled resonance peaks is doubled, and the number of other peaks in the transmission spectrum is reduced. The number of holes removed to make the cavity was reduced compared to earlier. Increased cavity width in 2D gives rise to an increased number of high quality factor resonance modes, which is apparent in 5.15b. Additionally, the tilted output waveguide was widened by reducing the holes in the row next to the waveguide instead of removing two rows of air holes. The output waveguide in the new multiplexer should then guide the light better out of the photonic crystal. The multiplexer studied here should be transferable to a 3D system, but due to the reduction of resonance quality factor in 3D a cavity-waveguide separation of two rows instead of four might be needed. The receiver waveguides in the multiplexer discussed here consist of a section parallel to the cavity and a tilted section. Switching to the purely tilted receiver waveguide discussed earlier can be beneficial since this will remove much of the transmission near the band edge, which in turn can make the transmission spectrum easier to interpret. Furthermore, the interface between each block of photonic crystal can act as a wavelength dependent mirror since only the light with a frequency above the band edge frequency will propagate in the next photonic

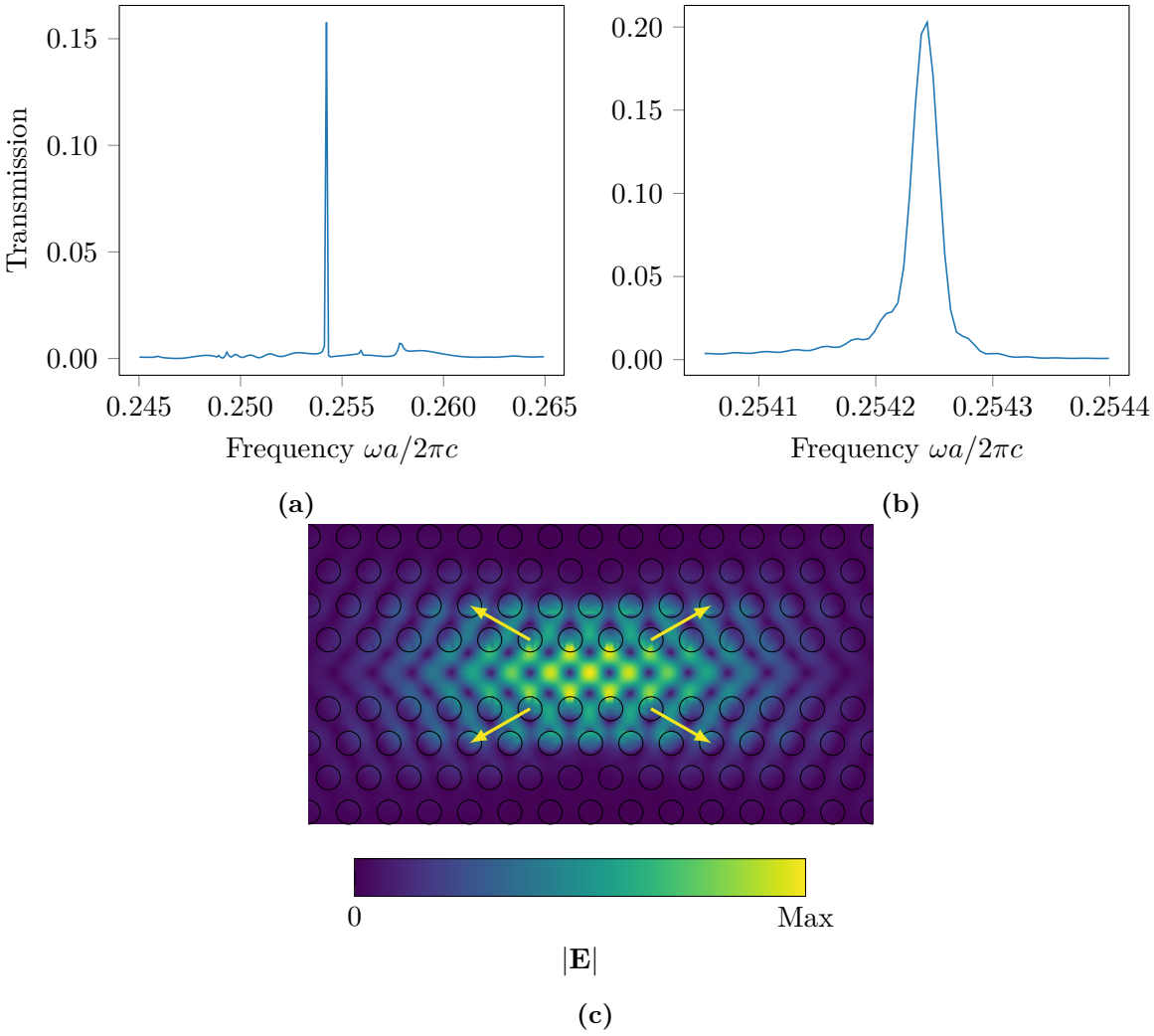

Figure 5.14: FDTD transmission for tilted SOI drop filter. The spectrum in (b) has a higher spectral resolution explaining the difference in peak height compared to (a). The electric field norm of the resonance mode is shown in (c) where the direction of the evanescent field tails is highlighted.

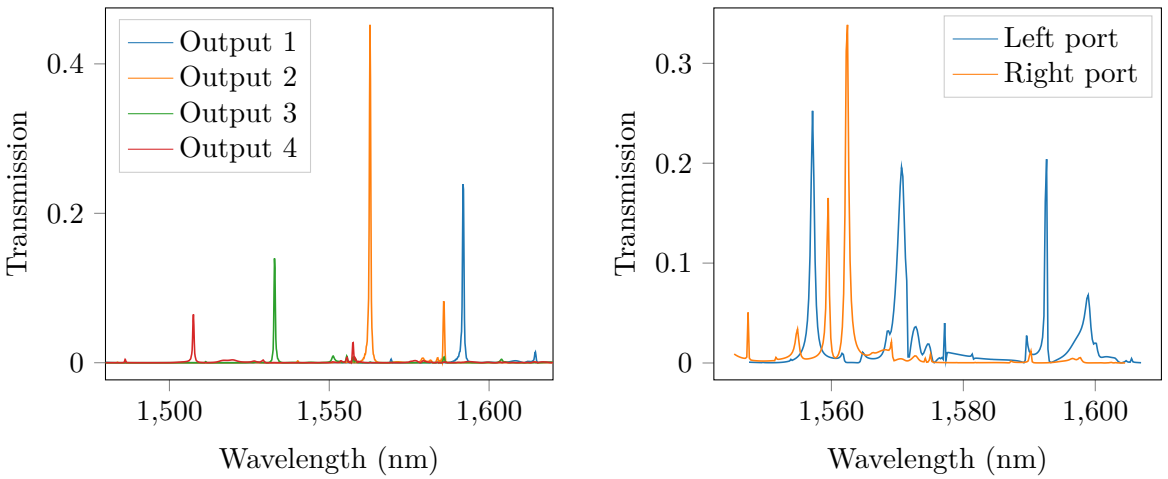

Figure 5.15: (a) Transmission spectrum for multiplexer with resonance peaks at at 1507.5 nm, 1532.9 nm, 1562.8 nm and 1592 nm. The peaks are large and clear, and there are almost no unintened peaks in the spectrum compared to (b), where the designed resonance peaks are found at 1562.4 nm and 1592.6 nm

crystal waveguide. By careful placement of the different blocks of photonic crystal, tuning of the transmission using mirrors as discussed earlier can be achieved.

5.1.7 Biosensing

The photonic crystal drop filter designed here is intended for use as a refractive index biosensor. Biosensing using the SOI drop filter with mirrors discussed above (with transmission spectra shown in Fig. 5.13a) was simulated using 3D FDTD. The transmission through a drop filter with water above the filter was calculated, and then a $0.05a$ thick biolayer was placed over the drop filter, and the transmission was calculated again. The transmission spectra are shown in Figure 5.16, where the lattice constant is set to 400 nm to make the biolayer 20 nm thick. The resonance peak shifts from 1589.82 nm to 1590.77 nm giving a redshift of 0.95 nm. This result is similar to what was found in the project work and by Lien in his thesis [3]. Compared to the transmission spectrum for the SOI drop filter surrounded by air, the relative intensity of the resonance peaks has increased from 45% to 73%, while the quality factor is reduced from 9,800 to 1,500. This can be explained by a change in resonance frequency and propagation constant when the surroundings are changed from air to water. The mirror placement is closer to giving perfectly constructive interference for the drop filter surrounded by water, which results in a higher transmission and a reduction in quality factor of the system. The quality factor of the resonance cavity does not contribute to the lowering of the total quality factor. The quality factor of the SOI heterostructure cavity made by removing a row increases from 91,500 to 170,700 when changing the surroundings from air to water. The cavity is already optimized to reduce radiation loss to the SiO_2 cladding. The loss due to light not satisfying TIR at the silicon-water interface should therefore be minimal since the refractive index of water is lower than for the cladding. The resonator mode should be more TE-like than before since the refractive indices of the bottom, and top layer is more similar than before, and thus making the system more symmetric. The modes will therefore couple less to lossy TM-modes [15], which can explain the increase in quality factor. Additionally, a redshift in frequency gives an increase in quality factor, since the SiO_2 light line is shifted. It should therefore be possible to design a biosensor with at least the same quality factor and transmission as achieved for the SOI drop filter discussed earlier. An increased quality factor of the filter used as a biosensor will

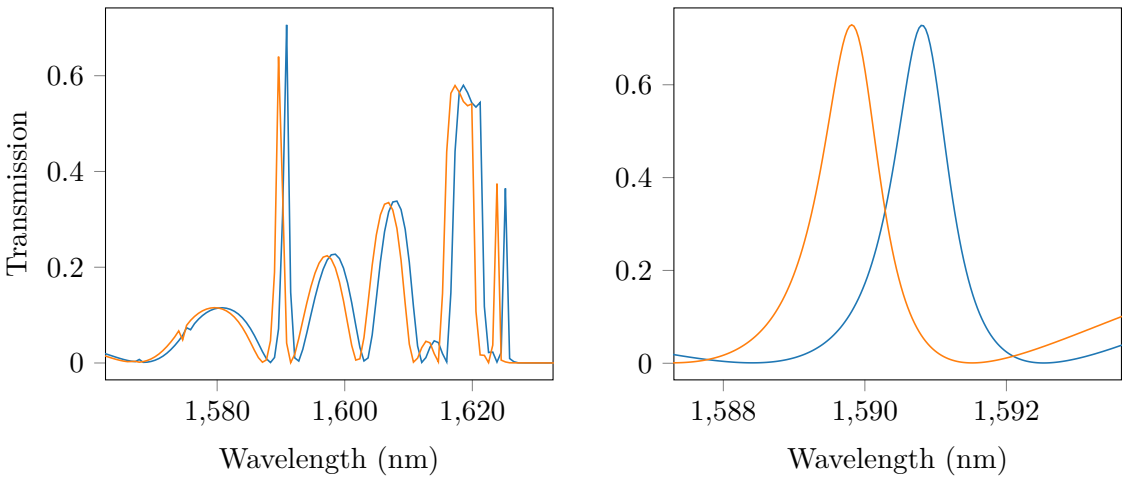

Figure 5.16: Resonance shift for 3D SOI drop filter with a 20 nm biolayer. The spectrum for a drop filter with water above (orange line) is shifted 0.95 nm when a biolayer is added (blue line).

Table 5.2: Resonance shift and quality factors for heterostructure cavity made in an air-bridge and in SOI.

Material system	$\Delta\lambda$ (nm)	Quality factor
Air-bridge	0.88	341,200
SOI	1.02	170,700

improve the resolution of the biosensor since smaller resonance shifts can be resolved. A high transmission increases the signal-to-noise ratio, which makes it easier to separate the resonance peak from noise.

As discussed earlier, the PhC drop filter based on an air-bridge structure has a theoretical performance far superior to the equivalent filter made in SOI. To test the performance when changing the surrounding medium from air to water, the quality factor of a standard heterostructure cavity in the two different systems was calculated using 3D FDTD. Additionally, the sensitivity of the two systems was tested by placing a 20 nm thick biolayer on top of the two resonators. The quality factors and the shift in resonance wavelength when $a = 400$ nm are shown in Table 5.2. The wavelength shift is nearly identical for the systems, with the SOI resonator slightly more sensitive. The relative difference in quality factors is reduced greatly from 13.33:1 to 2:1. Switching from an SOI filter to an air-bridge filter will not increase the sensitivity according to these calculations, and the performance of the air-bridge filter is reduced significantly when changing the surrounding medium from air to water. It is nevertheless expected that the air-bridge sensor will have a slightly higher detection limit since the quality factor is higher than for the SOI sensor. The wavelength shift when changing the medium from air to water is 18.6 nm for an SOI drop filter, an experiment easily verified for a fabricated sensor by placing a drop of water on top of the silicon slab.

The difference in sensitivity for the two systems can be discussed using perturbation theory (Eq. 2.18). The perturbation of the permittivity only occurs in the 20 nm thick layer above the silicon, and the perturbed frequency can be rewritten as

$$\Delta\omega = \frac{-\omega}{2}\frac{\varepsilon_{\text{bio}} - \varepsilon_{\text{water}}}{\varepsilon_{\text{water}}}\frac{\int_{\text{biolayer}} \mathrm{d}^3\mathbf{r}\varepsilon(\mathbf{r})|\mathbf{E}|^2}{\int_{\text{tot}} \mathrm{d}^3\mathbf{r}\varepsilon(\mathbf{r})|\mathbf{E}|^2}, \tag{5.1}$$

where the last factor is the electric energy in the layer above the silicon divided by the total

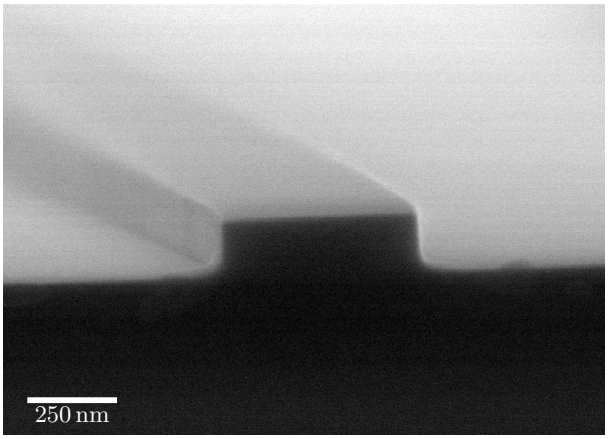

Figure 5.17: SEM cross-section image of strip waveguide.

electric energy of the mode before the perturbation. The relative electric energy in the biolayer was calculated to be 1.31% and 1.33% for SOI and air-bridge, respectively, using Meep. With unperturbed resonance wavelength of 1597.1 nm and 1592.6 nm, the resonance shifts in wavelength are calculated to be 2.16 nm and 2.20 nm for SOI and air-bridge, respectively. The results are in the same order of magnitude as the 3D FDTD simulation results shown in Table 5.2. The error in the approximation is usually neglible when the relative change in permittivity in the perturbed region is smaller than 1% [15]. The relative change in permittivity in the biolayer is close to 20%, suggesting that more terms are needed to calculate the wavelength shift accurately. First order perturbation theory nevertheless shows that increasing the relative electric energy in the volume where the refractive index change will increase the sensitivity. Further design of the heterostructure cavity should aim to improve the relative electric energy in this volume.

5.2 Fabrication

This section presents the results from the fabrication of optical devices in SOI, with emphasis on the different fabrication steps used. The results are presented in the same order as the process steps are listed in Chapter 4. Fabricated devices such as strip waveguides, PhC waveguides, and PhC drop filters will be discussed in detail in Section 5.3.

5.2.1 Film Thickness

The SOI samples were made by depositing a-Si on 15x15 mm^2 samples of thermally grown SiO_2 on silicon. The film thickness was measured by taking cross-section images of the sample after EBL and etching, and measuring the thickness of a strip waveguide as seen in Figure 5.17. The film thickness was measured to be 220 nm for the two samples measured, which is the intended film thickness. Measuring the film thickness using the cross-section requires cleaving of the sample normal to the waveguides. This is also necessary to do in order to couple light into the strip waveguides, and the film thickness was therefore measured using the otherwise useless cleaved sides of the sample. A consequence of this is that the film thickness was measured 5 mm away from the center of the sample, where the photonic crystal devices were placed. From visual inspection of the samples after a-Si deposition it was clear that the film thickness varied from the center of the sample and outwards, although the film color was fairly uniform in the 10x10 mm used for making optical circuits. One can therefore expect that the samples had a film thickness slightly smaller than 220 nm at the center of the sample. This could be verified by breaking a sample at the middle. A less invasive technique for measuring film thickness is reflectometry,

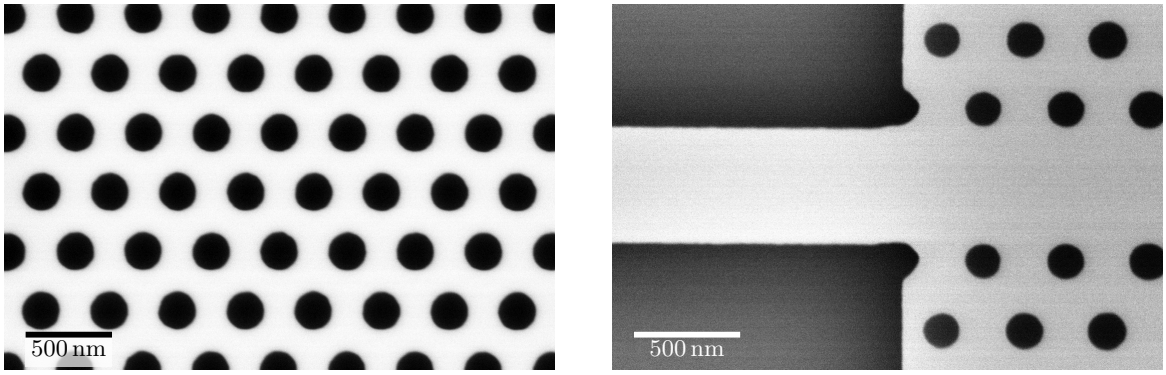

(a) (b)

Figure 5.18: (a) Photonic crystal with hole radius of 108 nm. (b) Strip waveguide - PhC waveguide interface.

Table 5.3: Comparison of patterned feature sizes and mask design.

Feature	Mask size (nm)	Measured size (nm)
Waveguide width	581	545
Hole radius	104	108
Lattice constant	400	395

but this technique gave inconsistent results compared to measuring the cross-section using SEM. Inconsistent measurements of silicon thickness using reflectometry have been observed in the research group earlier [1], and it is believed that the multilayer structure is not well modeled by the material models of the reflectometry system. For future work, depositing silicon before breaking the wafer into smaller pieces is recommended to reduce thickness variation across the sample.

5.2.2 Lithography

Mask design was transferred to the SOI samples by EBL and ICP-RIE. Resist cracking has been a problem for earlier Master's students [2, 3], but this was not seen for any of the fabricated devices indicating that the lithography steps listed earlier results in good adhesion and minimal stress in the resist film. As seen in Figure 5.18, the exposure dose of 350 $\mu C/cm^2$ and current of 1 nA resulted in high quality photonic crystals and strip waveguides. However, the size of the patterned features is different from the mask design as can be seen in Table 5.3. The difference in feature size between the mask and the fabricated device is explained by over-exposure due to electron scattering in the resist and a long etching time needed to etch through the silicon film. The increase in hole radius and decrease in waveguide width can be opposed by making the air holes smaller and the waveguides larger in the mask design. The lattice constant deviation from the mask design is harder to explain, but this was also easily adjusted by increasing the lattice constant in the mask.

During initial fabrications, exposure of different components with different currents was tested. Reducing the electron beam current from 1 nA to 100 pA has been shown to increase patterning resolution and reduce sidewall roughness [1]. It was not feasible to expose the whole design with 100 pA, due to increased exposure time when reducing the current. The photonic crystal was therefore exposed with 100 pA since it is expected that this part of the design is most sensitive to fabrication roughness and irregularities, while the strip waveguide was exposed with 1 nA. The resulting structure is shown in Figure 5.19, where there is an alignment error between the waveguide and the photonic crystal. The alignment error is most probably due to drift of

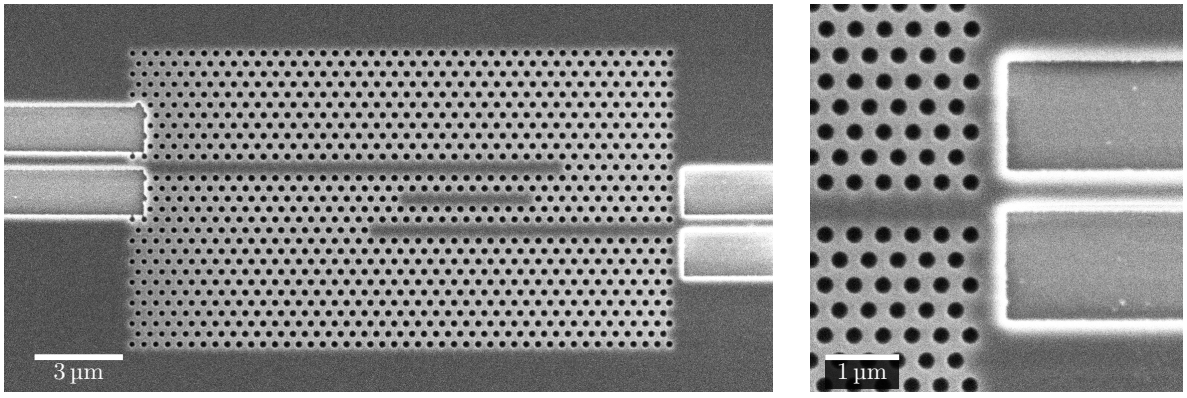

(a) **(b)**

Figure 5.19: (a) Alignment error between photonic crystal drop filter exposed with 100 pA and waveguide exposed with 1 nA. (b) The at interface between strip waveguide and PhC waveguide.

the sample between the different exposures. Exposure with different currents is done separately, and a waiting step of 45 min was used after switching current to stabilize the beam. The reason for the drift is believed to be the temperature difference introduced when entering the EBL chamber and loading the sample. The otherwise precisely controlled chamber temperature will change during the loading of the sample, and this can cause a drift of the sample. Adding a 45 min waiting step before the first exposure has been shown to reduce the alignment error [3].

5.2.3 Etching

Initially, the samples were etched for 45s since this was found to be sufficient for etching 220 nm a-Si earlier [3]. As seen in Figure 5.17 this etch time resulted in a completely etched strip waveguide with nearly vertical sidewalls. The same sample was later cleaved along the middle of the sample to take cross-section images of a photonic crystal, as shown in Figure 5.20. The etch depths of the photonic crystal holes are measured to be 189 nm. The etch rate of the PhC holes relative to the waveguide is reduced by 14%. The difference in the etch rate is explained by loading effects discussed in Section 3.3.4. The etch selectivity of silicon for the etch used here is 5.1:1 towards SiO_2 according to Holmen [1]. The cladding can therefore be utilized as an etch stop to prevent underetching of the waveguide when increasing the etch time to etch the holes completely. The etch time was therefore increased to 60s for the remaining samples. Overetching the waveguide can, however, increase chemical etching of the waveguide sidewall resulting in an increased sidewall roughness and thus increased loss [1].

5.2.4 Polymer Waveguides and Inverted Tapers

Polymer waveguides made by SU-8 were fabricated using photolithography instead of EBL as done earlier [1, 3] greatly simplifying alignment to the strip waveguides. The first attempts on fabricating inverted taper waveguides covered by polymer waveguides were made by spin coating SU-8 directly on a plasma cleaned patterned SOI sample with no adhesion promoter. After development and blow drying with N_2, several of the polymer waveguides were displaced from their initial position, and a few had disappeared completely after breaking the sample. Rough handling, too hard N_2 drying and poor adhesion to the silicon substrate were believed to be the reason for the failed fabrication of polymer waveguides. The following samples were primed with HMDS before spin coating, and the drying was performed by light blowing of N_2 perpendicular to the sample surface at the center of the sample. In Figure 5.21, a polymer waveguide made using these alterations is shown. The overview image (Fig. 5.21a) shows good

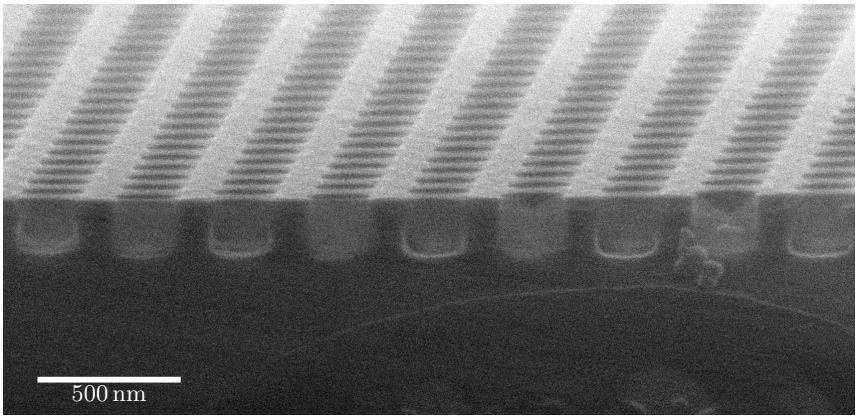

Figure 5.20: Cross-section SEM image of a photonic crystal.

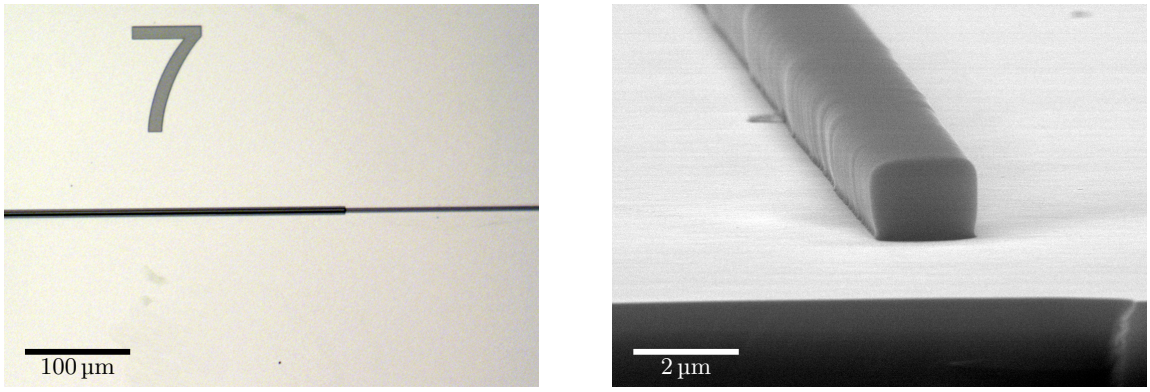

(a) **(b)**

Figure 5.21: (a) Optical micrograph of a 2 µm thick SU-8 waveguide deposited over a silicon strip waveguide. (b) Cross-section SEM image of SU-8 waveguide where the cross-section area is close to 2x2 μm^2.

alignment between the polymer waveguide and the underlying inverted taper waveguide. The polymer waveguide has a width and height close to 2 µm as shown in Figure 5.21b.

5.3 Optical Measurements

Optical measurements were performed on seven SOI samples using the setup described in Section 4.3.2. The results are compared to the simulation results discussed earlier.

5.3.1 Fiber-to-Strip Waveguide Coupling

Initially, coupling of light from the tapered fiber to the sample was done by butt coupling to a tapered silicon strip waveguide. This method for increasing the coupling efficiency was chosen since no extra lithography steps are needed. Good results were generally achieved using tapered strip waveguides, as seen for the photonic crystal waveguide and drop filters discussed in later sections. However, aligning fibers to the tapered waveguides and achieving good coupling was tedious and a relatively high detector amplification was needed. Therefore, using inverted tapers and polymer waveguides to enhance coupling efficiency was tested. Generally, the detector amplification was reduced by at least a factor of ten compared to the amplification needed to achieve similar transmission earlier, similar to what was found by Lien [3]. The alignment of fiber to waveguide was also greatly simplified. Coupling light from fiber to polymer waveguide

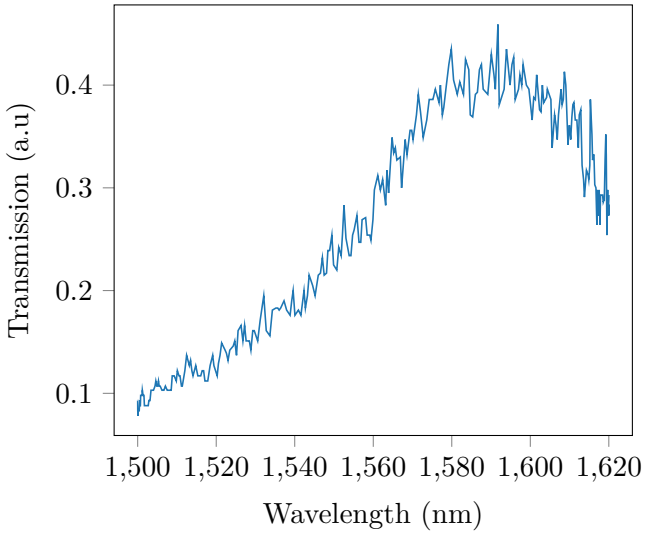

Figure 5.22: Transmission spectrum for strip waveguide using an inverted taper at the input. The transmission spectrum strongly resembles the laser output spectrum found in the laser datasheet [63].

is more efficient than coupling to strip waveguide due to a larger geometric overlap and a smaller difference in refractive index [55, 60]. A transmission spectrum for a strip waveguide using inverted tapers for coupling light into the device is shown in Figure 5.22. The spectrum is similar to the laser output spectrum found in the datasheet for the laser [63] indicating that both coupling to and light guiding in the strip waveguide is fairly good. For many photonic crystal devices, significant Fabry-Perót fringes were found in the transmission spectrum indicating that the interface between the PhC waveguide and the strip waveguide, and the cleaved end of the strip waveguide act as partially reflecting mirrors. Using inverted tapers at the output is suggested by McNab et al. [60] to reduce Fabry-Perót fringes, and was tested here without any success. An alternative method for reducing Fabry-Perót fringes is to use grating couplers for coupling light in and out of the sample, which have given good results for Lai et al. [14].

5.3.2 Photonic Crystal Waveguide

A PhC waveguide (shown in Fig 5.23) was fabricated with a measured lattice constant of 395 nm and hole radius of 108 nm. The transmission spectrum for the waveguide is shown in Figure 5.24. The unitless frequency range considered here is 0.247 to 0.263, and the spectrum is close to the spectrum simulated using 3D FDTD shown in Figure 5.4. The transmission in the higher frequency range is higher in the simulation, but this is mainly due to the power output of the laser, which is not uniform as seen in Figure 5.22. The band edge frequency is lower for the simulated waveguide. This is however expected since the r/a ratio is larger for the fabricated waveguide than for the simulated waveguide and increasing the r/a ratio will increase the band edge frequency (see Fig. 5.7). The large difference in transmission when decreasing the wavelength from above the band edge to below the band edge, from 1585 to 1584 , was also easily visible using the IR camera as seen in Figure 5.25

5.3.3 Photonic Crystal Drop Filter

PhC drop filters in SOI were made by placing waveguides two rows above heterostructure cavities where 11 air holes were removed. In Figure 5.27a the transmission spectrum for the drop filter in Figure 5.26 is shown. The spectrum is similar to the simulated dropped transmission for a drop filter with the same number of removed holes but without a mirror in the bus waveguide

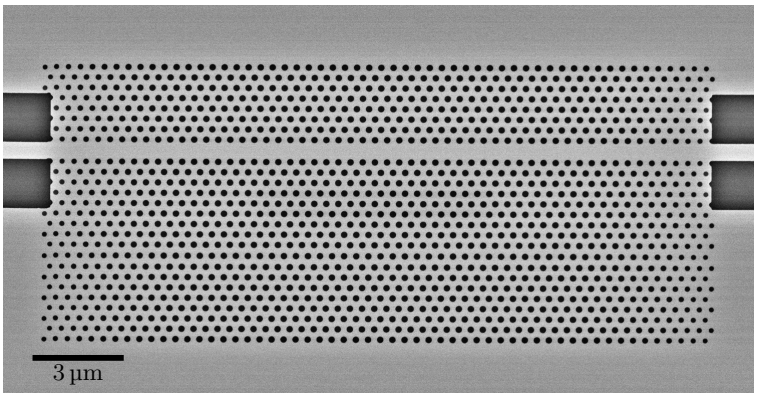

Figure 5.23: PhC waveguide with hole radius of 108 nm and lattice constant of 395 nm. Hole radius taper is used at both ends of the photonic crystal.

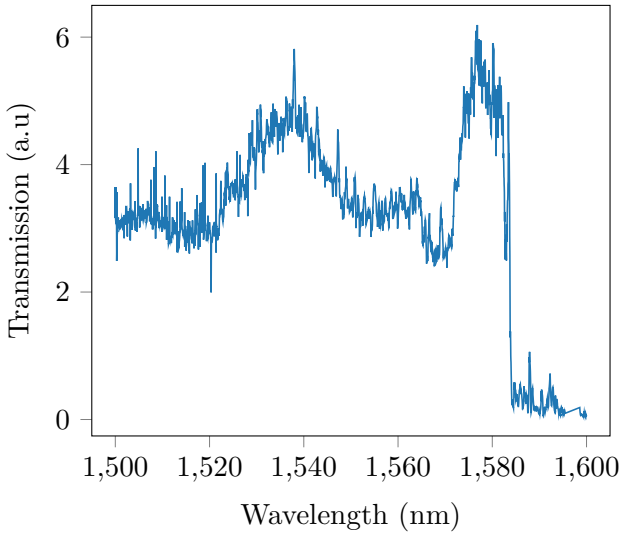

Figure 5.24: Transmission spectrum for the PhC waveguide shown in Figure 5.23. The spectrum is similar to simulations, and the band edge is found at 1584 nm.

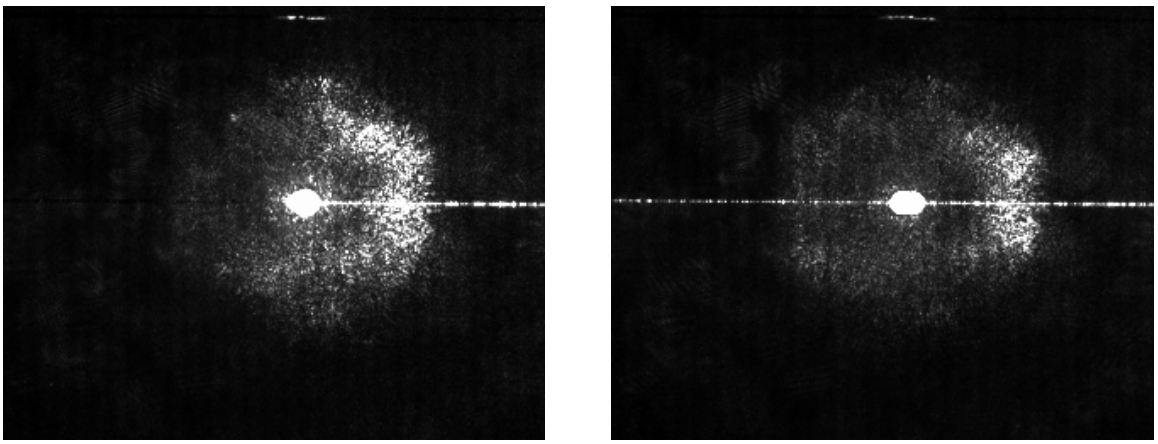

(a) **(b)**

Figure 5.25: IR image of the photonic crystal waveguide in Figure 5.23 where the laser wavelength is set to (a) 1585 nm and (b) 1584 nm. Light enters the sample from the right, and the large white spos in the middle of the images is the photonic crystal waveguide.

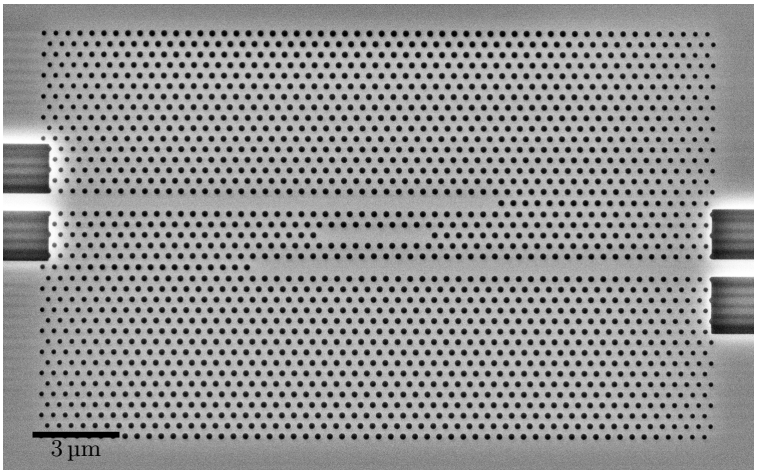

Figure 5.26: PhC drop filter using a heterostructure cavity with 11 air holes removed. The waveguides are placed 2 rows above and below the cavity, and mirrors are formed 10 rows away for the cavity center.

(see Fig. 5.11c). Several transmission peaks occur near the band edge in both spectra, and a rather small resonance peak is found at a unitless frequency of 0.256 for the fabricated filter and 0.254 for the simulated filter. The quality factor of the resonance peak was estimated to be 2,100, which is smaller than what found in simulations for the drop filter in air.

The refractive index sensitivity of the drop filter above was tested by depositing a drop of water on top of the sample and measuring the shift of the resonance peak. As seen in Figure 5.27, the resonance shift was measured to be 21.1 nm. This is very close to the simulated resonance shift of 18.6 nm when changing the surroundings from air to water discussed in Section 5.1.7.

The mirror placement was then investigated by fabricating two drop filters with a heterostructure cavity made by removing 19 air holes. The waveguides were placed two rows above the cavity, and the mirror distance was set to 11 and 12 rows. The transmission spectra for the two drop filters are shown in Figure 5.28. The transmission was generally larger in the filter with mirror distance of 11 rows (Fig. 5.28a), and there is therefore less noise in this spectrum compared to the transmission spectrum for the filter with mirror distance of 12 rows (Fig. 5.28b). The resonance peak at 1558 nm in Figure 5.28a is more clear than the one found at 1558 nm in Figure 5.28b, indicating that a mirror distance of 11 rows is closer to constructive interference than 12 rows. The high transmission near the band edge also changes character from several distinct peaks to one larger peak when changing the mirror distance, indicating that these peaks are due to overlap between bus and receiver waveguides rather than actual resonance peaks. The low intensity of the resonance peaks compared to the peaks near the band edge is explained by the wavelength dependent output of the laser shown in Figure 5.22. An alternative method for changing the mirror distance is to vary the hole radius of the air hole terminating the waveguides. Fabricating several drop filters where the radius of this air hole is varied could give a better picture of the mirror distance dependence on the resonance peak.

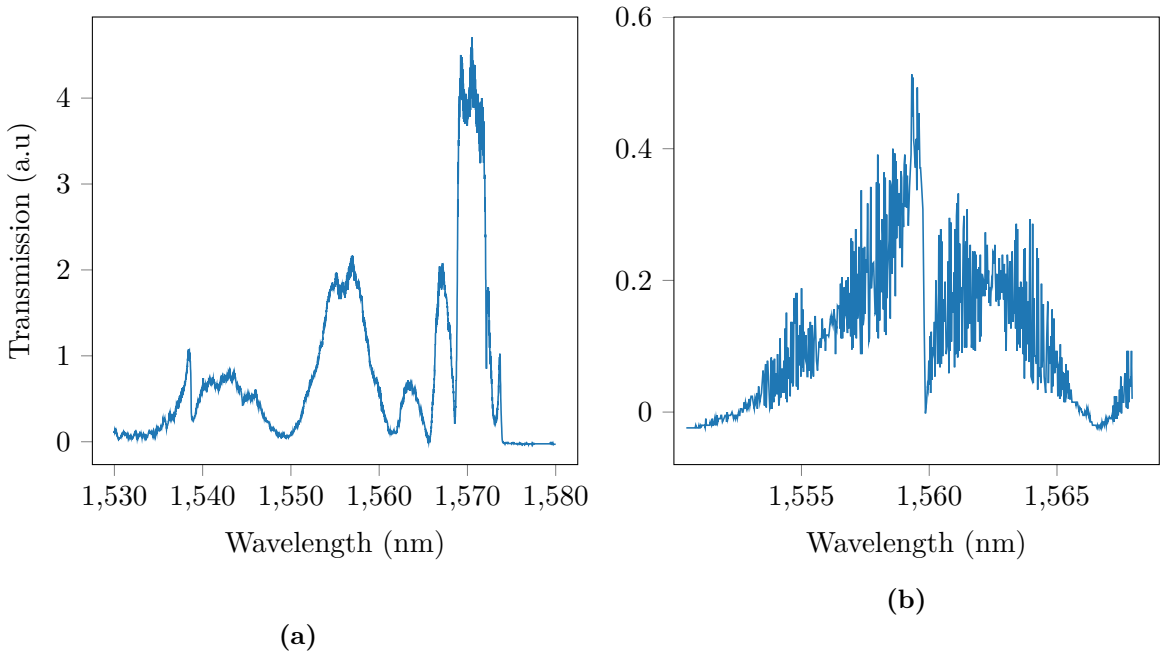

Figure 5.27: (a) Transmission spectrum for the drop filter shown in Figure 5.26. The spectrum is similar to the simulated spectrum shown in 5.11c, and the heterostructure cavity resonance is found at 1538.5 nm. (b) The resonance peak was redshifted to 1559.6 nm after depositing a drop of water on top of the drop filter. Noise is more prominent in the spectrum where water is placed above the filter.

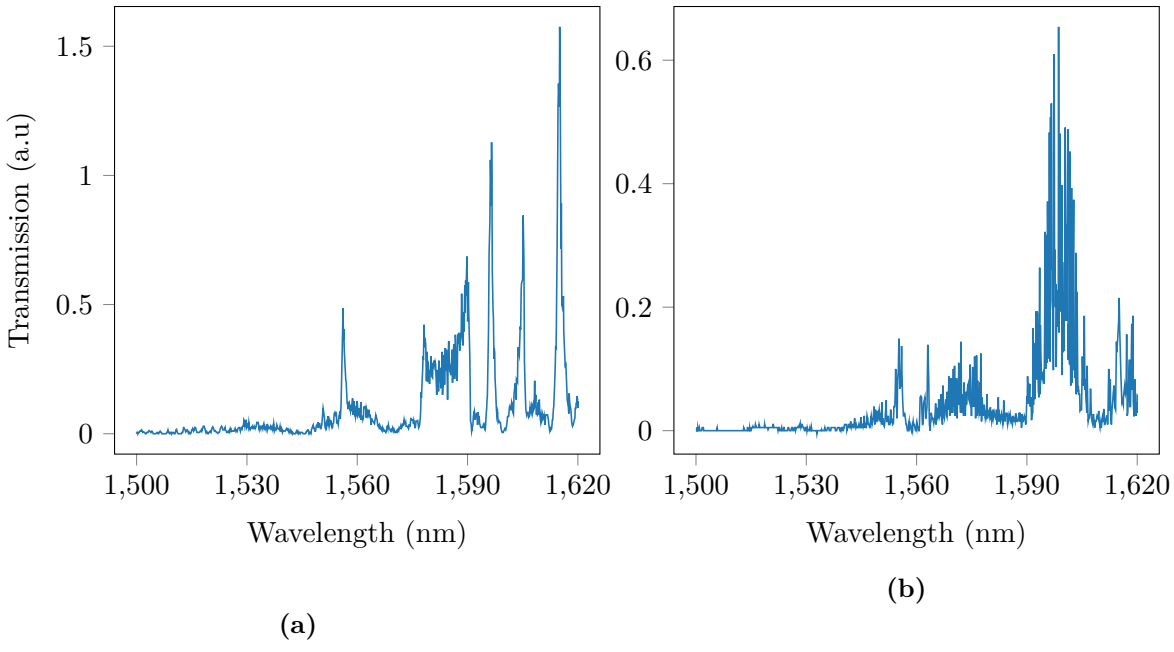

Figure 5.28: Transmission spectrum for drop filters with mirror distance of (a) 11 rows and (b) 12 rows. The resonance peak at 1558 nm is larger for 11 rows than for 12 rows.

Chapter 6

Conclusion

In this project work, a photonic crystal drop filter made of a resonator placed between two waveguides have been considered for use as a biosensor. The different components of the filter, as well as functioning filters, have been designed and optimized using frequency-domain and time-domain simulations. In parallel, photonic crystal waveguides and drop filters have been fabricated at NTNU Nanolab using electron beam lithography and tested using a tunable laser.

Simulations

The input and output waveguides of the drop filter were optimized using eigenmode computations. A reduction of the photonic crystal hole radius compared to earlier work [2] was found to increase the group velocity of guided modes in the frequency range of interest. Furthermore, increasing the width of the waveguide, either by shifting the photonic crystal above and below the waveguide or by reducing the radius of the holes next to the waveguide, was shown to redshift the band of guided modes. Increasing the group velocity and redshifting the frequency of the guided modes are important to be able to guide light effectively in and out of the photonic crystal. The eigenmode computations were confirmed by 3D transmission simulations using FDTD.

The resonator was then considered using 3D FDTD. The quality factor of the resonator was improved by more than an order of magnitude compared to the project work done prior to the master's project by reducing the hole radius, and increasing heterostructure and cavity width. Increasing the quality factor of the resonator can increase the resolution of the PhC drop filter biosensor. Additionally, a large quality factor of the resonator makes it possible to achieve a large transmission through the filter at resonance, which in turn increases the signal-to-noise ratio of the biosensor.

The transmission of the filter was analyzed using temporal coupled-mode theory, and the decay rate from the resonance cavity to waveguides was found using 3D FDTD. The transmission of the filter was improved by placing the waveguides closer to the resonator as expected, and the effect of placing mirrors in the waveguides was discussed. Using the latter approach, the transmission at resonance was increased by a factor of five.

Photonic crystal drop filters can be used to create a multiplexed biosensor able to detect several antigens at the same time. A multiplexed device with four tunable resonance peaks was designed by placing drop filters with a different lattice constant in series and simulated using 2D FDTD. The number of tunable peaks was doubled, and the number of unaccountable peaks was reduced significantly compared to earlier work by the author.

Lastly, the refractive index sensitivity of the photonic crystal drop filter was qualitatively tested by changing the surroundings of the drop filter from air to water, and adding a dielectric layer above the silicon slab using 3D FDTD. A resonance shift near 1 nm was found, which is well within the detectable range of the optical equipment at the research group.

Fabrication

Characterization of fabricated devices made using thin film deposition, patterning by lithography and plasma etching showed good control of feature dimensions important for the photonic crystal drop filter. The characterization was supported by optical measurements on fabricated photonic crystal waveguides and drop filters, where transmission spectra similar to simulations were found. The quality factor of the resonance peak found for the drop filter was significantly lower than what achieved in simulations, indicating that the loss due to surface roughness is significant for the resonance cavity considered here. The resonance shift when depositing a drop of water on top of a drop filter was similar to what was found in 3D FDTD simulations, giving a rough estimate of the refractive index sensitivity of the drop filter and illustrating the application of the drop filter as a photonic biosensor.

Future Work

Following this thesis, there are many aspects of the drop filter-based biosensor that can be improved further. The aspects I find most interesting are listed below:

- The distance between waveguides and cavity can, in theory, be increased from two to four rows for the resonance cavity discussed here, which will increase the quality factor of the filter and reduce the transmission due to waveguide-waveguide coupling. This should be tested using 3D FDTD simulations and for a fabricated drop filter.
- A multiplexed biosensor should be simulated in 3D. Tilted output waveguides should be considered for the multiplexer since the design is simplified, and the transmission off resonance is shown to be very low.
- Reducing the exposure current to 100 pA when patterning the photonic crystal in EBL should be tested to see if the quality of the sidewalls influence the performance of the filter.

Bibliography

[1] Lars Grønmark Holmen. "Simulation and Fabrication of a Photonic Crystal Mach-Zender Interferometer". Master's Thesis. Norwegian University of Science and Technology, 2016.

[2] Ingerid Gjeitnes Hellen. "Simulation and Fabrication of Two-dimensional Photonic Crystal Drop Filters for Biosensing". Master's Thesis. Norwegian University of Science and Technology, 2018.

[3] Størk Lien. "Simulation and Fabrication of a Photonic Crystal Transmission Filter for Biosensing Applications". Master's Thesis. Norwegian University of Science and Technology, 2018.

[4] Rebecca L Siegel, Kimberly D Miller, and Ahmedin Jemal. "Cancer statistics, 2019". In: *CA: a cancer journal for clinicians* 69.1 (2019), pp. 7–34.

[5] M Carmen Estevez, Mar Alvarez, and Laura M Lechuga. "Integrated optical devices for lab-on-a-chip biosensing applications". In: *Laser & Photonics Reviews* 6.4 (2012), pp. 463–487.

[6] Xudong Fan et al. "Sensitive optical biosensors for unlabeled targets: A review". In: *analytica chimica acta* 620.1-2 (2008), pp. 8–26.

[7] Jiří Homola. "Surface plasmon resonance sensors for detection of chemical and biological species". In: *Chemical reviews* 108.2 (2008), pp. 462–493.

[8] Qing Liu et al. "Highly sensitive Mach–Zehnder interferometer biosensor based on silicon nitride slot waveguide". In: *Sensors and Actuators B: Chemical* 188 (2013), pp. 681–688.

[9] Jonas Flueckiger et al. "Sub-wavelength grating for enhanced ring resonator biosensor". In: *Optics express* 24.14 (2016), pp. 15672–15686.

[10] Mindy Lee and Philippe M Fauchet. "Two-dimensional silicon photonic crystal based biosensing platform for protein detection". In: *Optics express* 15.8 (2007), pp. 4530–4535.

[11] Eli Yablonovitch. "Inhibited spontaneous emission in solid-state physics and electronics". In: *Physical review letters* 58.20 (1987), p. 2059.

[12] Sajeev John. "Strong localization of photons in certain disordered dielectric superlattices". In: *Physical review letters* 58.23 (1987), p. 2486.

[13] John D Joannopoulos, Pierre R Villeneuve, and Shanhui Fan. "Photonic crystals: putting a new twist on light". In: *Nature* 386.6621 (1997), p. 143.

[14] Swapnajit Chakravarty et al. "Slow light engineering for high Q high sensitivity photonic crystal microcavity biosensors in silicon". In: *Biosensors and Bioelectronics* 38.1 (2012), pp. 170–176.

[15] John D. Joannopoulos et al. *Photonic Crystals - Molding the Flow of Light*. Princeton University Press, 2008.

[16] Johannes Skaar. *Elektromagnetisme*. Available online at `https://www.ntnu.no/wiki/download/attachments/89163550/elektromagnetisme.pdf`. 2017.

[17] Richard Phillips Feynman, Robert B. Leighton, and Matthew Sands. *The Feynman Lectures on Physics, Vol. 2: Mainly Electromagnetism and Matter*. Basic Books, 2011.

[18] David K. Cheng. *Field and Wave Electromagnetics*. Pearson, 2014.

[19] PC Hemmer. *Kvantemekanikk*. Universitetsforlaget, 2005.

[20] Steven G Johnson et al. "Perturbation theory for Maxwell's equations with shifting material boundaries". In: *Physical review E* 65.6 (2002), p. 066611.

[21] Charles Kittel. *Introduction to Solid State Physics*. John Wiley & Sons, 2005.

[22] Felix Bloch. "Über die quantenmechanik der elektronen in kristallgittern". In: *Zeitschrift für physik* 52.7-8 (1929), pp. 555–600.

[23] C Jamois et al. "Silicon-based two-dimensional photonic crystal waveguides". In: *Photonics and Nanostructures - Fundamentals and Applications* 1.1 (2003), pp. 1–13.

[24] Steven G Johnson et al. "Linear waveguides in photonic-crystal slabs". In: *Physical Review B* 62.12 (2000), p. 8212.

[25] Yoshihiro Akahane et al. "High-Q photonic nanocavity in a two-dimensional photonic crystal". In: *Nature* 425.6961 (2003), p. 944.

[26] C Manolatou et al. "Coupling of modes analysis of resonant channel add-drop filters". In: *IEEE journal of quantum electronics* 35.9 (1999), pp. 1322–1331.

[27] Ziyang Zhang and Min Qiu. "Coupled-mode analysis of a resonant channel drop filter using waveguides with mirror boundaries". In: *JOSA B* 23.1 (2006), pp. 104–113.

[28] Ian M White and Xudong Fan. "On the performance quantification of resonant refractive index sensors". In: *Optics express* 16.2 (2008), pp. 1020–1028.

[29] William H. Press et al. *Numerical Recipes Third Edition: The Art of Scientific Computing*. Cambridge university press, 2007.

[30] Steven G Johnson and John D Joannopoulos. "Block-iterative frequency-domain methods for Maxwell's equations in a planewave basis". In: *Optics express* 8.3 (2001), pp. 173–190.

[31] Kane Yee. "Numerical solution of initial boundary value problems involving Maxwell's equations in isotropic media". In: *IEEE Transactions on antennas and propagation* 14.3 (1966), pp. 302–307.

[32] Ardavan F Oskooi et al. "MEEP: A flexible free-software package for electromagnetic simulations by the FDTD method". In: *Computer Physics Communications* 181.3 (2010), pp. 687–702.

[33] Vladimir A Mandelshtam and Howard S Taylor. "Harmonic inversion of time signals and its applications". In: *The Journal of chemical physics* 107.17 (1997), pp. 6756–6769.

[34] W. Bogaerts and S.K. Selvaraja. "13 - Silicon-on-insulator (SOI) technology for photonic integrated circuits (PICs)". In: *Silicon-On-Insulator (SOI) Technology*. Ed. by Oleg Kononchuk and Bich-Yen Nguyen. Woodhead Publishing, 2014, pp. 395–434. ISBN: 978-0-85709-526-8.

[35] Michael Quirk and Julian Serda. *Semiconductor Manufacturing Technology*. Vol. 1. 2001.

[36] Ludwig Reimer. *Scanning electron microscopy: physics of image formation and microanalysis*. Vol. 45. Springer, 2013.

[37] HH Li. "Refractive index of silicon and germanium and its wavelength and temperature derivatives". In: *Journal of Physical and Chemical Reference Data* 9.3 (1980), pp. 561–658.

[38] IH Malitson. "Interspecimen comparison of the refractive index of fused silica". In: *Josa* 55.10 (1965), pp. 1205–1209.

[39] George M Hale and Marvin R Querry. “Optical constants of water in the 200-nm to 200-μm wavelength region”. In: *Applied optics* 12.3 (1973), pp. 555–563.

[40] Huimin Ouyang, Christopher C Striemer, and Philippe M Fauchet. “Quantitative analysis of the sensitivity of porous silicon optical biosensors”. In: *Applied Physics Letters* 88.16 (2006), p. 163108.

[41] Steven G Johnson et al. “Roughness losses and volume-current methods in photonic-crystal waveguides”. In: *Applied Physics B* 81.2-3 (2005), pp. 283–293.

[42] Stephen Hughes et al. “Extrinsic optical scattering loss in photonic crystal waveguides: role of fabrication disorder and photon group velocity”. In: *Physical review letters* 94.3 (2005), p. 033903.

[43] Lars H Frandsen et al. “Photonic crystal waveguides with semi-slow light and tailored dispersion properties”. In: *Optics Express* 14.20 (2006), pp. 9444–9450.

[44] Takashi Asano et al. “Photonic crystal nanocavity with a Q factor exceeding eleven million”. In: *Optics express* 25.3 (2017), pp. 1769–1777.

[45] Bong-Shik Song et al. “Ultra-high-Q photonic double-heterostructure nanocavity”. In: *Nature materials* 4.3 (2005), p. 207.

[46] Hiroshi Sekoguchi et al. “Photonic crystal nanocavity with a Q-factor of $\sim$ 9 million”. In: *Optics Express* 22.1 (2014), pp. 916–924.

[47] Dirk Englund, Ilya Fushman, and Jelena Vuckovic. “General recipe for designing photonic crystal cavities”. In: *Optics express* 13.16 (2005), pp. 5961–5975.

[48] Yoshihiro Akahane et al. “Fine-tuned high-Q photonic-crystal nanocavity”. In: *Optics Express* 13.4 (2005), pp. 1202–1214.

[49] Tatsuya Nakamura et al. “Improvement in the quality factors for photonic crystal nanocavities via visualization of the leaky components”. In: *Optics express* 24.9 (2016), pp. 9541–9549.

[50] Andrei Faraon et al. “Efficient photonic crystal cavity-waveguide couplers”. In: *Applied Physics Letters* 90.7 (2007), p. 073102.

[51] Che-Yun Lin et al. “Group velocity independent coupling into slow light photonic crystal waveguide on silicon nanophotonic integrated circuits”. In: *Optoelectronic Interconnects and Component Integration XI*. Vol. 7944. International Society for Optics and Photonics. 2011, 79440K.

[52] Yi Zou et al. “The role of group index engineering in series-connected photonic crystal microcavities for high density sensor microarrays”. In: *Applied physics letters* 104.14 (2014), p. 141103.

[53] Hitomichi Takano et al. “Highly efficient multi-channel drop filter in a two-dimensional hetero photonic crystal”. In: *Optics express* 14.8 (2006), pp. 3491–3496.

[54] Bong-Shik Song, Susumu Noda, and Takashi Asano. “Photonic devices based on in-plane hetero photonic crystals”. In: *Science* 300.5625 (2003), pp. 1537–1537.

[55] Minhao Pu et al. “Ultra-low-loss inverted taper coupler for silicon-on-insulator ridge waveguide”. In: *Optics Communications* 283.19 (2010), pp. 3678–3682.

[56] John Canny. “A computational approach to edge detection”. In: *Readings in computer vision*. Elsevier, 1987, pp. 184–203.

[57] Richard O Duda and Peter E Hart. “Use of the Hough Transformation To Detect Lines and Curves in Pictures”. In: *Communications* (1972).

[58] Caroline A Schneider, Wayne S Rasband, and Kevin W Eliceiri. “NIH Image to ImageJ: 25 years of image analysis”. In: *Nature methods* 9.7 (2012), p. 671.

[59] Jens Høvik et al. “Lab-on-a-chip photonic biosensor for detection of antigens”. In: *Biosensing and Nanomedicine XI*. Vol. 10728. International Society for Optics and Photonics. 2018, p. 1072806.

[60] Sharee J McNab, Nikolaj Moll, and Yurii A Vlasov. “Ultra-low loss photonic integrated circuit with membrane-type photonic crystal waveguides”. In: *Optics express* 11.22 (2003), pp. 2927–2939.

[61] Toshihiko Baba. “Slow light in photonic crystals”. In: *Nature photonics* 2.8 (2008), p. 465.

[62] Shousaku Kubo, Daisuke Mori, and Toshihiko Baba. “Low-group-velocity and low-dispersion slow light in photonic crystal waveguides”. In: *Optics letters* 32.20 (2007), pp. 2981–2983.

[63] TLK-L1550M - Tunable Laser Kit datasheet. *Thorlabs*. Available online at `https://www.thorlabs.com/catalogpages/Obsolete/2018/TLK-L1550M.pdf`.

Appendices

Appendix A

COMSOL Multiphysics

This appendix aims to introduce the reader to the wave optics module in COMSOL. Tutorials will be given on the effective refractive index calculations mentioned in Chapter 3, and on transmission calculations for a simple photonic crystal drop filter. The effective refractive index tutorial is the same as presented in the report for the project work prior to the master's project.

Tutorial: Effective Refractive Index

Defining the Physics

Start by creating a new file. Select **Model Wizard** followed by **2D**. The **Wave Optics** module is found under the **Optics** branch. The effective refractive index is calculated in the frequency domain, and **Electromagnetic Waves, Frequency Domain (ewfd)** should therefore be selected. Propagation constants for a given frequency, and therefore also the effective refractive index, can be calculated in COMSOL by **Mode Analysis**. After pressing **done**, the graphical user interface should appear with the **Model Builder** (Fig. A.1) visible at the left side of screen.

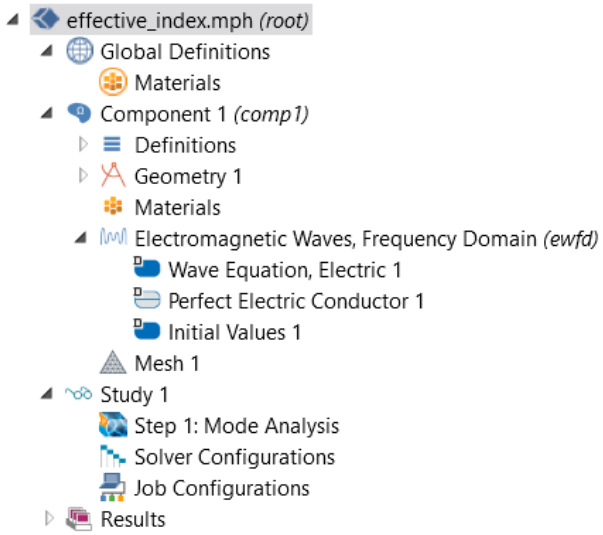

Figure A.1: Model builder in the Wave Optics module.

Setting Parameters and Adding Geometry

Firstly, the parameters used in the simulation have to be defined. A list of parameters are added to the simulation by right-clicking **Global Definitions** and selecting **Parameters**. The

Table A.1: Parameters used in the effective refractive index calculation.

Name	Expression	Description
n_air	1	Refractive index of air
n_si	3.48	Refractive index of silicon
n_cladding	1.44	Refractive index of SiO_2 cladding
height_air	1[um]	Thickness of air layer
height_si	220[nm]	Thickness of silicon thin film
height_cladding	1[um]	Thickness of cladding
width	1[um]	Width of the slab
wavelength	1550[nm]	Wavelength of the mode
f0	c_const/wavelength	Frequency of the mode

parameters used here are shown in Table A.1.

The SOI slab simulated here is made by adding geometries. Right-click **Geometry 1** and add three rectangles from the menu. The first rectangle is meant to be the cladding, and the settings for this rectangle is shown in Figure A.2. The settings for the other rectangles are

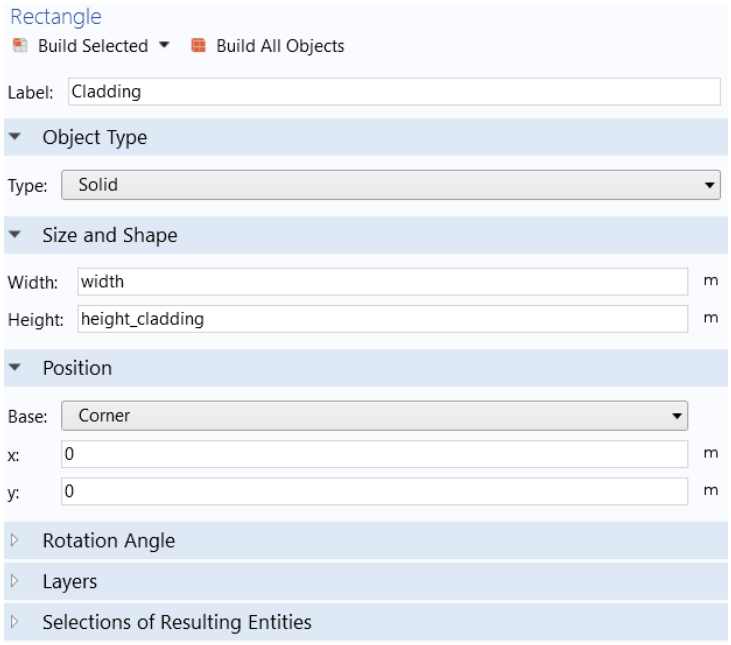

Figure A.2: Settings for the cladding rectangle.

similar, but the **y**-position should be shifted and the correct height parameter from **Parameters** should be chosen. Pressing **F8** or clicking **Build All** in the geometry menu should result in the geometry shown in Figure A.3. The **Zoom Extents** button in the **Graphics** tab automatically places the built geometry in the middle of the window. We have to assign different materials to the three rectangles. This is done by right-clicking **Materials** and choosing **Blank Material** three times. The materials are changed by selecting them and setting the **Refractive index, real part** equal to one of the refractive indices defined in the **Parameters**. The corresponding rectangle can be set to this material by clicking on the rectangle in the **Graphics** tab when selection is set to active, as can be seen in Figure A.3.

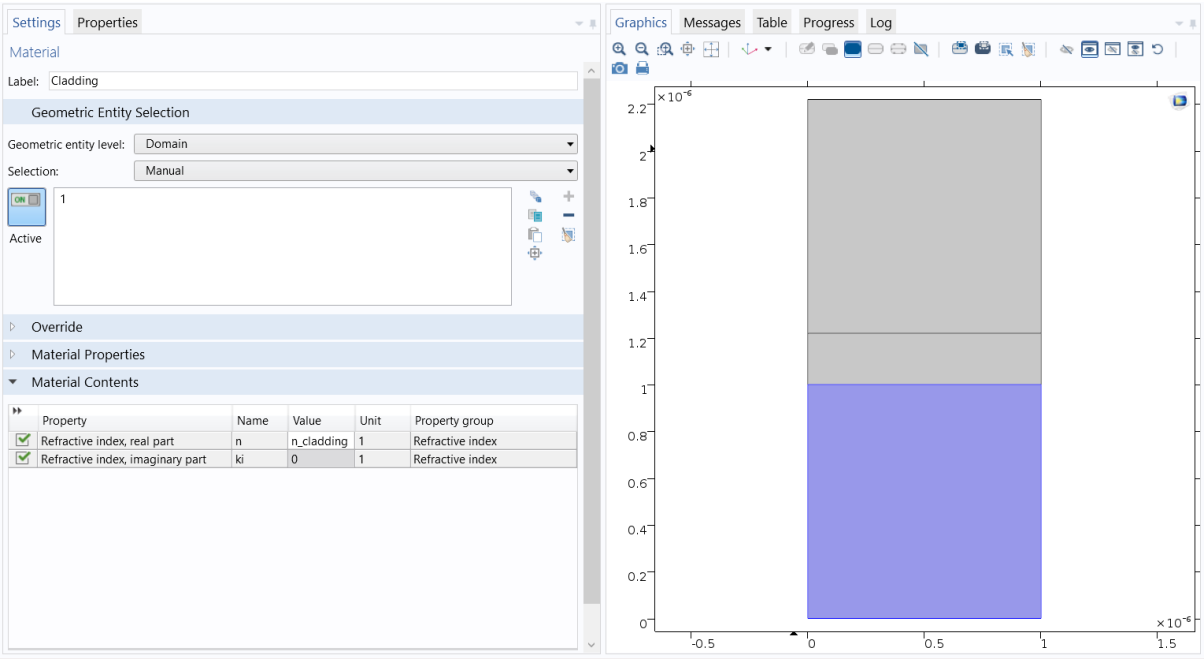

Figure A.3: The settings tab for materials and the Graphics tab.

Simulation Settings

Meshing of the geometry is done by choosing **Mesh 1** in the **Model Builder**. A **Physics-controlled mesh** with **Extremely fine** element size is fine for this simulation. We are interested in calculating the effective index for a range of wavelengths. This is done in COMSOL by right-clicking **Study 1** and selecting **Parametric Sweep** from the menu. The settings for the parametric sweep are shown in Figure A.4. The effective index is calculated for wavelengths between 1480 nm and 1620 nm. The settings for the mode analysis also have to be changed.

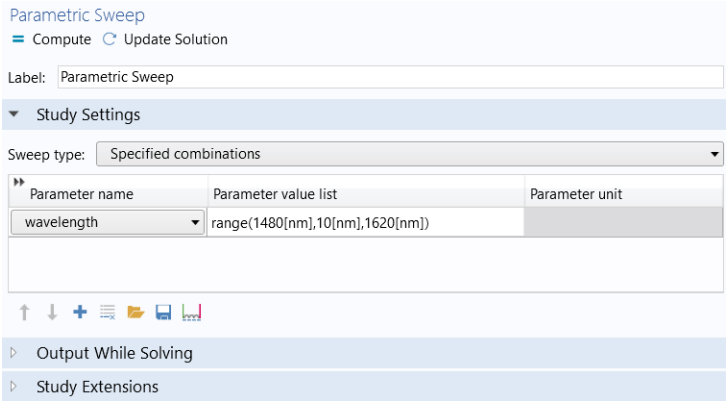

Figure A.4: The settings used in the parametric sweep.

The **Mode analysis frequency** should be set to f0, the **Desired number of modes** is 1 and we should **Search for modes around** 3, meaning that we expect the effective refractive index to be around 3. The simulation is now ready to be run. This is done by selecting **Study 1** and pressing **Compute**.

Results

The calculation should be finished after a couple of minutes. The electric field norm is shown in the **Graphics** tab by selecting **Electric Field (ewfd)** in the **Results** menu. The electric

Table A.2: Parameters used in the transmission simulation of a drop filter.

Name	Expression	Description
n_air	1	Refractive index of air
n_soi	2.88	Refractive index of SOI slab
a	1[um]	Lattice constant
A	sqrt(3)/2*a	Distance between rows
r	0.26*a	Air hole radius
padding	2*a	Thickness of PMLs
numx	29	Air holes in x-direction
numy	19	Air holes in y-direction
slab_length	(numx-1)*a	Slab length
slab_width	(numy-1)*A	Slab width
unitless_f	0.25	Unitless frequency
f0	unitless_f*c_const/a	Frequency

field profile for different wavelengths can be plotted by selecting the preferred wavelength in the **Parameter value** dropdown menu and pressing **Plot**. The effective index as a function of wavelength can be found by right-clicking **Derived Values**, selecting **Global Evaluation**, and setting the **Expression** to **ewfd.neff**. The results will be shown in a table to the right of the screen.

Tutorial: Photonic Crystal Drop Filter

Defining the Physics

Open a new file and select the same physics and dimensions as above. Under **Study** check **Frequency Domain** and press **Done**. To calculate the transmission through the filter, we need to add boundary mode analysis steps to the study. Right click **Study 1** in the **Model Builder** and select **Boundary Mode Analysis** under **Study Steps**, **Other**. Add two **Boundary Mode Analysis** and drag the two steps before the **Frequency Domain**-step.

Setting Parameters

Right click **Global Definitions** in the **Model Builder** drop-down menu and select **Parameters**. The parameters used in this simulation are presented in Table A.2.

Adding Geometry and Materials

To create the simulation geometry, we start by creating the air holes. Right click on **Geometry 1** in the **Model Builder** and add two circles. Set the **Radius** to r, and position the two circles at (1/2*a, 0) and (0, A) with **Base** at the **Center** of the circle. Next, select **Array** under **Transforms** from the geometry drop-down menu. Select the two circles as **Input objects**, and fill in the following entries: **x size** = numx, **y size** = numy under **Size**, and **x** = a, **y** = 2*A under **Displacement**. An array of circles should now be visible in the **Graphics** tab. Later, we will delete some of the circles, but first we add the SOI slab, input and output waveguides. Add a rectangle with **Width** = slab_length + 2*padding, **Height** = slab_width + 2*padding, and position the corner in **x** = -padding, **y** = -padding. Under **Layers**, set Layer 1 thickness to padding and add layers to the left, right, above and below the rectangle. Next, add two rectangles with base at the corner in position **x** = -padding, **y** = r + 13*A. Set the **Height** to 2*A - 2*r and **Width** to padding and padding/2. Right click the two newest rectangles and press **Duplicate**. Change the position to (slab_length, r + 3*A). All geometric objects are now added, and we only have to remove some objects to finish the simulation geometry. Right

click **Geometry 1** and select **Delete Entities**. Select the objects shown in Figure A.5 using the **Select Box** tool in the **Graphics tab**.

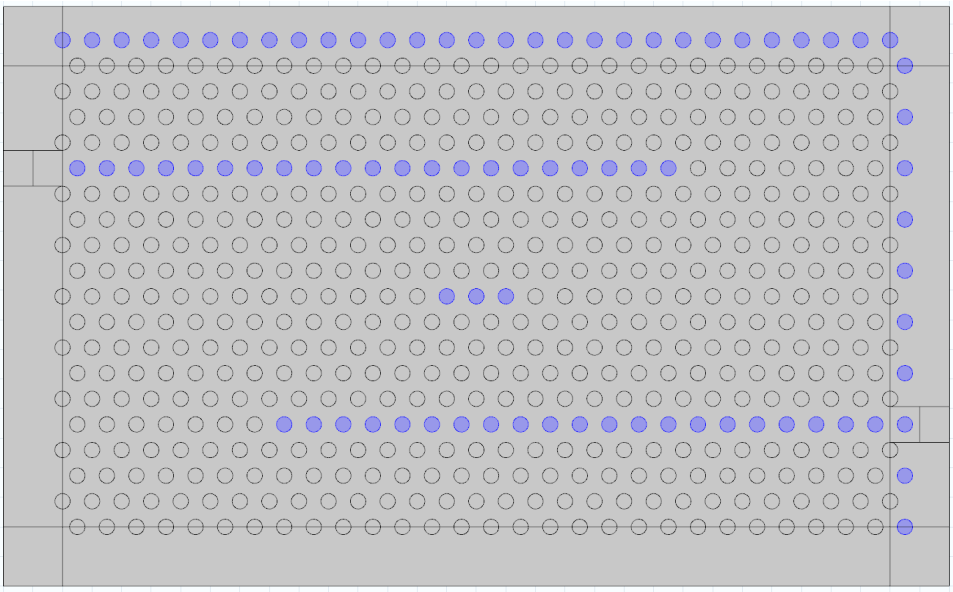

Figure A.5: The geometric objects to be deleted.

After the simulation geometry is made, add a **Perfectly Matched Layer** by right-clicking **Definitions** and select the outer layer of the geometry.

To assign the correct material properties to the different geometrical objects, right click on **Materials** in the **Model Builder** and select **Blank Material**. Enter n_air as the refractive index of the material and deselect the slab, the padding above and below the slab, and the two waveguides. This is done by clicking the objects in the **Graphics** tab. Add a new blank material, select the objects deselected for the air, and set the refractive index to n_soi.

Simulation Settings

Ports needed for calculating the transmission through the filter is added by right-clicking **Electromagnetic Waves, Frequency Domain (ewfd)** and selecting **Port**. Two ports are needed, one for input and one for output. Select the boundary shown in Figure A.6 for **Port 1**. This is the input waveguide. Select the boundary in the waveguide on the other side of the photonic crystal for **Port 2**. Set the **Type of port** to **Numeric** and set **Wave excitation at this port** to **On** for **Port 1** and **Off** for **Port 2**. After the ports have been made click **Electromagnetic Waves, Frequency Domain (ewfd)** in the **Model Builder** and deselect the rectangles behind the ports.

In **Step 1** and **Step 2** of **Study 1**, set the **Mode analysis frequency** to f0, and **Search for modes around** 2.88. It is also important that the **Port name** matches the name of the ports defined under **Electromagnetic Waves, Frequency Domain (ewfd)**. In **Step 3: Frequency Domain** set **Frequencies** to f0.

Meshing is done in the same as for the effective index calculation. Since the geometry is larger and more complicated for this simulation, a larger element size such as **Normal** is recommended to reduce the simulation time.

The transmission simulation can now be started by pressing **Compute** in the **Settings** tab of **Study 1**. The simulation time for a single frequency should be around one minute. By right-clicking **Study 1** and selecting **Parametric Sweep** one can calculate the transmission spectrum for a range of frequencies. Select unitless_f from the drop-down list under **Parameter name**. Setting the **Parameter value list** to range(0.25,1.0e-4,0.254) should cover the frequency range

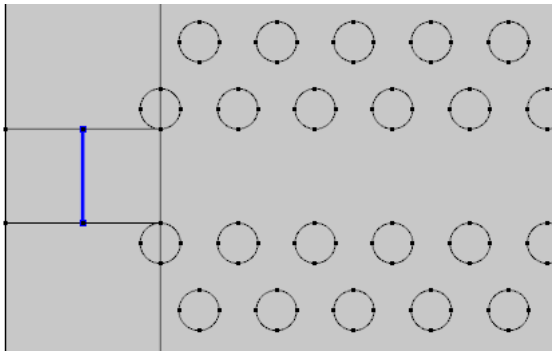

Figure A.6: The excitation port is marked in blue.

where we expect to find the resonance peak of the filter. The parametric sweep with the frequency range here takes around 30 minutes to finish.

Data Analysis

The transmission spectrum is calculated by right-clicking **Derived Values** under **Results**, selecting **Global Evaluation**, and setting the **Expression** to abs(efwd.S21)^2. After pressing **Evaluate**, a table should appear with calculated transmission for the frequencies in the parametric sweep. The table can be plotted by pressing **Table Graph** in the **Table** tab, and the spectrum shown in Figure A.7 should appear. The electric field norm is plotted by default after the simulations is finished, and plots of the different components of the electric and magnetic field can be made by using a **2D Plot Group**.

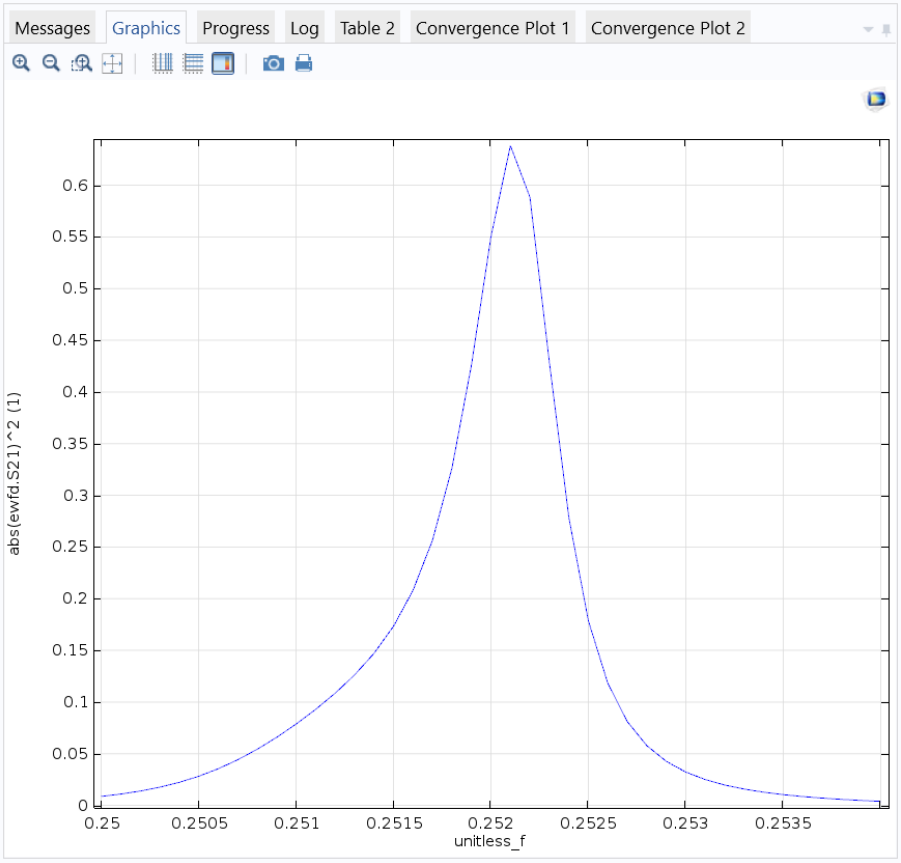

Figure A.7: The transmission spectrum for a drop filter simulated using COMSOL.

Appendix B

MIT Electromagnetic Equation Propagation

In this appendix, simulating photonic crystal drop filters using Meep will be briefly explained. More tutorials are found in the online reference for Meep (https://meep.readthedocs.io/en/latest). The installation of Meep was discussed in the project report and is repeated here.

Installation and Running Simulations

The easiest way of installing Meep is to use the Conda package manager, where packages for Meep is available for Linux and macOS. Additionally, Meep can also be installed on Windows by using the Windows Subsystem for Linux, where one can install a Linux distribution and its terminal in Windows. The lightweight version of Conda, Miniconda, can be installed from the Linux terminal with the following commands:

```
wget https://repo.continuum.io/miniconda/Miniconda3-latest-Linux-x86_64.sh -O
miniconda.sh
bash miniconda.sh -b -p documents/miniconda
```

Miniconda will here be placed in the folder `documents/miniconda`. To run conda from the terminal, the program has to be copied to a folder where the terminal can find it. This is done by

```
sudo cp documents/miniconda/bin/conda /usr/bin/
echo ". /home/username/documents/miniconda/etc/profile.d/conda.sh" >> ~/.bashrc
```

where "username" is your Linux username. Next, serial and parallel Meep can be installed using Miniconda by

```
conda create -n mp -c chogan -c conda-forge pymeep
conda create -n pmp -c chogan -c conda-forge pymeep-parallel
```

Conda environments called `pmp` and `mp` are created, and these must be activated before running simulations. For instance, if one wants to use parallel Meep, the environment called `pmp` has to be activated. This is done by

```
conda activate pmp
```

With the environment activated, python scripts can be run from the terminal. When using parallel Meep, the number of processes is specified before running the script. The command for running the script `scriptName.py` with four processes is

```
mpirun -np 4 python scriptName.py
```

Tutorial: Quality Factor of Resonance Cavity

A simple method for calculating the quality factor of a linear cavity is to analyze the decay of the field in the cavity using Harminv. First, Meep and the necessary libraries are imported

```
import meep as mp
import numpy as np
import argparse
import math
```

The `math` library is used for mathematical functions, `numpy` is used for saving simulation data, while `argparse` simplifies passing input to the script from the terminal. The simulation is placed in a function called `main` that will be called when running the script from the terminal. The input from the terminal is placed in the `args` variable. The unit length in Meep is set to 1 µm, and the lattice constant of the photonic crystal is therefore also set to this length. Other lengths will be scaled accordingly.

```
def main(args):
    A = np.sqrt(3)/2
    r = 0.26

    numx = 29
    numy = 19

    pml = 2
    padding = 1
    slab_length = numx - 1
```

The variable names used in the COMSOL is repeated here. `A` is the distance between two rows of holes, `numx` and `numy` is the number of holes in the x- and y-direction. The widths of the padding and the perfectly matched layers are set in the `padding` and `pml` variables. The computational cell and the PML layers used in the simulation are then defined by

```
sx = slab_length + 2*pml + 2*padding
sy = (numy - 1)*A + 2*pml + 2*padding

cell = mp.Vector3(sx, sy)
pml_layers = [mp.PML(pml)]
```

where `sx` and `sy` is the size of the computational cell in x- and y-direction. We then create a `mp.Medium` with refractive index of 2.88 that will be used for the SOI slab.

```
soi = mp.Medium(index=2.88)
```

With all dimensions and materials defined, the simulation geometry can be made. An empty array for storing the geometry is made. The silicon slab and the air holes are then added to the array, and SOI-cylinders are added above the air holes where the resonance cavity is made. The `material` is not defined for the air holes, and the default material which is air will therefore be used.

```
geometry = []

#SOI slab
geometry.append(mp.Block(size=mp.Vector3(slab_length, sy),
                         material=soi))

#Air holes
for i in range(-math.floor(numx/2), math.ceil(numx/2)):
    for j in range(-math.floor(numy/2), math.ceil(numy/2)):
```

```
        if ((j+1) % 2 == 0):
            geometry.append(mp.Cylinder(radius=r, center=mp.Vector3(i + 0.5, j*A)))
        else:
            geometry.append(mp.Cylinder(radius=r, center=mp.Vector3(i, j*A)))

#Cavity
for i in range(-1, 1):
    geometry.append(mp.Cylinder(radius=r, center=mp.Vector3(i, 0),
                                material=soi))
```

The light source used in the simulation is a Gaussian-pulse source with center frequency `fcen` and frequency width `df` passed from terminal:

```
fcen = args.fcen
df = args.df

sourceCenter = mp.Vector3(0, 0)
src = [mp.Source(mp.GaussianSource(fcen, fwidth=df), mp.Ey, sourceCenter)]
```

The source is placed in the middle of the cavity, and the electric field is excited in the y-direction. The system considered here is symmetric in both directions, and the simulation can therefore be sped up by specifying the symmetry. Additionally, the resolution is set to 16 grid points per lattice constant.

```
sym = [mp.Mirror(mp.Y, phase=-1), mp.Mirror(mp.X, phase=1)]
resolution = 16
```

The simulation object `sim` and a Harminv-object is then created and the simulation is run for `args.t` time units after the source is turned off.

```
sim = mp.Simulation(cell_size=cell,
                    sources=src,
                    geometry=geometry,
                    boundary_layers=pml_layers,
                    resolution=resolution,
                    symmetries=sym)
sim.use_output_directory("output")
harminv = mp.Harminv(mp.Ey, mp.Vector3(0, 0), fcen, df)
sim.run(mp.at_beginning(mp.output_epsilon),
        mp.after_sources(harminv),
        until_after_sources=args.t)
sim.run(mp.at_every(1 / fcen / 20, mp.output_efield_y), until=1 / fcen)
```

A .h5-file of the simulation geometry is saved in the folder named "output" and the electric field at `mp.Vector(0, 0)` is analyzed using the `harminv` object after the source is turned off. After the simulation is finished, the electric field in the y-direction is outputted as .h5-files. The resonance frequencies and the corresponding quality factors calculated using Harminv are saved in the "harminv.dat" file after outputting the electric field.

```
np.savetxt("harminv.dat",
           np.array(([m.freq for m in harminv.modes], [m.Q for m in harminv.modes])).T,
           delimiter=",")
```

Finally we define the starting point of the python script. Arguments given in the terminal are passed to the `main` function.

```
if __name__ == '__main__':
    parser = argparse.ArgumentParser()
    parser.add_argument('-fcen', type=float, default=0.252, help="Center frequency")
```

```
    parser.add_argument('-t', type=float, default=10000, help="Simulation time")
    parser.add_argument('-df', type=float, default=0.1, help="frequency width")
    args = parser.parse_args()
    main(args)
```

Below, the python script is run using four processes, and the center frequency is set to 0.25168, while the other parameters are set to the default values.

```
mpirun -np 4 python linearCavity_harminv.py -fcen 0.25168
```

where `linearCavity_harminv.py` is the name of the script. The .h5-files can be converted to .png-files using `h5topng`:

```
h5topng -RZc RdBu -C linearCavity_harminv-eps*.h5 linearCavity_harminv-ey*.h5.
```

It is a good idea to check if the resonance modes look the way you expect them to. In this case, the mode profile should look like the one shown in Figure B.1.

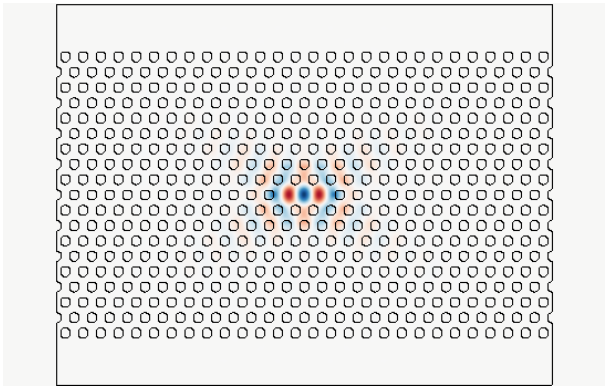

Figure B.1: E_y of the resonance mode for a linear cavity made by removing three air holes from a photonic crystal.

The quality factor for this resonance is approximately 920,000. A large quality factor is expected in 2D due to the photonic band gap. If the number of holes surrounding the cavity is reduced, the quality factor of the cavity will be reduced. Setting `numy` to 9 will result in a quality factor of around 2,300.

Tutorial: Photonic Crystal Drop Filter

Meep can also be used to calculate transmission through devices such as the drop filter considered here. A filter made by placing waveguides four rows above and below the cavity discussed in the previous tutorial is simulated using the script below.

```
import meep as mp
import numpy as np
import argparse
import math


def main(args):
    A = math.sqrt(3)/2
    r = 0.26

    numx = 29
    numy = 19
```

```
pml = 2
padding = 1
slab_length = numx - 1
slab_width = (numy - 1)*A
wg_width = 2*A - 2*r
sx = slab_length + 2*pml + 2*padding
sy = slab_width + 2*pml + 2*padding

cell = mp.Vector3(sx, sy)
pml_layers = [mp.PML(pml)]

eps = math.pow(2.88, 2)

fcen = args.fcen
df = args.df

source_sep = 1.5
flux_sep = 1.5

geometry = []

if (args.ref):
    filename = "reference.dat"
    geometry.append(mp.Block(size=mp.Vector3(sx, wg_width),
                     material=mp.Medium(epsilon=eps)))
    sourcePos = mp.Vector3(-sx/2 + source_sep, 0)
    source = [mp.Source(mp.GaussianSource(fcen, fwidth=df), mp.Ey, center=sourcePos)]
    fluxPos = mp.Vector3(sx/2 - flux_sep, 0)
    fluxRegion = mp.FluxRegion(center=fluxPos, size=mp.Vector3(0, 2*wg_width))
else:
    filename = "transmission.dat"
    geometry.append(mp.Block(size=mp.Vector3(slab_length, slab_width),
                             material=mp.Medium(epsilon=eps)))

    for i in range(-math.floor(numx/2), math.ceil(numx/2)):
        for j in range(-math.floor(numy/2), math.ceil(numy/2)):
            if ((j+1) % 2 == 0):
                geometry.append(mp.Cylinder(radius=r, center=mp.Vector3(i + 0.5, j*A)))
            else:
                geometry.append(mp.Cylinder(radius=r, center=mp.Vector3(i, j*A)))

    geometry.append(mp.Block(size=mp.Vector3(30, wg_width), center=mp.Vector3(-8, 5*A),
                    material=mp.Medium(epsilon=eps)))
    geometry.append(mp.Block(size=mp.Vector3(30, wg_width), center=mp.Vector3(8, -5*A),
                    material=mp.Medium(epsilon=eps)))
    geometry.append(mp.Block(size=mp.Vector3(3, wg_width), center=mp.Vector3(0, 0),
                    material=mp.Medium(epsilon=eps)))

    sourcePos = mp.Vector3(-sx/2 + source_sep, 5*A)
    source = [mp.Source(mp.GaussianSource(fcen, fwidth=df), mp.Ey, center=sourcePos)]
    fluxPos = mp.Vector3(sx/2 - flux_sep, -5*A)
    fluxRegion = mp.FluxRegion(center=fluxPos, size=mp.Vector3(0, 2*wg_width))
    time = 10000



resolution = 16
nfreq = 2000
```

```
    sim = mp.Simulation(cell_size=cell,
                        sources=source,
                        geometry=geometry,
                        boundary_layers=pml_layers,
                        resolution=resolution)
    sim.use_output_directory("output")

    trans = sim.add_flux(fcen, df, nfreq, fluxRegion)
    if (args.ref):
        sim.run(until_after_sources=mp.stop_when_fields_decayed(50, mp.Ey, fluxPos, 1e-3))
    else:
        sim.run(mp.at_beginning(mp.output_epsilon),
                until=time)


    freqs = np.array(mp.get_flux_freqs(trans))
    fluxes = np.array(mp.get_fluxes(trans))

    np.savetxt(filename, np.array([freqs, fluxes]).T, delimiter=",")


if __name__ == '__main__':
    parser = argparse.ArgumentParser()
    parser.add_argument('-fcen', type=float, default=0.252, help="Center frequency")
    parser.add_argument('-df', type=float, default=0.01, help="Frequency width")
    parser.add_argument('-ref', type=bool, default=False, help="Reference run")
    args = parser.parse_args()
    main(args)
```

The main differences compared to the previous tutorial is that the source is moved from the center of the structure to upper waveguide, left of the photonic crystal and that the flux through the lower waveguide is recorded. Additionally, a reference simulation where the transmission through a straight strip waveguide is recorded is run if `args.ref` is set to `True` when running the script from a terminal. The transmission is saved in the file "transmission.dat" or "reference.dat". After both simulations have been run, which should take around 15 minutes, the transmission can be plotted using `matplotlib`:

```
import matplotlib.pyplot as plt
import numpy as np

transmission = np.loadtxt("transmission.dat", delimiter=",")
reference = np.loadtxt("reference.dat", delimiter=",")

plt.plot(reference[:,0], transmission[:,1]/reference[:,1])
plt.xlabel("Frequency $\omega a /2\pi c$")
plt.ylabel("Transmission")

plt.show()
```

The flux data is loaded using `numpy`, and the transmission of the drop filter is normalized by the reference flux and plotted using `matplotlib`. The transmission plot should look like the plot shown in Figure B.2. If you are using the Windows Subsystem for Linux plotting is not supported, but there are workarounds using Xming (https://stackoverflow.com/a/43399827).

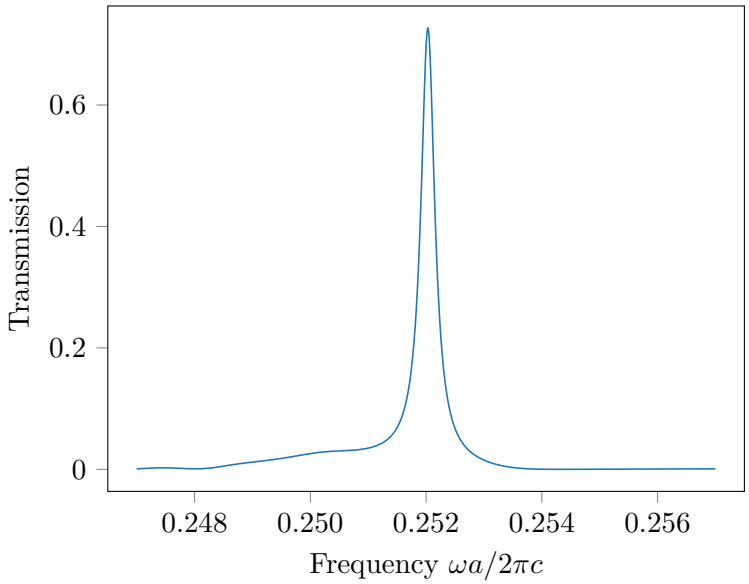

Figure B.2: The transmission spectrum for a drop filter simulated using Meep.

Appendix C

MIT Photonic Bands

MPB for Python is included in the Meep library discussed in Appendix B. The tutorial given here explains how to calculate band structures for linear defect waveguides in 2D. As for the Meep scripts, the necessary libraries are imported

```
import math
import meep as mp
from meep import mpb
import numpy as np
```

The same libraries used in the Meep tutorials are used here, but additionally `mpb` is imported from the `meep` library. We want to find the bandstructure for a linear defect waveguide made in a triangular photonic crystal of SOI. The supercell approximation has to be used here, and we use a supercell of 11 periods in the y-direction. The lattice is triangular and the basis vectors are therefore specified.

```
r = 0.26
sy = 11
soi = mp.Medium(index=2.88)
geometry_lattice = mp.Lattice(size=mp.Vector3(1, sy),
                              basis1=mp.Vector3(math.sqrt(3)/2, 0.5),
                              basis2=mp.Vector3(math.sqrt(3)/2, -0.5))
```

The geometry is made by placing air holes separated by a lattice constant over the whole supercell, and then removing the air hole in the middle of the cell.

```
geometry = []
for i in np.linspace(-(sy-1)/2, (sy-1)/2, sy):
    geometry.append(mp.Cylinder(radius=r, center=mp.Vector3(0, 0) + mp.Vector3(0, i),
                                material=mp.air))
geometry.append(mp.Cylinder(radius=r, center=mp.Vector3(0, 0), material=soi))
```

We want to calculate the band structure from the origin to the end of the 1st Brillouin zone for a total of 50 k-points.

```
Gamma = mp.Vector3(0, 0)
K = mp.Vector3(0.5, 0)

num_k_points = 50
k_points = [Gamma, K]
k_points = mp.interpolate(num_k_points-2, k_points)
```

The eigenvalue computations for TE-modes are then done by creating a `ModeSolver` object and running the `ms.run_te()` function.

```
ms = mpb.ModeSolver(num_bands=20,
                    k_points=k_points,
                    geometry=geometry,
                    geometry_lattice=geometry_lattice,
                    resolution=16,
                    default_material=soi)
ms.run_te()
```

After the simulation is finished, the TE-modes can be saved using `numpy`:

```
np.savetxt("te_modes.dat", ms.all_freqs, delimiter=",")
```

The band structure can be plotted using `matplotlib` and should look like the band structure shown in Figure C.1.

```
import matplotlib.pyplot as plt
k = np.linspace(0, 0.5, 50)
plt.plot(k, ms.all_freqs)
plt.xlabel("Wave vector $ka /2\pi$")
plt.ylabel("Frequency $\omega a /2\pi c$")
plt.show()
```

More on data analysis using MPB can be found at https://mbp.readthedocs.io/en/latest.

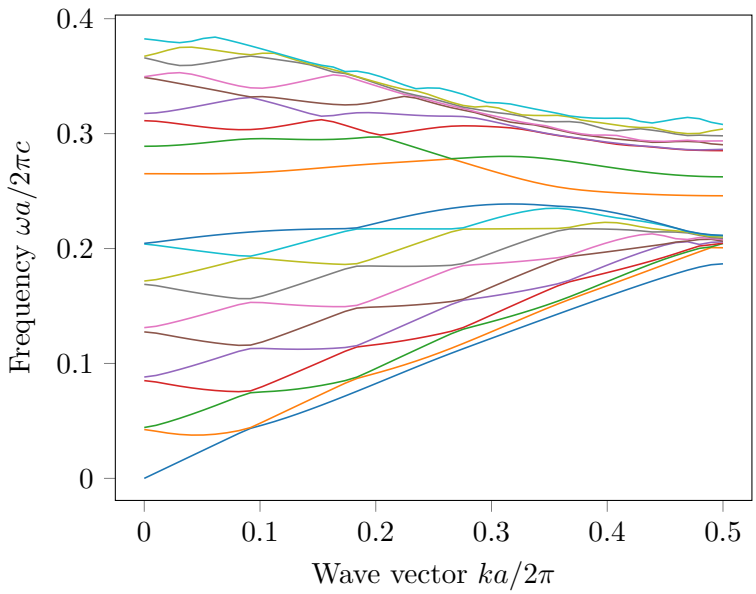

Figure C.1: Band structure for a linear defect waveguide in a triangular photonic crystal.